

**Robust Dynamic Orientation
Sensing Using Accelerometers:
Model-based Methods for
Head Tracking in AR**

Matthew Stuart Keir

A thesis presented for the degree of
Doctor of Philosophy
in
Mechanical Engineering
at the
University of Canterbury,
Christchurch, New Zealand.

24 September 2008

*Dedicated to
Richard and Margaret*

Acknowledgements

This research would not have been possible without the continuous help and support of many people. I begin this thesis by acknowledging them.

My supervisory team: Professor J. Geoffrey Chase inspired me to undertake postgraduate studies, and has provided continual motivation, guidance and advice. Dr Mark Billingham introduced me to Augmented Reality and has supported me within Hitlab. Dr Christopher Hann has helped me rediscover my passion for mathematics, through his unbounded enthusiasm for the subject.

The Tertiary Education Commission (TEC) provided funding for this research and the means to present the findings at conferences.

Technical staff, specifically Rodney Elliott who provided technical assistance and advice within the robotics laboratory.

The Human Interface Technology Lab (HitLab). My colleagues and friends in the HitLab, have assisted, supported, and encouraged me through our interactions during the long hours in the lab.

My friends and training partners from the UC Athletics Club, Coast 2 Coast, and Recreation Centre have provided the sometimes necessary distraction from work, keeping me positive, and giving additional perspective to life.

My family has always encouraged me to do the best, and be the best that I can. The self belief that they have instilled in me and the unconditional support they offer has provided the strong platform on which I build my life.

This is a very limited list, and I would like to thank all the people that have assisted, supported and inspired me, both directly and indirectly throughout my academic endeavours.

Contents

Acknowledgements	v
Abstract	xix
1 Introduction	1
1.1 Augmented Reality	1
1.1.1 AR Applications	3
1.1.2 Registration Performance Requirements	5
1.1.3 Registration Error Sources within AR Systems	8
1.2 Tracking Hand and Body Motion	10
1.3 Head Motion	11
1.3.1 Application of Head Motion Models	14
1.4 Motion Tracking Technology	15
1.5 Overview of Head Tracking in Augmented Reality	19
1.5.1 Compensating for Registration Error	20
1.5.2 Hybrid Tracking Systems	21
1.6 Preface	22
2 Head Motion Modelling and Validation	25
2.1 The Inverted Pendulum Model	25
2.2 Accelerometers	27
2.2.1 Static Tilt Sensing Using Accelerometers	28
2.2.2 Selection and Testing of Accelerometers	29
2.2.3 Accelerometer Calibration Procedures	34
2.3 Verification of the Model Using the Inverted Pendulum	38
2.3.1 Method	38
2.3.2 Results and Discussion	40
2.4 Summary	42
3 Difficulties in Solving the Model Equations	45
3.1 A General Engineering Approach	46
3.2 The Linear System	49

3.3	A Frequency Based Solution	50
3.3.1	Method	51
3.3.2	Results and Discussion	53
3.4	Summary	57
4	Initial Model Implementation	59
4.1	Methods	60
4.1.1	Single Section	60
4.1.2	Multiple Piecewise Sections	66
4.1.3	Analysis and Performance Metrics	70
4.2	Results and Discussion	71
4.2.1	Robustness to Noise	71
4.2.2	Dynamic Performance	75
4.2.3	Experimental Results	77
4.3	Summary	78
5	Optimised Method and Comparisons	81
5.1	Method	81
5.1.1	Initial Improvements	81
5.1.2	Generalised Approach	86
5.2	Results and Discussion	94
5.2.1	Dynamic Performance	94
5.2.2	Experimental Results and Comparisons	96
5.3	Summary	99
6	Extension to Full 2D Dynamics	103
6.1	Extending the Model	103
6.2	Method	106
6.3	Results and Discussion	112
6.3.1	Model Validation	112
6.3.2	Experimental Results and Comparisons	117
6.4	Summary	120
7	Conclusions	123
7.1	Objectives and Approach	123
7.2	The Unique Solution Method	124
7.3	Validation of the Methods	125
7.4	Potential Application Benefits	126
7.5	Summary	127

8	Future Work	129
8.1	Further Validation Methods	129
8.1.1	Using the Method in a Nested Approach	129
8.1.2	Controlling the Inverted Pendulum	130
8.1.3	Head Motion Validation	131
8.2	Extensions of the Methods and Algorithms	131
8.2.1	Extension to Three Dimensional Motion	131
8.2.2	Integrating a Gyroscope into the Methods	131
8.2.3	Investigate and Implement Prediction	132
A	Full Solution to the Generalised Approach	133

List of Figures

1.1	The reality-virtuality continuum	2
1.2	Industrial example of AR. The image is augmented by a planned addition (red pipes), and by an industrial drawing of what is beneath the floor [Appel and Navab, 2002]	4
1.3	Schematic illustrating the absolute registration accuracy and working range of the example applications in Section 1.1.1.	6
1.4	Lateral/depth registration error [Holloway, 1997]	7
1.5	Dynamic Visual Acuity (DVA)	9
1.6	Latency in the AR system application loop	10
1.7	Head motion, 6 degrees of freedom, 3 translational (x,y,z) and 3 rotational (yaw, pitch, roll). Figure from Strickland [2007]	13
1.8	Cumulative density plot of angular velocity for fast and slow head motion sequences [Azuma, 1995]	14
2.1	Acceleration vector diagram for a point at the end of an inverted pendulum, length R , undergoing a rotation of θ . Note the sign convention for rotation is positive in an anticlockwise direction from the vertical.	26
2.2	Using accelerometers to measure static tilt	28

2.3	Comparison accelerometer noise performance	31
2.4	Zero g duty cycle drift with temperature for the second ADXL213 accelerometer. Note, that the y axis of each plot have different scales.	33
2.5	Bode plot showing phase and magnitude response for the ADXL202 accelerometer. Note, no theoretical line is available for the Magnitude response.	35
2.6	Dynamic response testing, ADXL202 accelerometer mounted on voice coil actuator with laser doppler measurement equipment in the background	36
2.7	The indexing table with accelerometers attached for calibration	36
2.8	The output from the first ADXL213 accelerometer during calibration at 21 °C	37
2.9	The inverted pendulum laboratory equipment with accelerometer attached	39
2.10	The inverted pendulum laboratory equipment showing the optical encoder and cart clamped in place	39
2.11	Measured and model accelerations: (A) Tangential acceleration, A_T ; (B) Radial acceleration, A_R	41
3.1	Numerical solutions to the tangential ODE given zero and true initial conditions	47
3.2	Numerical solution to the tangential ODE showing quasi-stability present with small amplitude and true initial conditions	48
3.3	Simulated linearised data, solved analytically using initial conditions with a small additive error $\epsilon = 1\text{e}^{-18}$ applied to the true $\dot{\theta}_0$ initial condition	50

3.4	Flow-chart summarising the Fourier Series based method of solving orientation.	52
3.5	The FFT for both the measured A_T and measured θ_{en} from the optical encoder.	53
3.6	Acceleration fit and solution for slow motion using the frequency based method	55
3.7	Acceleration fit and solution for higher frequency motion using the frequency based method	56
4.1	Linearisation of $\sin(\theta)$ over a short time period	61
4.2	Maximum error in the $\sin(\theta)$ linearisation where $\Delta T = 0.1s$	61
4.3	Flow-chart for the solution of θ	65
4.4	Piecewise linearisation of $\sin(\theta)$	67
4.5	Response to the Mean noise added to simulated data using the single section method, Method A, and piecewise section method, Method B. The methods both track quickly to the true solution, despite non a non zero initial condition, and $\theta_{old} = 0$ value.	74
4.6	The response of the methods presented to increasing dynamics	76
4.7	Experimental results using the three section piecewise method for (A), (B), and (C) data sets compared to θ_{en}	79
5.1	Two methods of determining the $\sin(\theta)$ linearisation range; (A) Using a constant δT for each section, (B) Limiting $\delta\theta$ within each section	83
5.2	Schematic of piecewise cubic sections fitted the measured A_T data	85

5.3	Comparison of the fit of a single cubic expression versus multiple cubic sections to a synthetic A_T signal with no noise added, generated from a 3Hz θ signal with a 10° amplitude	85
5.4	The generalised method showing A_T , θ and $\sin(\theta)$	87
5.5	Flowchart for the generalised method	93
5.6	The improved response of the Generalised Method to increasing dynamics	95
5.7	Sensing devices used for comparisons attached to the pendulum. From left to right, the gyroscope, accelerometer, and Inertia Cube 3 (black box)	96
5.8	Experimentally derived frequency response and comparisons of the generalised method with the Inertia Cube 3 and Gyroscope.	98
5.9	Experimental comparisons to determining orientation, θ , using the Generalised Method (A), Inertia Cube 3 (B), and Gyroscope (C) . . .	100
5.10	Absolute error in θ for the signal and solution methods of Figure 5.9. The Generalised Method (A), Inertia Cube 3 (B), and Gyroscope (C)	101
6.1	Schematic of the extended inverted pendulum model, including rotation and translation of the centre of rotation in a 2 dimensional plane	105
6.2	The inverted pendulum apparatus with two accelerometers attached and cart free to move, also attached is the Inertia Cube 3 and gyroscope	113
6.3	Close up view of cart system of the inverted pendulum with Accelerometer 2 mounted on the pendulum, at the centre of rotation in this case	113

6.4	Cart displacement and total acceleration: (A) Measured displacement via cart encoder; (B) Measured horizontal acceleration, A_H , via Accelerometer 2 and Equation (6.35); (C) Measured vertical acceleration, A_V , via Accelerometer 2 and Equation (6.36)	115
6.5	Measured and model accelerations: (A) Tangential acceleration, A_T ; (B) Radial acceleration, A_R	116
6.6	Experimental comparisons to determining orientation, θ , using the Extended Method (A), Inertia Cube 3 (B), and Gyroscope (C)	118
6.7	Absolute error in θ for the signal and solution methods of Figure 6.6. The Extended Method (A), Inertia Cube 3 (B), and Gyroscope (C) .	119
8.1	The nested system for two pendulum sections	130

List of Tables

1.1	Tracking error specifications	8
1.2	Summary of tracking technologies	17
2.1	Key specifications for the selected accelerometers	30
2.2	Calibration Results at 21°C	37
2.3	Angular and acceleration model error	42
3.1	The model equations	45
4.1	Error response to the presence of noise	73
4.2	Error response when accelerometer placement is shifted	75
4.3	Experimental error results	78
5.1	Generalised method experimental error results for frequency	97
5.2	Generalised method experimental error results for a 15 second signal .	99
6.1	Acceleration model error	114
6.2	Extended method experimental error results for the 10 second signal .	117

Abstract

Augmented reality (AR) systems that use head mounted displays to overlay synthetic imagery on the user's view of the real world require accurate viewpoint tracking for quality applications. However, achieving accurate registration is one of the most significant unsolved problems within AR systems, particularly during dynamic motions in unprepared environments. As a result, registration error is a major issue hindering the more widespread growth of AR applications.

The main objective for this thesis was to improve dynamic orientation tracking of the head using low-cost inertial sensors. The approach taken within this thesis was to extend the excellent static orientation sensing abilities of accelerometers to a dynamic case by utilising a model of head motion.

Head motion is modelled by an inverted pendulum, initially for one degree of rotational freedom, but later this is extended to a more general two dimensional case by including a translational freedom of the centre of rotation. However, the inverted pendulum model consists of an unstable coupled set of differential equations which cannot be solved by conventional solution approaches.

A unique method is developed which consists of a highly accurate approximated analytical solution to the full non linear tangential ODE. The major advantage of the analytical solution is that it allows a separation of the unstable transient part of the solution from the stable solution. The analytical solution is written directly in terms of the unknown initial conditions. Optimal initial conditions are found that remove the unstable transient part completely by utilising the independent radial ODE. Thus, leaving the required orientation.

The methods are validated experimentally with data collected using accelerometers and a physical inverted pendulum apparatus. A range of tests were performed

demonstrating the stability of the methods and solution over time and the robust performance to increasing signal frequency, over the range expected for head motion.

The key advantage of this accelerometer model-based method is that the orientation remains registered to the gravitational vector, providing a drift free solution that outperforms existing, state of the art, gyroscope based methods. This proof of concept, uses low-cost accelerometer sensors to show significant potential to improve head tracking in dynamic AR environments, such as outdoors.

Chapter 1

Introduction

Access to computation and electronically stored information is moving beyond the traditional desktop and into the everyday world. Computers are smaller, more powerful, have more storage and are more connected than ever before. With this proliferation of ubiquitous computing comes the challenge of designing intelligent and intuitive interfaces for human-computer interaction.

Augmented Reality (AR) interfaces are intuitive interfaces that overlay virtual content onto the real world. A key requirement for a compelling AR experience is accurate registration of the virtual imagery. If the virtual imagery moves with the users motion or drifts about, the illusion that it resides in the real environment or its relationship to physical objects is quickly broken. Obtaining accurate registration is one of the largest unsolved problems for AR systems, and is a major issue hindering their growth.

To achieve accurate registration an AR system requires precise knowledge of the users viewpoint. Many existing tracking methods perform poorly especially in highly dynamic applications. This thesis seeks to improve the dynamic accuracy of viewpoint tracking for AR using a low-cost solution. Thus, delivering the first steps towards enabling new inexpensive and highly dynamic AR applications, such as those in outdoor environments.

1.1 Augmented Reality

Azuma [1997] defines AR as the realtime superimposition of computer graphics

on the real world. These virtual images supplement the real world rather than completely replacing it as with Virtual Reality (VR). When accurately positioned and oriented these generated images give the appearance that they coexist with real objects in the environment. Specifically Azuma [1997] defines AR as requiring the following three characteristics:

1. Combining real and virtual
2. Interactive in realtime
3. Images are registered in 3D

Milgram and Kishino [1994] use a Reality-Virtuality continuum shown in Figure 1.1 to place AR in the context of Mixed Reality. The continuum embodies all user experiences. A position along the continuum represents the degree or amount that the users experience is computer generated.

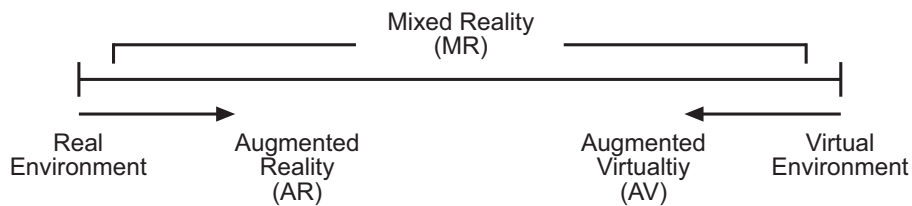


Figure 1.1: The reality-virtuality continuum

On the left of the continuum there is the real environment where real experiences take place, such as walking or eating etc. On the right is the immersive virtual environment where the real environment has been substituted by a computer generated world. The region between these two extremes is known as *Mixed Reality* and includes AR and *Augmented Virtuality*. AR is essentially a real world experience enhanced by the addition of synthetic content. In contrast Augmented Virtuality is an experience in a virtual world with real world elements such as video feeds embedded.

Implementing AR in practice is a challenging problem. Any AR system relies on two fundamental enabling technologies, tracking and display. Various display systems have been used; fixed displays, hand held displays, and head mounted displays (HMD). This thesis focuses on enabling applications using the more intuitive HMD.

To achieve accurate registration of the virtual content for applications using HMDs, the AR system needs relatively exact knowledge of the users viewpoint.

The accuracy and timely delivery of this information is crucial to the quality and practicality of the AR experience. Any error in the placement of the virtual objects quickly destroys the illusion and thus, the usefulness of the data presented.

The successful implementation of AR technology has huge implications for enhancing perception and improving productivity, while reducing errors. These outcomes would be achieved through the addition of contextual information that the user can not detect with their own senses or is in a different form. Various applications have been developed illustrating these potential advantages for different disciplines. Examples are discussed to support these concepts in the sections below.

1.1.1 AR Applications

Most applications have been developed by research groups to prove the concept and potential uses of AR. Recent research has focused on showing new applications rather than solving the underlying problems with the technology. Few of these examples have reached the commercial world. However, they help illustrate the importance and impact AR will have in the world.

Every application presents unique challenges for AR technology. Consideration needs to be given in designing any application to the following factors:

- Display properties;
- The required registration accuracy, see Section 1.1.2;
- Cost limitations;
- Expected motion and dynamics;
- The working volume;
- The operating environment (prepared/unprepared, indoor/outdoor etc).

This thesis focuses on enabling low-cost highly dynamic AR applications through improved tracking. The applications discussed in this section are listed below in order of increasing dynamic motion, providing context to this work. The applications range from medical applications, requiring high precision tracking of slow movements in a small prepared volume, to fully dynamic outdoor gaming applications requiring lower precision tracking in a very large unprepared environment.

1. **Medical:** AR ultrasound imagery [Bajura et al., 1992]
Scenario: Doctors have “X-Ray” vision in a needle biopsy task using a medical interface that overlays virtual ultrasound images onto a patient’s body.
2. **Medical:** Guided surgery [Soler et al., 2004]
Scenario: MRI and CT scans are used to reconstruct 3D patient specific imagery. Using AR this imagery is used to guide abdominal surgery.
3. **Maintenance:** Virtual instructions [Feiner et al., 1993]
Scenario: Users see virtual annotations appearing over a laser printer, showing how to repair the machine.
4. **Education:** Augmented chemistry [Fjeld et al., 2003]
Scenario: Students use augmented tangible objects to help explain basic chemistry.
5. **Industrial:** AR factory visualisation, see Figure 1.2 [Appel and Navab, 2002]
Scenario: AR is used to visualise planned additions in place and check for collisions or interference with existing structures. Industrial AR also allows contractors to quickly find and understand unfamiliar machinery in often very complex environments or processes.

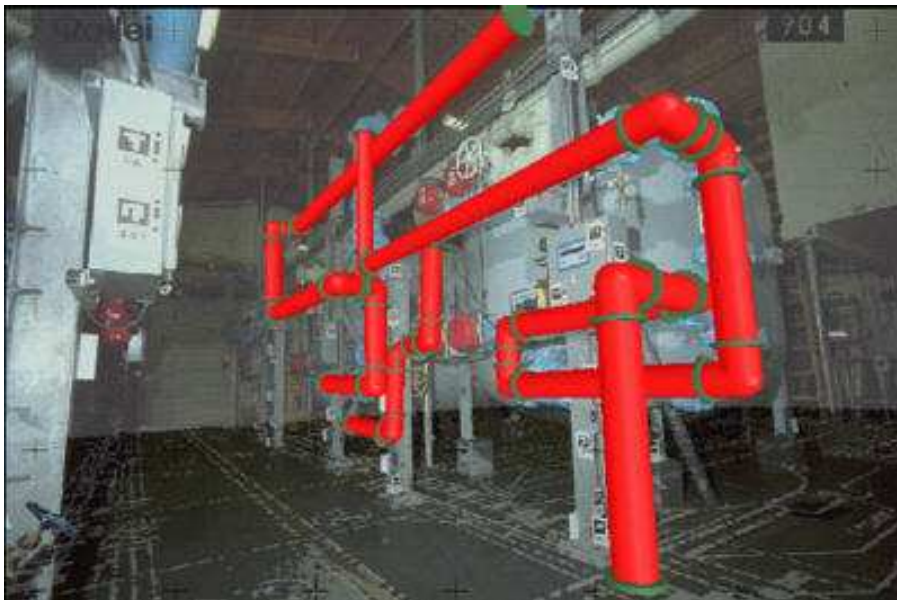


Figure 1.2: Industrial example of AR. The image is augmented by a planned addition (red pipes), and by an industrial drawing of what is beneath the floor [Appel and Navab, 2002]

6. **Architectural:** Civil construction [Behzadan and Kamat, 2005]
Scenario: Civil engineers view a virtual bridge during the construction and planning of the real bridge.
7. **Industrial:** Subsurface visualisation [Roberts et al., 2002]
Scenario: Vast amounts of information on underground features reside in computer databases. However this information is not readily accessible to engineers and managers in the field. This AR system allows users to visualise subsurface features such as gas and water pipe work.
8. **Entertainment:** Outdoor Gaming, AR Pacman [Cheok et al., 2004]
Scenario: 2D arcade Pacman is extended to involve humans as Ghosts or Pacmen in an outdoor environment. Virtual cookies and tangible physical objects are incorporated providing seamless transitions between real and virtual worlds.
9. **Entertainment:** Outdoor Gaming, AR Quake [Piekarski and Thomas, 2002]
Scenario: The existing desktop game Quake is developed into an outdoor AR game. Users move in the physical world, and at the same time experience computer-generated graphical monsters and objects.

These examples illustrate that AR can change perceptions, and improve performance through visual enhancement of the real world. AR is moving from the research environment into applications with commercial value. However, poor accuracy, robustness and high costs of the tracking technology impedes further commercial development, especially for applications using HMDs. These tracking issues are most notable in unprepared dynamic environments, such as outdoors. For AR to become practical for industrial, gaming, architectural and other applications these problems need to begin being addressed within a serious or rigorous framework. It is such a framework and initial approach that is attempted in this thesis.

1.1.2 Registration Performance Requirements

Achieving accurate registration is the biggest problem in building effective AR systems [Azuma, 1997]. Any error or misalignment in the registration of virtual images in an AR application will detract from the experience. The degree to which registration error can be tolerated is heavily dependent on the application being performed.

For example, medical applications require far greater accuracy than outdoor gaming applications. This concept is illustrated schematically in Figure 1.3. The example applications from Section 1.1.1 are plotted against absolute registration accuracy and their working range.

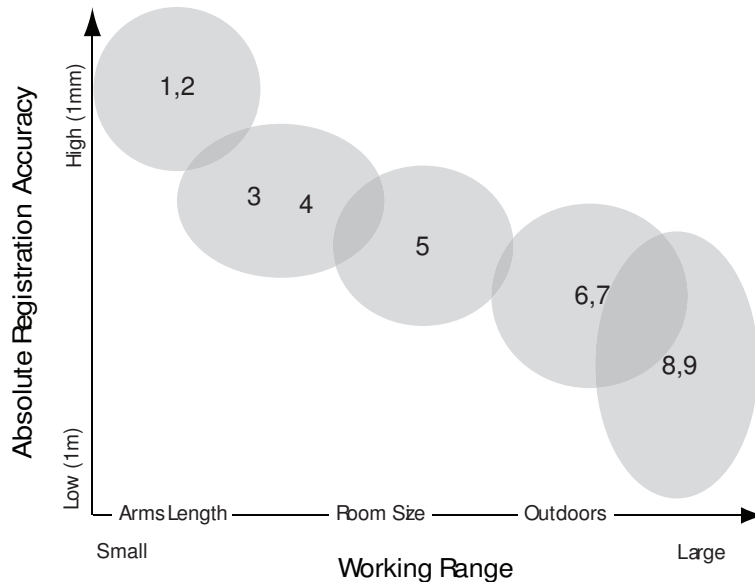


Figure 1.3: Schematic illustrating the absolute registration accuracy and working range of the example applications in Section 1.1.1.

Holloway [1997] analysed errors in AR systems and provides a clear definition of registration error. He defines *angular error* (ϕ) as the angle at the eye point (E) between two supposed coincidental points. *Linear registration error* is the length of a 3D error vector between them. Depth position error can be masked by other depth cues, such as size and head-motion parallax. Thus, registration errors in depth are less important than registration errors that cause a clear visual separation. The *linear registration error* can be broken down into the *lateral error* and *depth error*, as shown in Figure 1.4, where P is the real point, P* is the displayed point, and r is the distance to the viewed object. Lateral error (error) within AR systems is more sensitive to orientation error than position error [Friedmann et al., 1992], as orientation error is scaled by the distance to the viewed object.

Any registration error will ultimately be measured by the users visual system. Humans are not tolerant of visual errors when compared with other sensory inputs. This issue is known as *visual capture*, which is the tendency for the brain to believe what is seen rather than what it feels or hears [Welch, 1978]. This tendency can be an advantage for fully virtual environments, as small tracking errors go unnoticed.

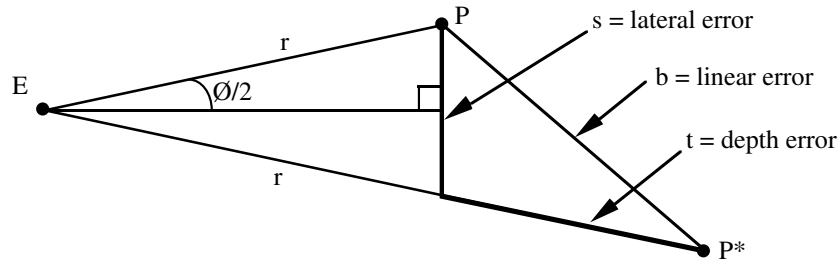


Figure 1.4: Lateral/depth registration error [Holloway, 1997]

However, in AR it becomes very important to minimise visual errors.

The human visual system is incredibly complex. AR tries to deceive the visual system into thinking virtual images are in the real world. The resolution of the visual system is defined by Static Visual Acuity (SVA) and Dynamic Visual Acuity (DVA) for static and dynamic environments. Standard tests are available for SVA and form a major part of any eye exam. Commonly SVA is measured using the Snellen chart with reference to the Snellen fraction 20/20 ft. Thus, 20/20 vision requires that the subject can view an optotype 20 feet away that covers an angle one minute of arc. However, these results can also vary with contrast and illumination.

DVA is more complicated than SVA. There is no accepted standard test and it is generally not measured. Human abilities vary widely and DVA can be improved through training. Those used to tracking fast moving objects, such as athletes, commonly show more ability. Measuring DVA is also complicated by the Vestibulo-Ocular Reflex (VOR), an involuntary reflex where head movement is compensated by opposing eye motion to stabilise the image on the retina [Schml et al., 2000]. This stabilising reflex behaviour can be thought of as natural damping. Consequently, quantifying these limits is not an easy task.

Dynamic registration also has different requirements than static registration. When the head rotates at speed the world blurs as the brain can not process the information from the eyes fast enough. Clearly, highly accurate registration is not required in such situations. However, registration is still important, as it provides directional context allowing the user to rapidly search their environment and slow head motion when items of interest are detected.

Figure 1.5 illustrates schematically the drop in visual acuity or increase in allowable registration error with increasing dynamics. Studies suggest this relationship is a cubic function of optotype motion [Reading, 1972]. Existing registration techniques unfortunately are far from achieving this limit. However, if techniques could be improved such that registration was within the shaded region of the plot then the user would be unable to detect any registration error. This challenge effectively represents a “Holy Grail” for registration in AR systems.

Registration in AR is therefore, in its entirety, a very challenging problem. Ideally, registration would meet the DVA line in Figure 1.5. However, this goal is unachievable with current systems, and is not likely to be achieved in the near future. Holloway [1995] suggests in the future work section of his thesis that to achieve a registration error of 1mm, each error source should aim to achieve 0.1mm. He then defines specifications for 0.1mm and 1mm registration error in terms of tracking error alone. These specifications are summarised in Table 1.1.

Table 1.1: Tracking error specifications to achieve 1mm and 0.1mm registration error [Holloway, 1995]

Registration Error	Tracking Error		Latency (moderate head motion)
	Translational	Angular	
1.0 mm	0.5 mm	0.057 °	3 ms
0.1 mm	0.05 mm	0.0057 °	0.3 ms

1.1.3 Registration Error Sources within AR Systems

AR system errors are comprised of static and dynamic errors. Static errors occur due to optical distortions, misalignments between system components, tracker errors and incorrect viewing parameters. Dynamic errors are more complex, combining the sources of static error with the error induced by the system *latency*. Latency is the end to end time delay between finding the viewpoint and displaying the corresponding image to the user.

Latency increases dynamic error when the user is in motion because the rendered image no longer corresponds with the new viewpoint and thus, is no longer correctly aligned to the real world. Figure 1.6 illustrates schematically the application loop for a simple example of an AR system. The tracking system generates a 6DOF

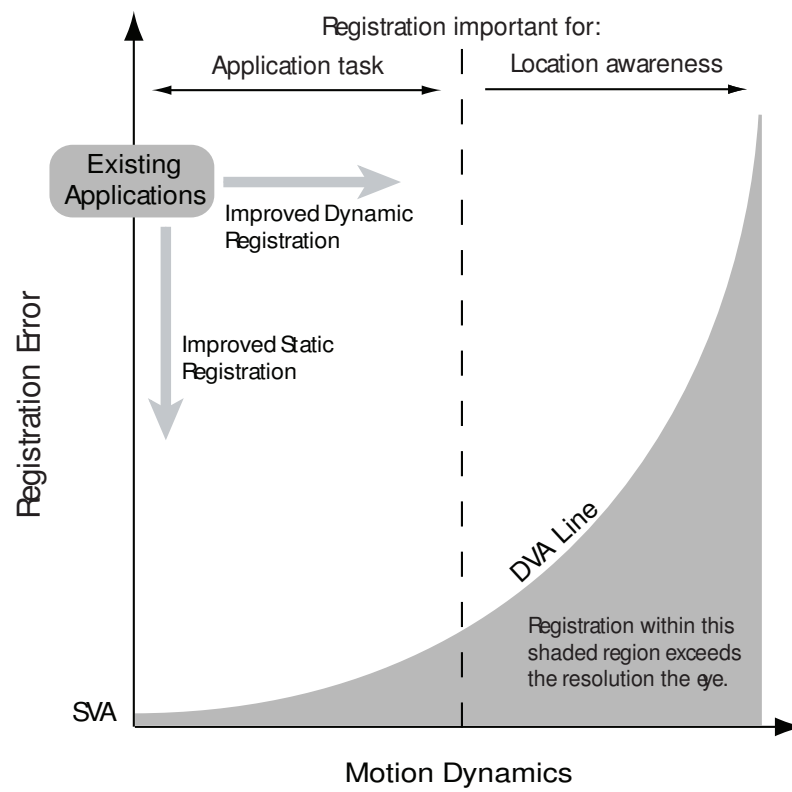


Figure 1.5: Schematic of Registration performance and Dynamic Visual Acuity (DVA)

viewpoint. Next, any simulations or calculations required for the new image are performed and passed on so the correct scene can be rendered. Lastly, the image must be written to the display so it can be observed by the user.

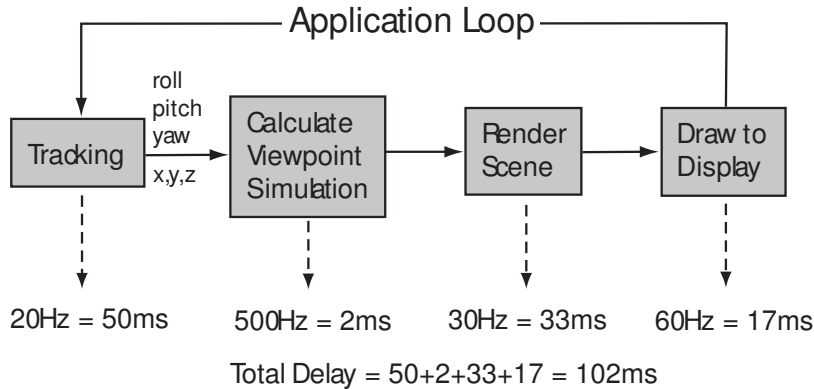


Figure 1.6: Latency in the AR system application loop

Examples of system latencies are shown in Figure 1.6. The total latency will contribute according to the motion of the user. As a very general rule, 1ms contributes to 1/3mm registration error. Thus, for this example the dynamic error would be 34mm. Latency can be reduced by using faster trackers, central processors (CPU), graphics processors (GPU) and displays. However, while tracker speed and display speed are not increasing quickly, the speed of CPUs and GPUs are improving very rapidly. This shows promise for improved performance in the future.

Changes in the tracking error and the latency also adversely affect performance of an AR system. This is termed *jitter* [Welch and Foxlin, 2002] and manifests itself as the virtual image shaking or twitching, thus destroying the illusion of registration. These changes are due to noise on the tracking signals or cycle to cycle variations of the latency.

1.2 Tracking Hand and Body Motion

Using the human body as an input device is seen as a natural way of interaction. This additional interaction can lead to a higher level of immersion and increased efficiency, while reducing demands on the user. Various techniques to track or interpret motion have been used. Gesture recognition is commonly performed using optical tracking. However, Tangible User Interfaces (TUI) [Ullmer and Ishii, 2000]

often utilise inertial tracking. An example of a recently commercialised TUI device is the Wii gaming console from Nintendo [Nintendo, 2007]. The Wii system has a wireless hand held remote that uses accelerometers and gyroscopes to sense the user's hand motion to control items in an interactive game.

With knowledge of the user's location and activity, intelligent computing systems can provide the user with relevant contextual information. Location based services have already been developed for cell phones. In the past, human body motion has commonly been captured using optical systems in the movie industry and in the study of biomechanics for sports science. Though, these systems are fixed and expensive, prohibiting collection of data in the natural environment.

Inertial sensors provide a cheap alternative. However, they do not provide the same level of accuracy as expensive optical systems. This lower accuracy is not a significant issue with detecting user activity (Randell [2000], Laerhoven and Cakmakci [2000]). However, accurately tracking position with inertial sensors alone proves extremely challenging. Most researchers combine inertial with some other form of sensor to combat drift caused by the accumulation of errors and noise in inertial measurements. Golding and Lesh [1999] use accelerometers and magnetometers with environmental sensors (light and temperature) and machine learning. Kouroggi [2003] analyses human walking behaviour and matches camera images to a database to aid in position determination.

1.3 Head Motion

An important part of developing an accurate viewpoint and head tracking method is understanding the dynamics of human head motion even in simplistic form. These dynamics help define part of the specification for the tracker, namely the range of motion required and maximum angular rates expected. Hardware designs can then be tailored to this application, focusing the bandwidth of the device and increasing the signal to noise ratio. Head motion analysis also has potential to aid in the development of predictive tracking algorithms, by potentially recognising characteristic signatures of head movement.

An adult human head weighs approximately 4.5-5kg and is supported by the neck above the shoulders. Motion and stability is achieved by neck musculature and

controlled by feedback from the muscles themselves and the visual and vestibular systems. Attaching items such as HMDs to the head changes the inertia of the head meaning the user must spend additional effort in turning the head [Shaw and Liang, 1992]. However, as technology improves it is expected that the hardware necessary for AR will become lighter and less obtrusive.

Like the motion of any object in 3D space, head motion has three rotational degrees of freedom and three translational degrees of freedom. Figure 1.7 shows these schematically. The maximum voluntary head rotational rates define the limits that any head tracking system must meet. However, values from the literature vary greatly from $360^\circ/s$ [List, 1984], to $2000^\circ/s$ [Aliaga, 1997], again indicating the difficulty in obtaining agreement for human measurements. These maximum rotational rates are unlikely to allow the human visual system to produce an image. Therefore, the demands for registration accuracy are greatly reduced from these values.

Head motion is very dependent on the application being performed. For example, a fighter pilot searching the sky for an enemy will have vastly different motion from a surgeon operating on a patient. Head motion is also complex, it can be very ordered one minute and very chaotic the next, making prediction very challenging. In his dissertation Azuma [1995] measured head motion for the specific application of people unfamiliar to HMDs walking through a room and handling interesting objects. His results for a fast and slow motion sequence are shown in Figure 1.8 as a cumulative density plot of angular velocity. This data shows that, for this application, most head motion is very slow with approximately 50% being below 10 degrees per second. In their frequency domain analysis of head motion Azuma and Bishop [1995] show that the majority of energy is below 2Hz, a result which is supported by other research for similar applications.

No one has yet analysed in depth head motion for highly dynamic AR applications, perhaps because few examples exist. Grossman et al. [1988] analyses head motion during locomotion. During running, median maximum head velocities did not exceed $90^\circ/s$ and had predominant pitch frequency of 3.2Hz. During vigorous voluntary head motion median frequencies for pitch and yaw are similar at 2.6Hz. While walking or running, motion in the pitch axis is much faster than the other two axes due to increased vertical acceleration acting on the head-neck system. Hirasaki et al. [1999] notes that significant head pitch develops at walking speeds above

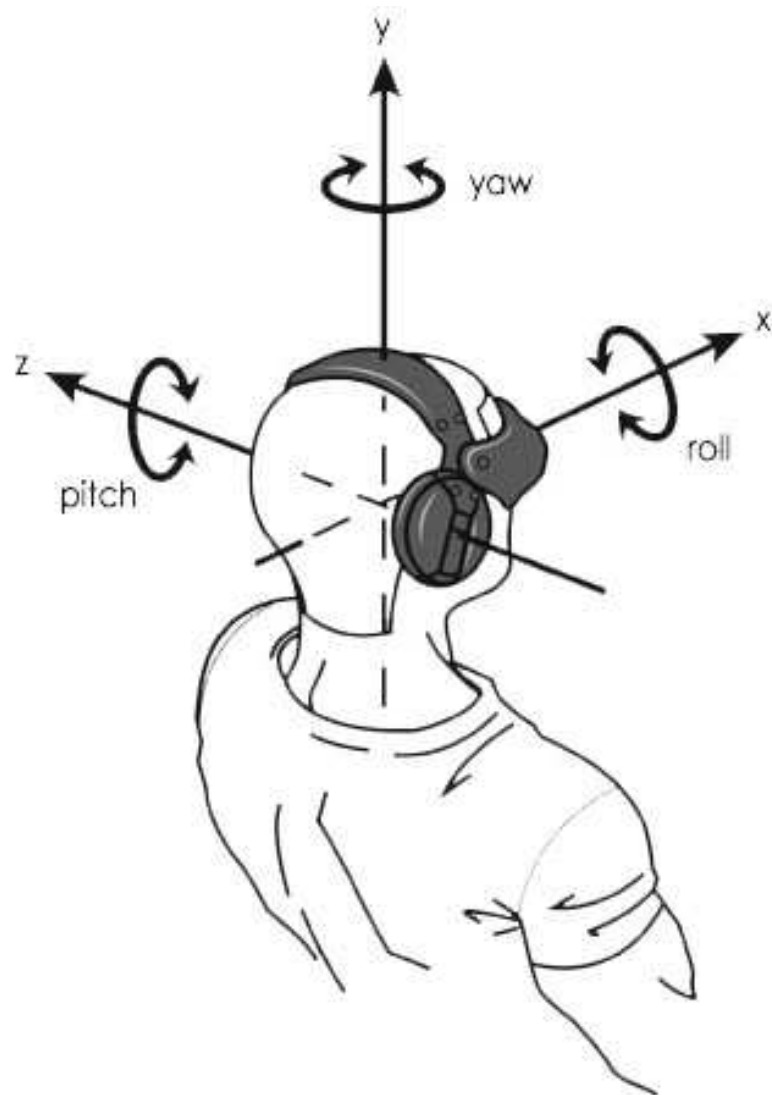


Figure 1.7: Head motion, 6 degrees of freedom, 3 translational (x,y,z) and 3 rotational (yaw, pitch, roll). Figure from Strickland [2007]

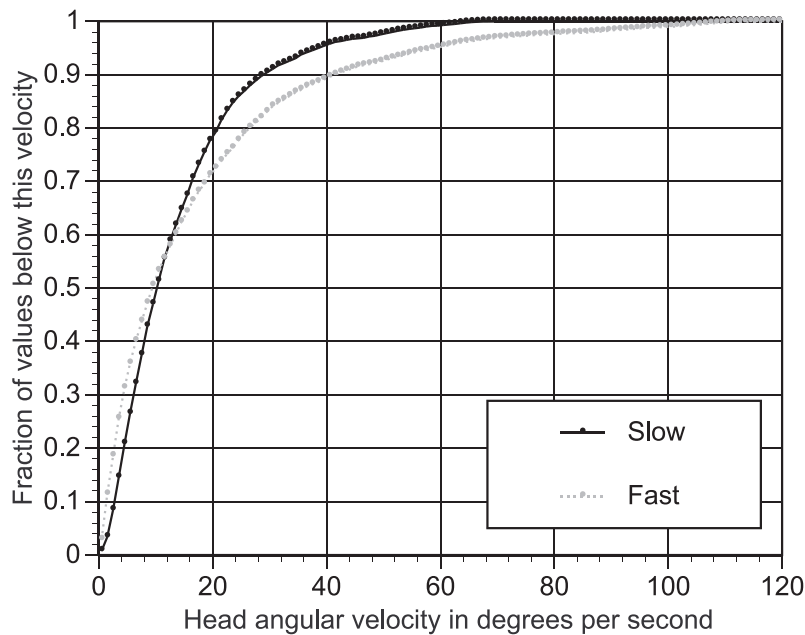


Figure 1.8: Cumulative density plot of angular velocity for fast and slow head motion sequences [Azuma, 1995]

1.2m/s. Clearly, tracking head pitch becomes very important for fully dynamic AR applications.

If the mechanics of the head are considered further it is possible to infer other characteristics of head motion. There is limited force that can be applied by the neck musculature to the head which has mass and therefore inertia. Thus, it is reasonable to expect that voluntary head motion will be smooth in nature. When viewing different objects, the arc traced by the head is that of the shortest length and therefore the most efficient path. The angular speed of the head illustrates that head motion is symmetric [Shaw and Liang, 1992]. This is because the muscles used to accelerate the head are also used to slow it down. Thus, the same amount of time is taken.

1.3.1 Application of Head Motion Models

Head motion models have found some modest use in head tracking for AR. Kalman (Azuma and Bishop [1995], Foxlin [1996]), extended Kalman [Chai et al., 1999], unscented Kalman [Kraft, 2003] and Particle [Fakhr-eddine Ababsa, 2003] filters have all been applied. These filters are used to combine noisy measurements from

different sensors to estimate, and sometimes predict, the system states including orientation. The filters require state or model equations from a head motion model. The models used are generally very simplistic rigid body motion models assuming constant angular rate or constant angular acceleration. To improve model accuracy the equations of motion for the head could be developed. However, head motion is driven by the forces from the neck muscles which are unknown. Thus, none of these systems truly model head dynamics, all use very simple approximations instead.

Head motion models have found use in other areas of research. Most applications are medical and used to provide better understanding of traumatic injuries or disorders that affect head motion. Gillies et al. [2003] uses an inverted pendulum model to explore the dynamics of head motion. Such models are commonly applied in studies of human posture and bipedal locomotion. Their model is verified with some experimental data, although they fail to solve the model for rotational angle over any useful time period. Specifically they state that large unphysiological values of orientation develop after 0.1s, but that these values would never be realised because of anatomical constraints.

1.4 Motion Tracking Technology

A review of the literature shows that no single technology provides good position and orientation for all applications. However, many different technologies and varied approaches have been applied to the problem of tracking motion. Each technology has its own strengths and weaknesses and these aspects ultimately drive the selection for each application. For AR tracking, cost, required accuracy, expected motion, required working volume, and the environment all impact on the selection of a tracking technology. Table 1.2 surveys the various different technologies and summarises their advantages and limitations in very general terms.

Welch and Foxlin [2002] provide a more in depth overview of each technology. They also consider the specification of an ideal tracking technology and note that inertial trackers are the closest technology to an ideal solution. This conclusion was developed because typical inertial sensors are small, inexpensive, have low latency, are sourceless, and are immune to most interference. However, the biggest limitation of inertial sensors and using them to derive displacement is that the results drift.

The advent of small size, low cost MEMS (micro electro mechanical systems) in the 1990's revolutionised inertial tracking. This development was initially driven by the automotive industry, although now MEMS inertial sensors are finding application in areas from consumer electronics to footwear. In the competitive market this technology is evolving rapidly. During the course of this doctorate several high accuracy accelerometers prominent in others research have become obsolete and more measurement axes than ever before are now available on one chip. For example, Analogue Devices Analogue Devices Inc [2007] has developed a IMU on a single IC chip that combines 3 orthogonal accelerometer axes with 3 orthogonal rate gyroscope (gyro) axes. Though at the time of writing these devices were not commercially available.

Drift is fundamental to the operation of inertial sensors. For MEMS gyros drift can be measured in $^{\circ}/s$. However, for larger more stable gyros drift is measured in $^{\circ}/hour$. Drift occurs because measurements from accelerometers and gyroscopes require integration to obtain position and orientation. Numerical integration of noisy signals accumulates the small errors and causes the results to drift. This drift has a tendency to increase with the number of integrations performed. For rate gyros this drift requires correction. However, with the accelerometer double integration causes drift that corrupts the position measurement. Hence, inertial devices may only be useful for tracking orientation in AR applications.

Accelerometers sense dynamic accelerations and also the static acceleration due to gravity. This second aspect enables accelerometers to also be used as effective tilt sensors. However, when other motion is introduced, the acceleration signal is modified by the dynamic accelerations, leading to orientation errors.

Table 1.2: Summary of tracking technologies

Technology and Description	Advantages	Limitations
<i>Mechanical:</i> The tracked target remains connected to a reference frame via a series of linkages. 6 DOF motion is measured physically using incremental encoders or potentiometers.	<ul style="list-style-type: none"> • Accurate • Immune to interference • No line of sight issues 	<ul style="list-style-type: none"> • Limited range • Very intrusive, affecting natural motion • Subject to mechanical wear • Expensive
<i>Magnetic - active:</i> A magnetic field is generated by passing current through orthogonal coils. This field is pulsed using AC or DC current. The sensor detects its alignment to the magnetic field, which is used to find 6 DOF position.	<ul style="list-style-type: none"> • Accurate • Inexpensive • No line of sight issues 	<ul style="list-style-type: none"> • Prone to ferromagnetic and electromagnetic interference • Range limited (room size) as accuracy reduces with distance. • High latencies
<i>Magnetic - passive:</i> Magnetometers measure 3 DOF orientation relative to the earth's magnetic field.	<ul style="list-style-type: none"> • Sourceless • Inexpensive • Small size • No line of sight issues 	<ul style="list-style-type: none"> • Accuracy limited (1-3°) as the earth's magnetic field is inhomogeneous. • Prone to ferromagnetic and electromagnetic interference
<i>Inertial:</i> 3 DOF orientation is determined from accelerometers and rate gyroscopes. Accelerometers sense acceleration and gyroscopes sense the rate of angular rotation. Inertial Measurement Units (IMUs) offer an integrated solution.	<ul style="list-style-type: none"> • Sourceless • Fast • Unlimited range • Immune to interference • No line of sight issues • Small size • Inexpensive (MEMS) 	<ul style="list-style-type: none"> • Drift • Generally not good for slow motion

Continued on Next Page...

Table 1.2 – Continued

Technology and Description	Advantages	Limitations
<p><i>Global Positioning System (GPS)</i>: Calculates the range to satellites using radio frequency, then triangulates a 3 DOF position. Real Time Kinematic (RTK) GPS uses the higher frequency carrier wave to get better resolution.</p>	<ul style="list-style-type: none"> • No drift • Large range (approx 10km from RTK base station) • Environment already prepared 	<ul style="list-style-type: none"> • Multipath interference. • Requires line of sight to satellites • Large antenna • Expensive
<p><i>Optical</i>: Often called vision tracking, a camera(s) captures 2D images of the target and image processing techniques are used to determine 6 DOF. The visual and infrared spectrums (with active or passive targets) are often used. Systems can be arranged with the camera(s) in the environment looking at the target (outside-in) or the camera(s) on the target looking at the environment (inside-out).</p>	<ul style="list-style-type: none"> • High accuracy achieved with fixed expensive systems • Good with slow motions • Immune to magnetic interference 	<ul style="list-style-type: none"> • Fixed systems have limited range • Line of sight required • Requires prepared or semi prepared environment (fiducial markers)
<p><i>Acoustic</i>: The distance between the emitters and microphones is calculated and the receiver's 3 DOF or 6 DOF position found using triangulation. Ultrasonic frequencies are used so that the signals can not be heard.</p>	<ul style="list-style-type: none"> • Inexpensive • Immune to magnetic interference 	<ul style="list-style-type: none"> • Ultrasonic noise interference • Low accuracy due to the variability of the speed of sound in air • Sensitive to environmental conditions • Multipath interference • Line of sight required

1.5 Overview of Head Tracking in Augmented Reality

Tracking head motion in AR is therefore a challenging problem. Many different approaches have been applied using the technology introduced in Section 1.4. Commercial solutions are available for; **Magnetic**: the Flock of Birds [Ascension Technology Corporation, 2007], Fastrak [Polhemus, 2008]; **Optical**: infra red ART system [Advanced Realtime Tracking GmbH, 2008]; and **Inertial**: the InertiaCube3 [Inetersense Inc, 2007], 3d-Bird [Ascension Technology Corporation, 2007], MTx [Xsens Technology, 2007], and the 3DM-DH [Micro Strain, 2007]. Computer vision techniques are also available in open-source software such as the ARToolKit computer vision library [Kato, 1999].

Fixed optical tracking systems are perhaps one of the most accurate technologies. These systems are ideal for highly controlled prepared environments, where they offer relative flexibility of motion to the user within the limited working volume. However, these systems are expensive and often cost prohibitive. Computer vision is an intensive area of research. This area is slowly evolving from tracking fiducial markers or matching images to a database to tracking natural features. However, for general AR applications in undefined spaces it still does not offer adequate solutions.

MEMS based inertial measurement units (IMUs) for tracking 3 DOF orientation have matured in recent years. The range of commercial options being evidence of this maturation. These IMUs typically contain three rate gyroscopes, accelerometers, and magnetometers. The gyros are used to determine orientation, while the accelerometers and magnetometers are used to correct for drift. However, these devices are a complex, and typically costly multi-sensor package.

In approaching simple, inertial based solutions, one approach is to take advantage of the burst like nature of head motion, and correct for drift only during natural pauses [Foxlin et al., 1998]. However, Luinge et al. [1999] shows that orientation is improved using accelerometers to aid the gyro during human kinetic measurement, but does not detail the motion. Some commercial IMUs do offer tailored filtering. However, they are not optimised for individual applications. None are yet fully proven in a highly dynamic environment.

These single technology approaches do not currently provide satisfactory tracking solutions for all applications.

1.5.1 Compensating for Registration Error

Consistent static errors mentioned in Section 1.1.3 can be compensated by employing various calibration techniques (Janin [1993], Bajura and Neumann [1995]). However, this correction is not possible for dynamic errors. Both dynamic tracking error and latency induced dynamic error can not be calibrated for, and thus must be addressed in the data.

Various approaches have been taken to reducing or minimising the effect of latency. As technology continues to improve, faster processors will reduce system lag. Some researchers implement methods to reduce apparent lag by updating the virtual image position [Kijima, 2002] or warping the image [Mark et al., 1997] after it has been rendered. Therefore, they take greater advantage of more up to date tracker information.

Video see through HMDs overlay the virtual content on a video of the real world. A common technique employed with these displays is to delay the video signal to match the system lag [Bajura and Neumann, 1995]. This approach reduces registration error and can work well for slow motions. However, at faster speeds it causes a sensory mismatch between the vestibular system and visual system. This mismatch can become uncomfortable for the user and lead to simulator sickness, which is a common problem in VR.

Predictive tracking aims to reduce this latency by predicting where the users viewpoint will be ahead of time [Azuma and Bishop, 1995], enabling the correct imagery to be rendered and displayed to the user coinciding with the actual viewpoint. Prediction error increases roughly with the square of the prediction interval. Prediction is also fundamentally limited by the inertia of the head and the torque or force that can be applied to it. Holloway [1995] suggests this effect is limited to 80ms considering the data from Azuma and Bishop [1995]. Even with increased computing power, tracking and rendering will take a finite amount of time. Thus, registration will always be improved by good prediction provided it can be implemented effectively.

1.5.2 Hybrid Tracking Systems

A great deal of recent development has been focused on developing hybrid tracking systems, effectively exploiting and combining attributes of different technologies. The objective of any hybrid tracking system is to provide a tracking solution with better performance or more flexibility than each of the contributing technologies possess individually. One of the most common approaches is to combine inertial and vision technologies, effectively replicating human tracking with our visual and vestibular systems. These technologies complement each other well with vision working well for slow motions and inertial tracking better at faster motions. Integration also allows the inertial system to be used to reduce the search space for visual features in subsequent frames. Both of these technologies can be sourceless showing potential for use in unprepared environments.

Examples of vision-inertial hybrid trackers in prepared indoor environments are given in Azuma and Bishop [1994], You and Neumann [2001], Lang et al. [2002], Foxlin and Naimark [2003]; in unprepared indoor environments, Azuma et al. [1999], You et al. [1999a]; and in unprepared outdoor environments You et al. [1999b], Satoh et al. [2001], Ribo et al. [2002]. These systems are evolving as vision techniques move from tracking fiducial markers or infra red LEDs to tracking natural features. However, during highly dynamic motion the hybrid systems rely on the inertial system, thus are reduced to the same issues described in Section 1.4.

For outdoor systems the addition of GPS position measurements can be useful. Standard GPS in most consumer products has low accuracy, about 10m. This accuracy can be improved using corrections to about 3m with differential GPS. However, real time kinematic (RTK) GPS achieves centimetre precision. Currently, these systems are very expensive, however some networks are being set up in some cities, such as Sydney, Australia [Rizos et al., 2004].

However, GPS is reliant on line of sight to satellites, which can be disrupted in urban environments. Tall buildings and structures can block satellites meaning no position can be determined and reflected signals can cause multipath disturbance giving an erroneous position. These issues along with the size of RTK GPS antennas mean that GPS will not suit all outdoor applications. Outdoor applications using GPS combined with inertial tracking include: Roberts et al. [2002] and Piekarski and Thomas [2002].

Other hybrid approaches researchers have taken include: Magnetic-Vision [State et al., 1996], [Auer et al., 1999]; Inertial-Acoustic [Foxlin et al., 1998]. These approaches are limited to indoor prepared environments, and thus not suitable for the targeted applications of this thesis.

With all hybrid approaches sensor fusion also becomes important. More specifically, it addresses the issues of how to combine data from different sources, often collected at different rates, to form one distinct position and orientation. Kalman filters are the most popular approach in the literature to fusing data from different sources. These filters utilise a state model, as discussed in Section 1.3.1. However, the Kalman approach typically does not easily accommodate data at different rates. Welch and Bishop [1997] develop a technique that utilises each low level measurement, as it is made, offering higher update rates, lower latency and with improved accuracy.

However, while hybrid systems can improve tracking performance and flexibility, it is often at the expense of increased system complexity and cost. It also implies a need for dependency on multiple sensor types. This thesis seeks to breach that compromise by developing an inertial approach and initial methods for orientation tracking of pitch and roll using only inertial data. As described it would have use in a number of applications and systems, including hybrid sensor systems, if a reasonably robust and accurate method, or approach to the same could be developed.

1.6 Preface

Many head or viewpoint tracking methods exist, although typically these perform relatively poorly or are unsuitable in highly dynamic environments that many AR applications seek to expand into. Thus, applications in these more challenging environments, such as outdoors, are not well catered for by existing commercial tracking solutions. To fully enable AR growth, what is required is low cost approaches based on simple, existing sensor platform technologies.

The key objective for this thesis was to improve dynamic orientation tracking of the head using low cost inertial sensors. However, a more general research approach is taken that does not limit the outcomes specifically to head tracking for AR. The methods applied extend the excellent static orientation sensing abilities of

accelerometers to a dynamic case by utilising a model of head motion. The inverted pendulum model applied, and the solution methods are investigated and validated for the case of a two dimensional system in the following chapters.

Chapter 2

Head Motion Modelling and Validation

As shown in Section 1.3, accurate models have not been applied to the head motion tracking problem for a variety of reasons. In this chapter, a model of the fundamental dynamics involved in rotation of the head is developed and matched to experimental sensor data. Given noisy or uncertain sensor data the use of the model has the potential to significantly improve tracking performance, especially for highly dynamic applications with or without limited sensor data or tracking technologies.

2.1 The Inverted Pendulum Model

An inverted pendulum model applies where a mass is balanced above an axis of rotation. In this application, the mass is a human head, which is supported above the shoulders by the cervical spine. This balanced equilibrium state is intrinsically unstable. In the classical inverted pendulum problem, balance is maintained by continuously moving the fulcrum under the centre of the pendulum mass. However, head stability is maintained by moments applied by the neck musculature, a very different situation.

The head-neck system is modelled using an inverted pendulum for one rotational degree of freedom in a vertical plane. This simple model corresponds to either a single pitch or roll motion of the head. A dual axis accelerometer is positioned along the pendulum, aligned in the plane of rotation. Generally in most applications the amplitude of head rotations are small as extreme displacements are uncomfortable. An integral based fitting method that could be extended to find the optimal radius is discussed in Section 2.3.2. For applications where extreme displacements are

common the radius of rotation may be more accurately represented as a function of the rotation. However, for this proof of concept, the assumption is made that the radius of rotation for the head is fixed.

Figure 2.1 shows a schematic for the model. A particle at radius R undergoing rotation $\theta(t)$ is subjected to tangential, centripetal and gravitational (g) accelerations. These accelerations are sensed by the accelerometer axes $A_y(t)$ and $A_x(t)$ oriented at a fixed angle λ to the tangent of rotation. With the pendulum near vertical, optimal sensitivity to gravity for both accelerometer axes is achieved when $\lambda = \pi/4$. This placement also ensures the dynamic components of accelerations are sensed by both axes, thus averaging the effects of the noise on each independent accelerometer measurement.

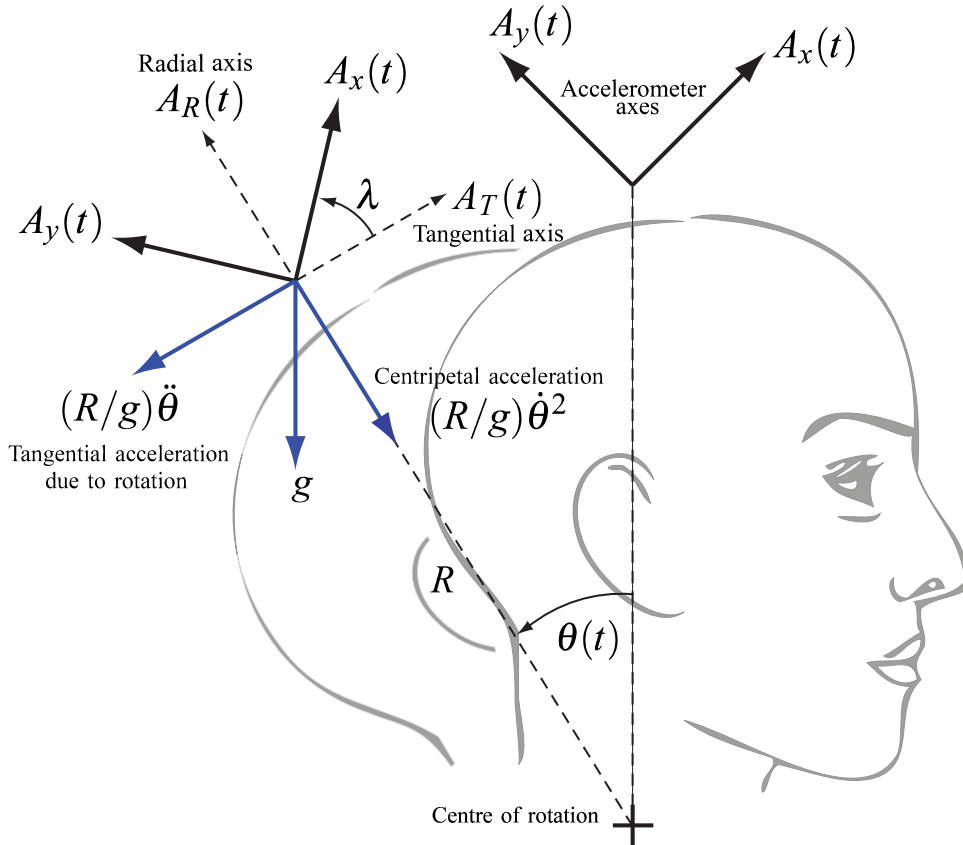


Figure 2.1: Acceleration vector diagram for a point at the end of an inverted pendulum, length R , undergoing a rotation of θ . Note the sign convention for rotation is positive in an anticlockwise direction from the vertical.

The accelerometer senses the acceleration of its proof mass relative to its casing. Hence, dynamic accelerations contribute in the opposite direction to that shown in Figure 2.1. Resolving acceleration in terms of g along the tangential and radial

axes provides two independent ordinary differential equations (ODEs) for $A_T(t)$ and $A_R(t)$. Note that all accelerations and rotations ($\ddot{\theta}$ and $\theta(t)$) are functions of time and that the “(t)” is now dropped for clarity.

$$A_T = (R/g)\ddot{\theta} - \sin(\theta), \quad (2.1)$$

$$A_R = (R/g)\dot{\theta}^2 - \cos(\theta). \quad (2.2)$$

The actual tangential (A_T) and radial (A_R) accelerations are derived from the measured accelerations:

$$A_T = A_x \cos(\lambda) - A_y \sin(\lambda), \quad (2.3)$$

$$A_R = A_x \sin(\lambda) + A_y \cos(\lambda). \quad (2.4)$$

It is important to note that Equations (2.1) and (2.2) are not equations of motion, and thus are independent from any inertia, actuation force, damping or physiological limits that may influence the motion. The effect of any such terms will directly contribute to the measured acceleration and is therefore captured by this model. This approach frees the problem from complex calibration or system identification procedures.

2.2 Accelerometers

To implement and validate the model a MEMS accelerometer must be selected. There is an extremely wide variety of these devices available. Most are currently manufactured using surface micro-machining and operate by detecting the displacement of a constrained proof mass with capacitive sensors. Analogue Devices Inc. [Analogue Devices Inc, 2007] is a leading manufacturer of these devices.

An alternative to a constrained solid proof mass is to use a gaseous proof mass. These are termed thermal accelerometers and examples are manufactured by MEMSIC Inc. [MEMSIC Inc., 2008]. Thermal accelerometers are less complex to manufacture and overcome issues, such as stiction, when a solid proof mass is used. These devices heat a small pocket of air and sense its movement within higher density surrounding air using thermopiles. Acceleration is then determined from the temperature gradient.

MEMS accelerometers continue to improve in accuracy and performance. There is a clear trend to further integration with the first 3 axis accelerometers and more recently 3 axis IMUs becoming commercially available. This continuous improvement will allow even smaller and less obtrusive implementations which bodes well for emerging applications for head tracking.

2.2.1 Static Tilt Sensing Using Accelerometers

Static tilt sensing using an accelerometer is a trivial problem. As the accelerometer is stationary the only acceleration it senses is due to gravity. The amount of gravitational acceleration sensed by the accelerometer axis indicates the angle of the device to the gravitational vector. This situation is illustrated in Figure 2.2.

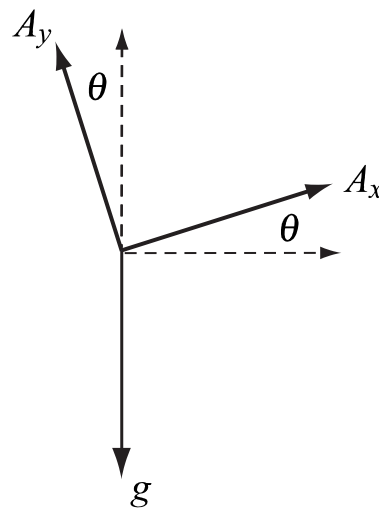


Figure 2.2: Using accelerometers to measure static tilt

Theoretically, only a single axis is required to sense tilt for one rotational degree of freedom as in Equation (2.5). However, the change in acceleration per degree reduces as the angle between the accelerometer axis and the gravitational vector increases. The resolution changes from approximately $17.45mg/^\circ$, when perpendicular to gravity to only $0.15mg/^\circ$ when the axis is parallel to gravity. This reduction in resolution is not important if only small tilt angles are expected.

$$\theta = \arcsin(A_x) \quad (2.5)$$

Head motion can have large rotations. Using two axes to sense one degree of tilt, as shown in Equation (2.6), provides a more robust result. This method maintains optimal resolution through full rotation.

$$\theta = \arctan(Ax/Ay) \quad (2.6)$$

Applying either of these simple equations to static or quasi-static rotations can easily determine static pitch and roll. These simple techniques are being used in PDAs and other devices to enhance user interfaces with new functionality, such as tilt initiated scrolling.

2.2.2 Selection and Testing of Accelerometers

The head tracking application requires accelerometers with high accuracy when undergoing small accelerations. This type of motion is challenging for inertial sensors. Therefore, it is important to select an appropriate accelerometer. Key specifications to consider include:

- *measurement range* which must be selected such that it does not saturate during motion;
- *sensitivity* which is related to the measurement range. This parameter represents the amount of output signal per g ;
- *noise performance* which is critical when working with small accelerations.

A range of suitable low acceleration accelerometers were selected. These sensors included thermal and capacitive types along with digital and analogue outputs. These are listed below and key specifications are summarised in Table 2.1.

- **ADXL202**; Low cost $\pm 2g$ Dual Axis Accelerometer with Duty Cycle Output from Analog Devices.
- **ADXL203**; Precision $\pm 1.7g$ Dual Axis Accelerometer from Analog Devices.
- **ADXL213**; Low cost $\pm 1.2g$ Dual Axis Accelerometer from Analog Devices.
- **MXD2020E**; Ultra Low Noise, Low offset Drift $\pm 1g$ Dual Axis Accelerometer with Digital Outputs from MEMSIC Inc.

Table 2.1: Key specifications for the selected accelerometers

Device	Output	Measurement Range (g)	Sensitivity	Noise Density ($\mu g/\sqrt{Hz}$)
ADXL202	Digital	2.0	12.5%/g	200
ADXL203	Analogue	1.7	1000mV/g	110
ADXL213	Digital	1.2	30%/g	160
MXD2020E	Digital	1.0	20%/g	200

Acceleration is calculated from the output signal of the accelerometers using the general Equation (2.7). Thus, it is important to have accurate knowledge of the zero g output and the sensitivity of the device axes.

$$Acceleration = \frac{Output - ZeroG\ Output}{Sensitivity} \quad (2.7)$$

where *Output* is the the duty cycle or the voltage output and *ZeroG Output* is the zero g duty cycle or voltage output.

Noise Performance

The bandwidth of the accelerometers was set to 10Hz by selecting the external circuitry components. This choice tailored the devices to the low frequency head tracking application. Two of each device (except the ADXL202, as only one was available) were calibrated using the procedure described later in Section 2.2.3. The theoretical noise floor was calculated using Equation (2.8) and compared to the experimental noise floor of each device axis. These values are compared in terms of g in Figure 2.3.

$$rmsNoise = (Noise\ Density) \times (\sqrt{BW} \times 1.6) \quad (2.8)$$

where the *Noise Density* is listed in Table 2.1 and *BW* is the bandwidth the device is set to.

The results show that it is difficult to achieve the noise performance specified for the devices by their manufactures. Signals can be corrupted by many noise sources within the laboratory environment. Generally, the Analogue Devices accelerometers outperform the thermal accelerometers from MEMSIC. The ADXL202 accelerometer clearly shows the best performance experimentally and is closest to its theoretical

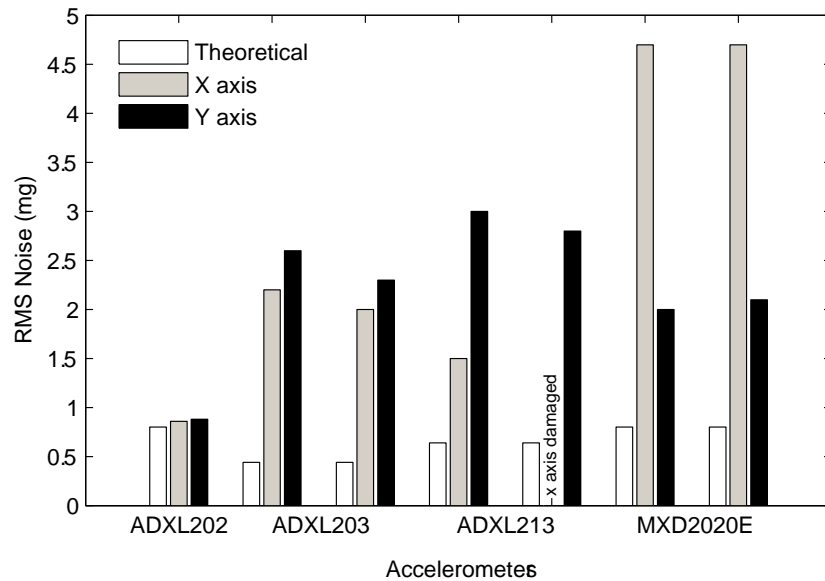


Figure 2.3: Comparison of theoretical and experimental accelerometer noise performance

noise floor.

The failure of the x axis of the second ADXL213 accelerometer illustrates that these MEMS accelerometers are fragile and need to be handled with care. The MEMSIC devices are more robust in this respect, having greater shock survival rates.

Both manufacturers products show some disparity in the noise floor for each axis. The layout of the accelerometers internal circuitry is likely to be the reason for this disparity. This difference is most extreme with the MXD2020E, where the x axis has approximately twice the noise of the y axis. Upon communication with MEMSIC Inc., it eventuates that this difference is normal behaviour despite the noise specification being the same for both axes.

Temperature Compensation

Accelerometers are subject to thermal variation. For high accuracy applications the thermal drift in the zero g bias must be compensated. Application notes are available from the manufacturers showing thermal compensation techniques (Weinberg [2002], Dao [2002]). MEMSIC accelerometers have consistent thermal behaviour for each model. However, each Analogue Devices iMEMS accelerometer has a unique temperature characteristic that is approximately linear.

A small temperature chamber was developed to test the zero g duty cycle temperature drift. A thermoelectric Peltier element was used to provide heating and cooling. Temperature was controlled using feedback from a thermocouple and the dSPACETM rapid development suite in the lab. Figure 2.4 illustrates the drift for each axis of the second ADXL213 accelerometer. All except one accelerometer axis showed similar linear trends with temperature.

This work shows that temperature compensation of accelerometers is important to deliver the robustness and accuracy required. Provided a temperature source is available in the hardware this compensation would not be difficult to implement. However, it will require calibration for each device and does make the system more complex. At this early stage, more importance is placed on proving the concept that motion can be tracked using accelerometers and the model developed. A simple yet accurate way to account for the variation due to temperature, in this situation, is to perform the calibration procedure in Section 2.2.3 each time data is collected. This approach provides calibrated results for each axis of the device at the testing temperature, avoiding the complexity of implementing a full temperature compensation method.

Dynamic Performance

For the Analogue Devices ADXL series MEMS accelerometers, the dynamic performance is dominated by the output filter response. The ADXL202 accelerometer bandwidth is set to 10Hz by an external $0.47\mu\text{F}$ capacitor (C). The phase response can be calculated using Equation (2.9) which is taken from application note AN-688 [Weinberg, 2004].

$$\text{Phase Response} = -\arctan(\omega RC) \quad (2.9)$$

where $\omega = 2\pi f$, and the internal resistor $R = 32k\Omega$ in this case.

Experiments were conducted to verify this response. The accelerometer was mounted on a voice coil actuator as seen in Figure 2.6 and driven in a sinusoidal motion at various frequencies. The x axis of the accelerometer was aligned with the motion. A laser doppler system was used to measure velocity of the accelerometer motion and upon integration provide an independent measure of acceleration. Comparing the accelerometer reading to the acceleration derived from the laser measurement system allows the phase lag and magnitude response to be determined.

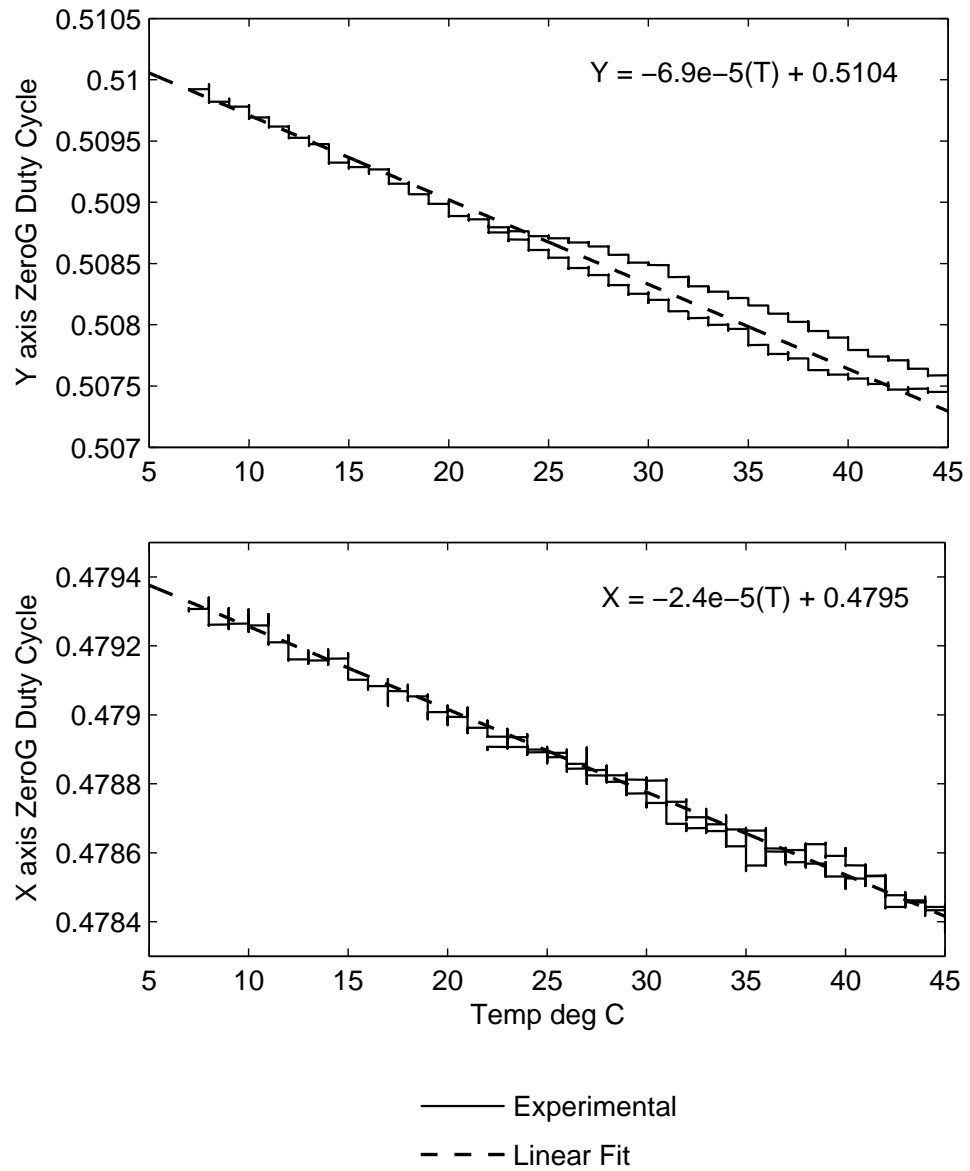


Figure 2.4: Zero g duty cycle drift with temperature for the second ADXL213 accelerometer. Note, that the y axis of each plot have different scales.

Unfortunately, the voice coil does not follow the sinusoidal driving signal perfectly and suffers from some stiction. This causes small noise like disturbances in the acceleration and velocity signals and is especially evident at slower frequencies. However, filtering the acceleration from the accelerometer and the velocity from the laser measurement system prior to differentiation allows comparison of smooth acceleration signals.

A comparison of filtered signals was made for 1,2,5 and 10Hz excitation frequencies, allowing the experimental magnitude and phase response to be determined. The theoretical phase response can be calculated using Equation (2.9). These parameters are compared in the Bode plot in Figure 2.5 and show good agreement between experimental and theoretical phase shift.

2.2.3 Accelerometer Calibration Procedures

Due to the inevitable variation in manufacture, MEMS accelerometers require individual calibration for optimal performance. The accelerometers selected have nominal zero gravity outputs and sensitivity. However, for high accuracy applications nominal values do not provide optimal performance. This simple calibration procedure determines both the zero g output and sensitivity specific to each device axes. The procedure works for both analogue and digital accelerometers. However, in this case it is demonstrated for two digital ADXL213 accelerometers.

Equation (2.7) shows the reliance acceleration has on the zero g reference output and the sensitivity of the device. Calibration to determine these values accurately involves rotating the accelerometer axes in a precisely vertical plane. The rotation must be performed very slowly to avoid any contribution from centripetal or tangential accelerations. To achieve this rotation, an indexing table from a mechanical workshop is used. Accelerometers are mounted to the surface as illustrated in Figure 2.7. When mounted on a level isolation table the high tolerances of the indexing table ensure that the accelerometers are precisely in a vertical plane.

Winding the hand wheel causes the table to rotate and the data from the accelerometers is collected. The slow motion means that each axis will pass directly through the vertical axis. Thus, a full rotation will yield a measurement at $1g$ and $-1g$. Assuming a linear sensitivity within the device then both the sensitivity and

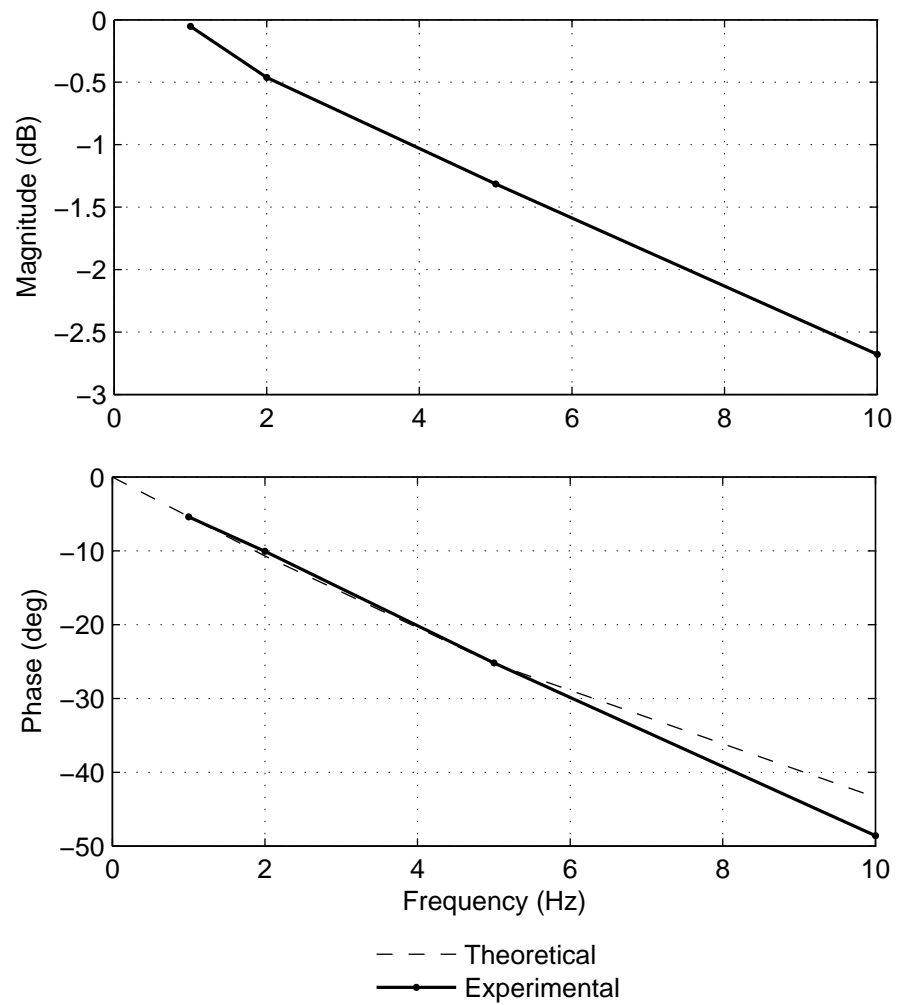


Figure 2.5: Bode plot showing phase and magnitude response for the ADXL202 accelerometer. Note, no theoretical line is available for the Magnitude response.

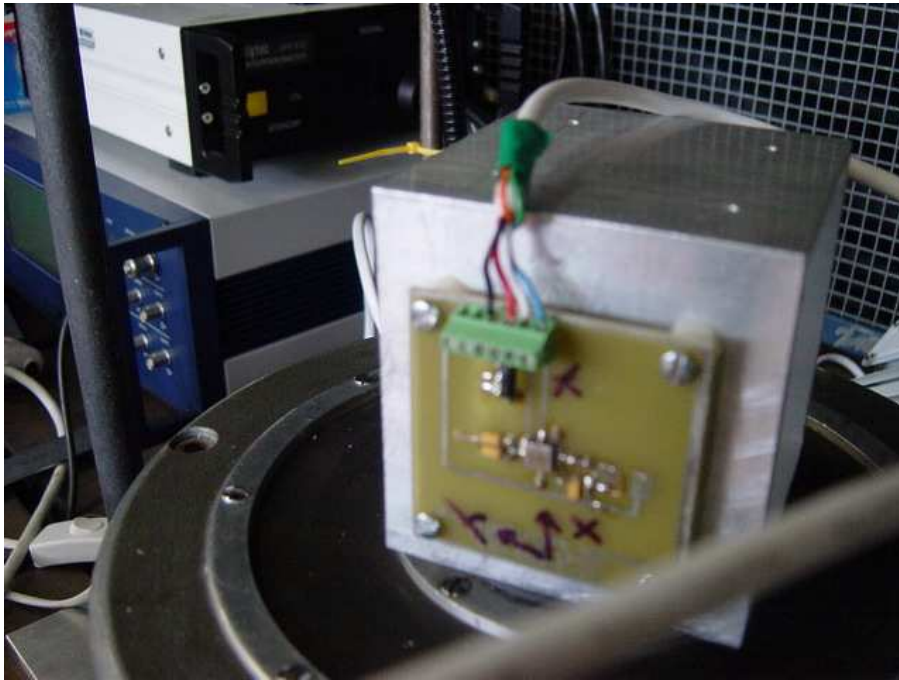


Figure 2.6: Dynamic response testing, ADXL202 accelerometer mounted on voice coil actuator with laser doppler measurement equipment in the background

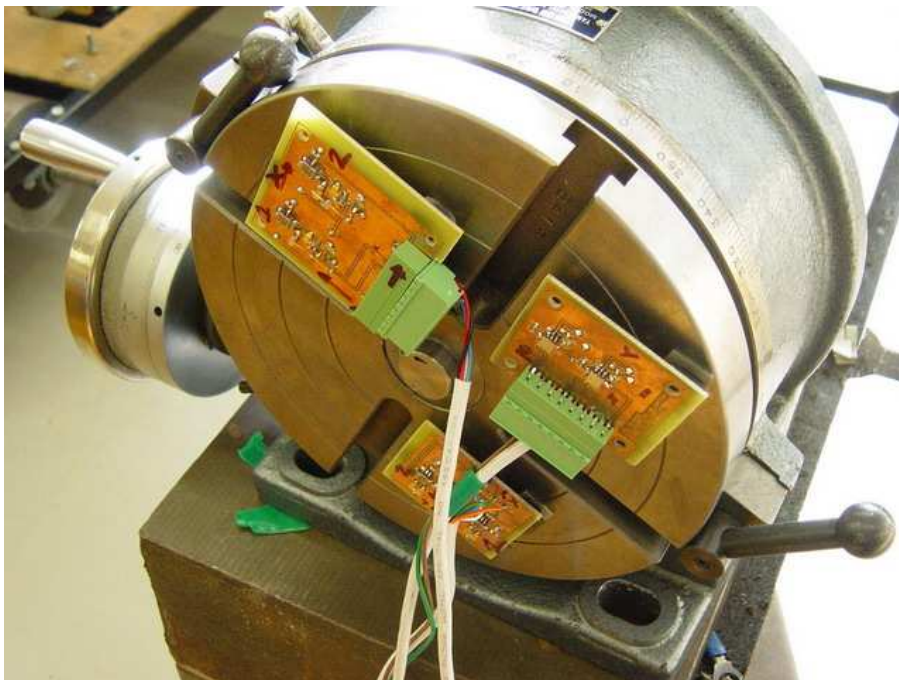


Figure 2.7: The indexing table with accelerometers attached for calibration

zero g reference output can be determined. The mid point being the effective zero g output and the range divided by $2g$ being the sensitivity.

Figure 2.8 plots the output from an ADXL213 accelerometer for the described acceleration procedure. Calibration results for two ADXL213 accelerometers are summarised in Table 2.2. The difference between the X and Y axes on the first accelerometer illustrate how much variation can exist. Un-calibrated, these differences would propagate through acceleration as errors reducing the accuracy of the orientation.

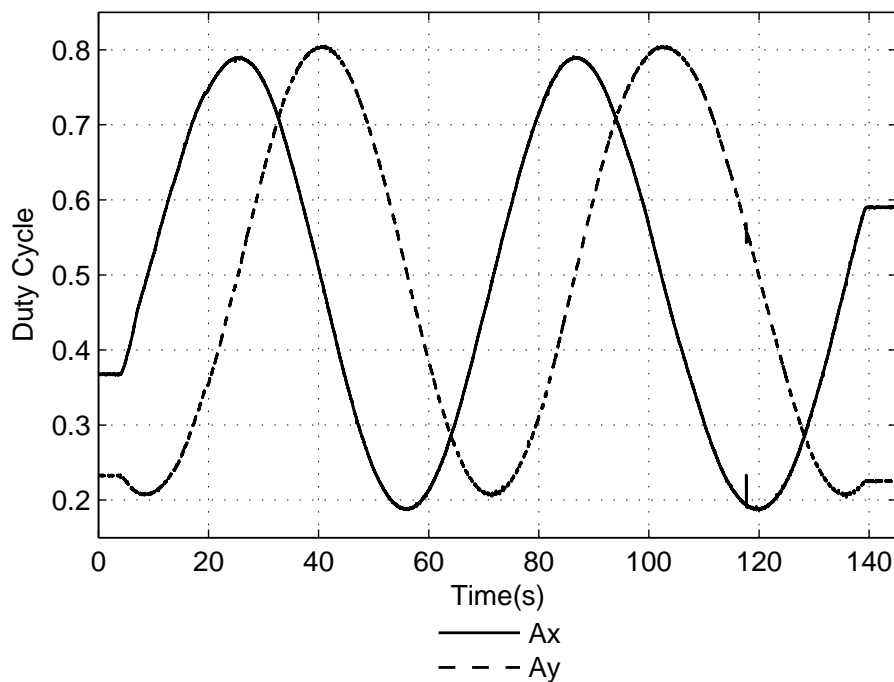


Figure 2.8: The output from the first ADXL213 accelerometer during calibration at 21 °C

Table 2.2: Calibration Results at 21°C

	Axis	Mean Duty Cycle $1g$	Mean Duty Cycle $-1g$	Zero Gravity Duty Cycle	Sensitivity (DC/g)
Accelerometer 1	X	0.78905	0.18780	0.4884	0.3006
	Y	0.80370	0.20770	0.5057	0.2980
Accelerometer 2	X	0.80215	0.19920	0.5007	0.3015
	Y	0.80190	0.20150	0.5017	0.3002

The accelerometer is the critical piece of hardware for the model based tracking approach presented and used in this thesis. Initially, the ADXL202 was used for experimental testing as it had the lowest noise floor. However, this accelerometer

was damaged and substituted with the ADXL213 as it had the same digital output. These accelerometers were readily available in the robotics laboratory used for testing, so using them prevented delays in sourcing more ADXL202 accelerometers.

2.3 Verification of the Model Using the Inverted Pendulum

With the important accelerometer hardware selected the model developed in Section 2.1 can be evaluated. The goal is to verify that model Equations (2.1) and (2.2) fit with experimental data collected using a physical inverted pendulum and attached accelerometers.

2.3.1 Method

An existing inverted pendulum apparatus was used with an optical encoder providing an independent measure of rotation, θ_{en} . The encoder used had a resolution and nominal angular position error of 0.17° . This setup is seen in Figures 2.9 and 2.10. The cart position was fixed with a clamp to limit motion to the one rotational degree of freedom of the pendulum.

The ADXL213 dual axis accelerometer was attached to the pendulum at radius $R = 0.3\text{m}$, the approximate radius for a device mounted on top of the head, and at an approximate angle $\lambda = 45^\circ$. It is important to accurately determine the accelerometer orientation on the pendulum, as error in λ will cause an offset between the orientation obtained from the encoder and that found via the accelerometer. The following setup procedure is used:

1. Calibration data for the accelerometer is collected using the procedure in Section 2.2.3. The zero g offset and sensitivity values can be applied to the accelerometer outputs in post processing, meaning that all experimental data can be collected in one session.
2. The encoder zero point is initialised by building the Simulink model to a dSPACETM system with the pendulum hanging stationary under its own weight.

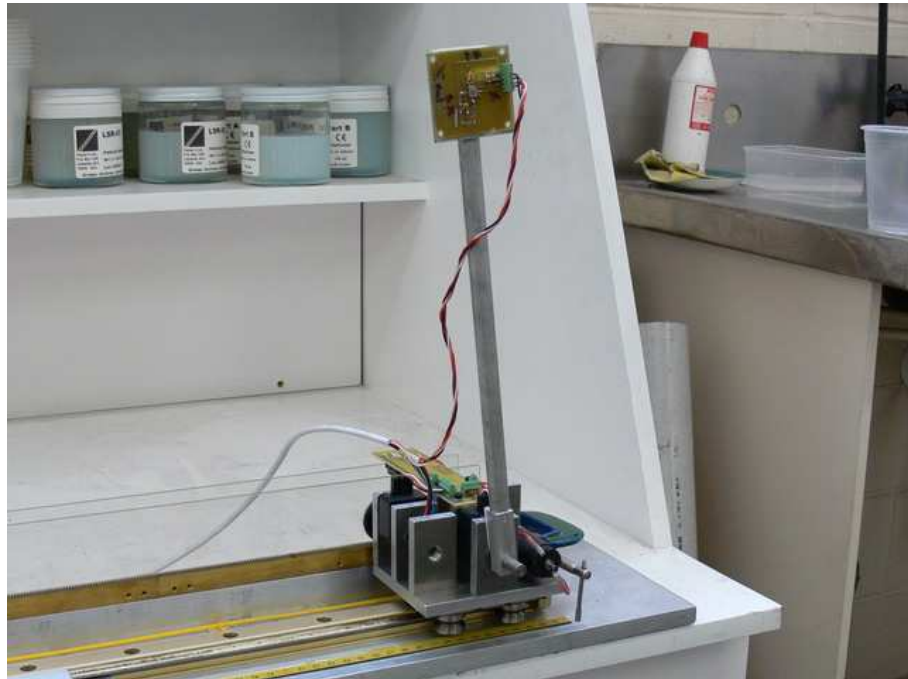


Figure 2.9: The inverted pendulum laboratory equipment with accelerometer attached

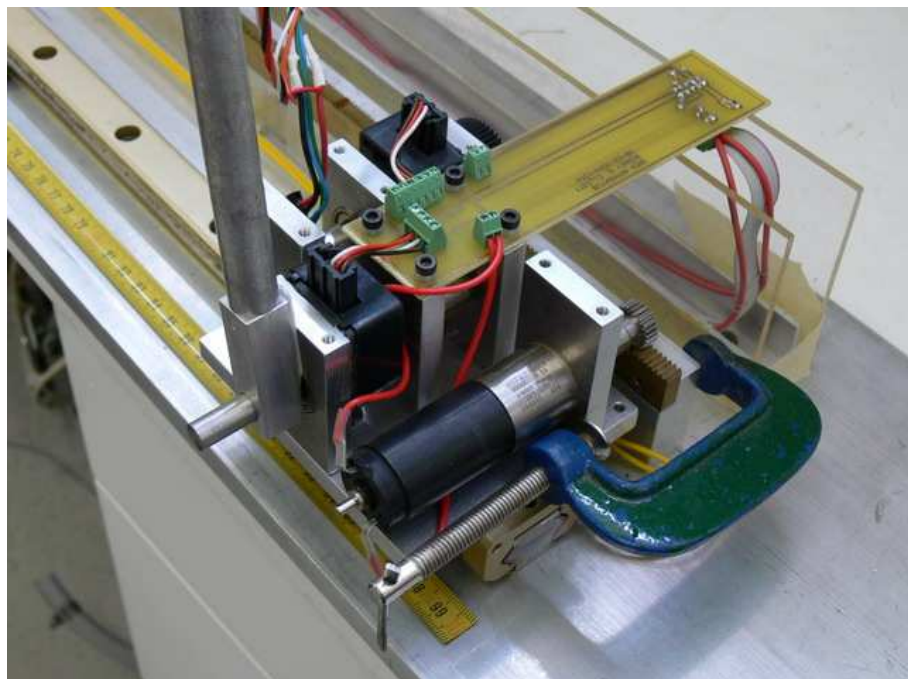


Figure 2.10: The inverted pendulum laboratory equipment showing the optical encoder and cart clamped in place

This procedure sets the direction straight down as $\theta = 0$ for the encoder, which can be modified to match the accelerometer model by adding π .

3. Attach the calibrated accelerometer to the pendulum at the desired radius and approximate angle λ to the pendulum. The true λ can be calculated provided that the pendulum is stationary using Equation (2.6) and the encoder angle. However, it is important to ensure that the centre of the pendulum is inline with the centre of the accelerometer package.

Data was collected while manually oscillating the pendulum in relatively slow motions similar to typical head motions. Attaining exact frequencies was difficult. However, performance improved markedly when aided by audible beeps. The following assumptions are made in this validation of the model:

- the point of rotation is fixed;
- the accelerometer is mounted exactly in the plane of motion;
- no out of plane motion occurs;
- the centre of the accelerometer is aligned with the centre of the pendulum.

2.3.2 Results and Discussion

Estimates of the true A_R and A_T were generated using θ_{en} and the model Equations (2.1) and (2.2). To combat the buildup of noise due to the differentiation of θ_{en} , this signal was filtered to smooth the steps caused by the finite resolution of the encoder. The measured accelerations A_x and A_y were resolved along the tangential and radial axes using Equations (2.3) and (2.4). A comparison of the model acceleration with the measured accelerations is shown in Figure 2.11.

The mean, standard deviation (STD) and percentage errors are summarised in Table 2.3. A percentage error of 5.4% relative to the mean amplitude shows a good fit between the measured tangential acceleration and the model. However, 21.9% shows the error is much worse for the radial acceleration due to poor sensitivity to orientation when this axis is near vertical.

To determine the accuracy of the model fit to the experimental data in terms of

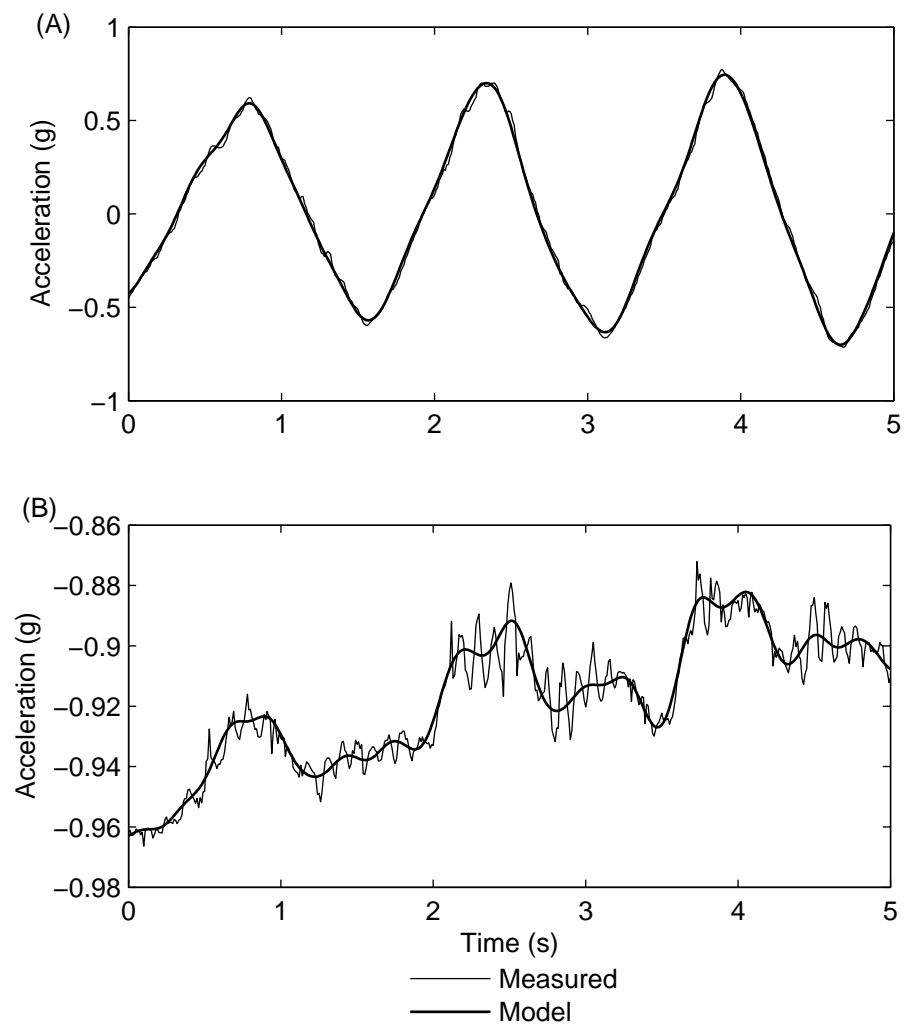


Figure 2.11: Measured and model accelerations: (A) Tangential acceleration, A_T ; (B) Radial acceleration, A_R

Table 2.3: Angular and acceleration model error

Error Measure	Acceleration		Angular
	A_R (mg)	A_T (mg)	θ (deg)
Mean	3.8	20.1	0.17
STD	3.4	13.7	0.04
Mean %	21.9	5.4	1.1

θ , independently from the solution method and noise, Equation (2.1) is integrated:

$$\theta = \frac{g}{R} \int_0^t \int_0^t A_T + \frac{g}{R} \int_0^t \int_0^t \sin(\theta) + t\dot{\theta}(0) + \theta(0) \quad (2.10)$$

Fitting Equation (2.10) to the experimental data determines the optimal initial conditions $\dot{\theta}(0)$ and $\theta(0)$. This method could also be used to find an optimal R value for later calibration procedures, but here the measured R is used. Evaluating the fit allows an estimate of the model error in terms of theta to be calculated.

The model error is evaluated for each subsequent 0.3 second period, as this is the same period that the subsequent algorithm is commonly solved over for each iteration. The final column in Table 2.3 shows the maximum mean error for any section. This error is much less than 1° or 1.1% of the mean signal amplitude in a highly dynamic situation and verifies that the inverted pendulum model does capture the main dynamics for this situation. Explanations for the remaining model error include:

- Missing dynamics due to finite encoder precision;
- Errors in the initial set up, placement and alignment of the accelerometer, and zero position of the pendulum;
- Out of plane disturbances affecting the accelerometers.

2.4 Summary

An inverted pendulum model for head motion has been developed. This model is defined by two equations that balance accelerations tangentially, Equation (2.1), and radially, Equation (2.2). Consequently this model is free from unknown forces or

inertial metrics. The model equations developed are experimentally verified using an inverted pendulum apparatus, with an optical encoder providing the “true” measure of rotation. The model presented is limited to one degree of rotational freedom. However, provides a starting point to prove the concept of model based head tracking using accelerometers.

Chapter 3

Difficulties in Solving the Model Equations

A simple model for head motion, based on an inverted pendulum with a fixed centre of rotation, was presented in Figure 2.1 of Chapter 2. The model Equations (2.1) and (2.2) describing the angular motion were validated experimentally, as seen in Figure (2.11). For easy reference within this chapter these model equations are repeated in Table 3.1.

Table 3.1: The model equations

$$A_T = (R/g)\ddot{\theta} - \sin(\theta) \quad (2.1)$$

$$A_R = (R/g)\dot{\theta}^2 - \cos(\theta) \quad (2.2)$$

However, finding a stable solution to either Equation (2.1) or (2.2) proved difficult. This chapter will show that a conventional engineering approach fails to produce a stable solution. The reasons for this unstable solution are investigated through a linear representation of Equation (2.1). This simplification allows an analytical solution that approximates the solution to Equation (2.1) to be formed. This analytical solution illustrates the specific reasons for the instability.

A Fourier series based approach is also applied as an initial attempt to stabilise the solution. The method uses the assumption that the same frequencies that occur within the acceleration signal, will also occur within the unknown θ signal. This approach is implemented to solve Equation (2.1) and shows improved results. However, significant errors still remain, further demonstrating the challenge in stabilising the solution to Equation (2.1) to obtain a suitable model-based head tracking method.

3.1 A General Engineering Approach

To provide a solution for θ the tangential Equation (2.1) is initially considered. This choice is made because A_T has a higher sensitivity to θ when the accelerometer is placed directly above the centre of rotation. This increased sensitivity results in better quality signal for A_T than A_R , which is confirmed in the model verification of Figure 2.11.

To investigate a solution from the tangential model Equation (2.1) a synthetic signal for θ is generated using a simple sine wave. This signal is used to represent the “true” θ , denoted θ_{true} , and is defined:

$$\theta_{true} = a_1 \sin(\omega_1 t) \quad (3.1)$$

where:

$$\begin{aligned} a_1 &= 1/2 \\ \omega_1 &= 5 \end{aligned} \quad (3.2)$$

The signal θ_{true} of Equation (3.1) is substituted into Equation (2.1) to derive a synthetic signal for $A_{T,true}$:

$$A_{T,true} = (R/g)\ddot{\theta}_{true} - \sin(\theta_{true}), \quad (3.3)$$

Taking a general engineering approach and solving Equation (2.1) numerically illustrates the instability present. Equation (2.1), where A_T is given by $A_{T,true}$ of Equations (3.1) – (3.3), was solved in Maple using the default initial value problem (IVP) solver, a Fehlberg fourth-fifth order Runge-Kutta method, and in Matlab using a similar solver. For two sets of initial conditions $\{\theta_0 = 0, \dot{\theta}_0 = 0\}$ and $\{\theta_0 = \theta_{true}(0), \dot{\theta}_0 = \dot{\theta}_{true}(0)\}$, both Maple and Matlab failed to produce a stable solution.

The results for the two cases are presented in Figure 3.1. The solution from the first case with initial conditions $\{\theta_0 = 0, \dot{\theta}_0 = 0\}$, is seen to become unstable immediately. The solution from the second case, with the true initial conditions, performs better. However, the latter solution still only tracks the true solution

of Equation (3.1), for two cycles before diverging, despite the unlikely perfectly true initial conditions. These diverging results can be interpreted as the pendulum spinning in the physical system.

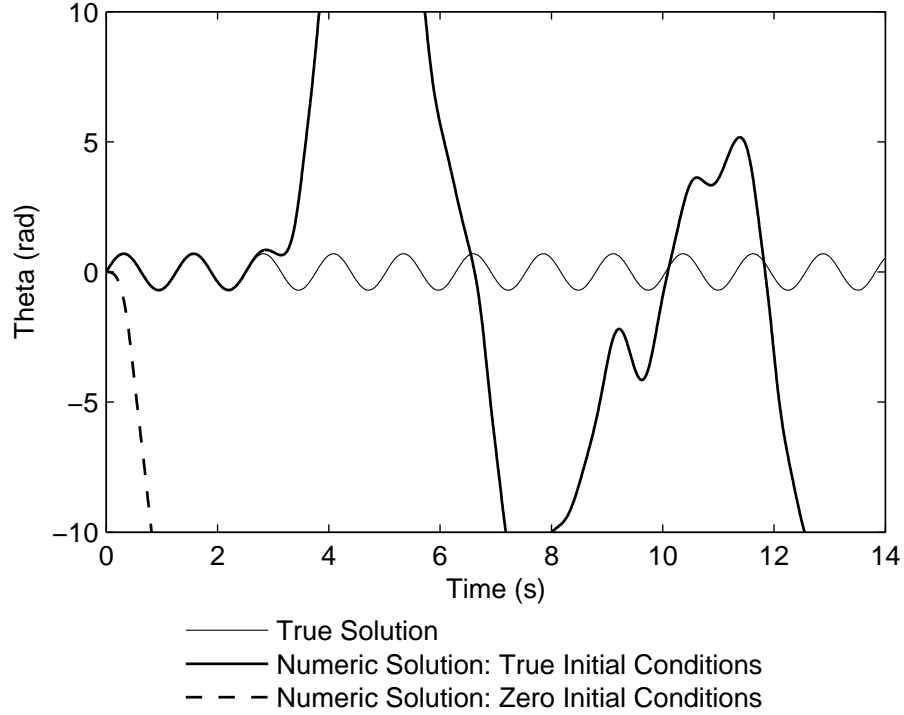


Figure 3.1: Numerical solutions to the tangential ODE given zero and true initial conditions

A further test is done with an amplitude of θ_{true} that is one fifth of the signal amplitude shown in Figure 3.1. The parameters a_1 and ω_1 in Equation (3.1) are thus defined:

$$\begin{aligned} a_1 &= 1/10 \\ \omega_1 &= 5 \end{aligned} \tag{3.4}$$

Substituting the new θ_{true} , defined by Equations (3.1) and (3.4) into Equation (3.3) provides the corresponding signal for $A_{T,true}$.

Solving Equation (2.1), again numerically, with the true initial conditions $\{\theta_0 = \theta_{true}(0), \dot{\theta}_0 = \dot{\theta}_{true}(0)\}$ and A_T defined by the new $A_{T,true}$ of Equations, (3.1), (3.3) and (3.4), illustrates some partial stability within the solution. This quasi-stability is illustrated in Figure 3.2, where the solution oscillates around π although similar oscillations have been observed at $-\pi$ depending on the initial conditions chosen.

The oscillatory solution in Figure 3.2 corresponds to the stable position of a physical pendulum, where the pendulum hangs directly below the axis of rotation. Numerical solutions with many different starting points have shown that including a damping term, $b\dot{\theta}$ in the ODE of Equation (2.1) can stabilise this solution. However, adding damping proves to be of no practical use in determining the true orientation θ , and therefore the results are not shown.

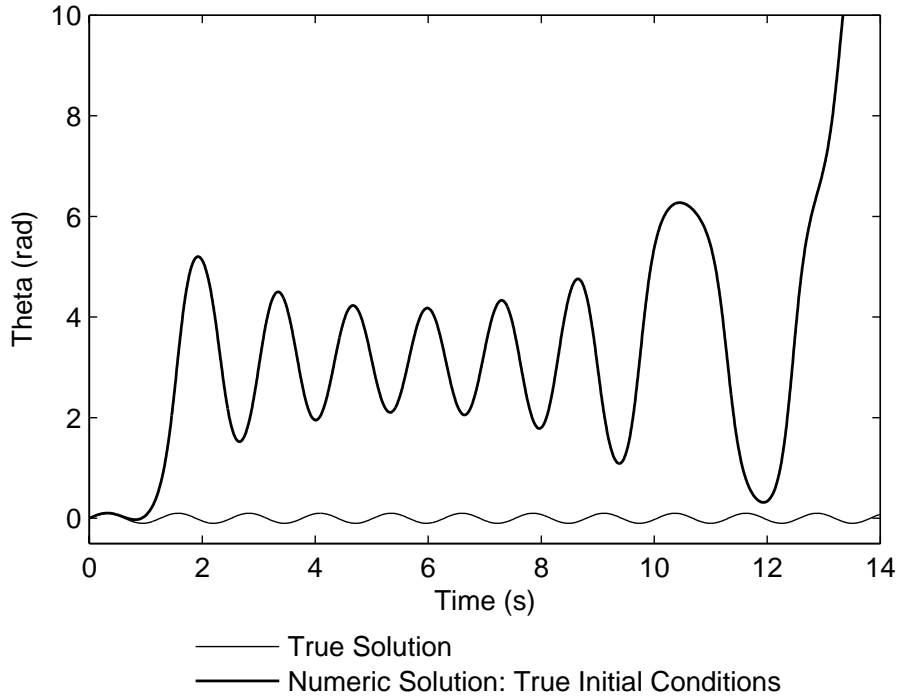


Figure 3.2: Numerical solution to the tangential ODE showing quasi-stability present with small amplitude and true initial conditions

Due to the stiff nature of Equation (2.1) an implicit method, `ode15s` in Matlab, was implemented in an attempt to increase the numerical stability of the method. However, this method also fails, producing unstable results similar to those shown in Figure 3.1.

Attempts to directly solve Equation (2.2) have been investigated by replacing Equation (2.2) with the equations:

$$\dot{\theta}_0 = +\sqrt{g/R(A_R + \cos(\theta))}, \quad \dot{\theta} > 0 \quad (3.5)$$

$$= -\sqrt{g/R(A_R + \cos(\theta))}, \quad \dot{\theta} < 0 \quad (3.6)$$

But the poor quality of the radial acceleration signal due to noise and a relatively low signal, and the difficulty in handling the sign changes in Equations (3.5) and

(3.6) gave unstable results. There is also no immediate, direct way of solving both Equations (2.1) and (2.2) simultaneously.

3.2 The Linear System

To investigate the cause of the instability in the solution, shown in Figures 3.1 and 3.2, Equation (2.1) is linearised:

$$A_T = (R/g)\ddot{\theta} - \theta \quad (3.7)$$

Equation (3.7) has an analytical solution of the form:

$$\theta = \theta_c + \theta_p \quad (3.8)$$

$$\theta_c = C_2 e^{\frac{\sqrt{g}}{\sqrt{R}} t} + C_1 e^{-\frac{\sqrt{g}}{\sqrt{R}} t} \quad (3.9)$$

where θ_c denotes the complimentary solution, C_1 and C_2 are arbitrary constants, and θ_p is a particular solution to Equation (3.7).

The positive power in the C_2 exponential term fully explains the instability observed in the solutions of Figures 3.1 and 3.2. Typically, the transient solution corresponding to Equation (3.9) would die away leaving the steady state solution θ_p . However, the positive power of this exponential term results in an increasing transient solution, which after only a short period of time completely dominates the full solution.

Due to the large numerical value of the positive power exponential, the coefficient, C_2 in Equation (3.9), must be found very precisely to determine an accurate solution θ in Equation (3.8). Given the initial conditions determine C_2 , any small error in the initial conditions will be transferred to C_2 , and be greatly magnified in the result. Thus, the solution of Equation (3.8) to the linear Equation (3.7) is extremely sensitive to the initial conditions used, and hence is inherently ill-conditioned given noisy measurements and uncertainty in any initial conditions for practical cases.

To illustrate this ill-conditioning for the linear Equation (3.7), consider a synthetic acceleration signal $A_{T,true,lin}$ generated from θ_{true} , in Equations (3.1) and (3.2),

as follows:

$$A_{T,true,lin} = (R/g)\ddot{\theta}_{true} - \theta_{true} \quad (3.10)$$

Solving Equation (3.7) with A_T determined from Equation (3.10), and using the true initial conditions $\{\theta_0 = \theta_{true}(0), \dot{\theta}_0 = \dot{\theta}_{true}(0)\}$ provides a stable solution for all time. However, introducing a small error ϵ to the $\dot{\theta}_0$ initial condition makes the solution unstable. For example, Figure 3.3 illustrates this ill conditioning when the error $\epsilon = 1e^{-18}$, effectively machine zero or smaller computationally.

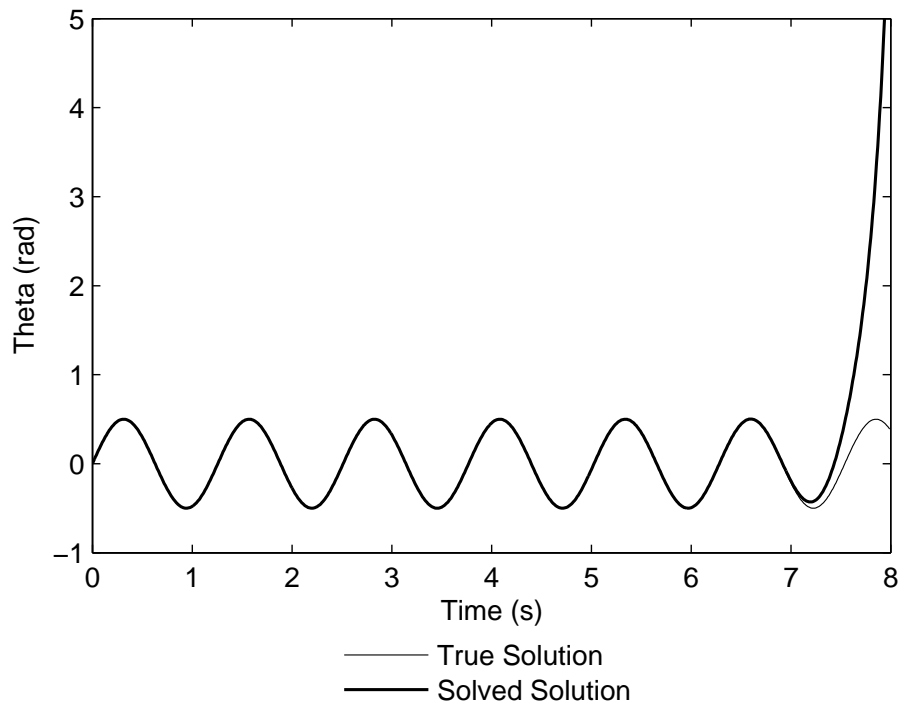


Figure 3.3: Simulated linearised data, solved analytically using initial conditions with a small additive error $\epsilon = 1e^{-18}$ applied to the true $\dot{\theta}_0$ initial condition

3.3 A Frequency Based Solution

The numerical methods applied in the general engineering approach failed to produce a stable solution to Equation (2.1), as seen in Figures 3.1 and 3.2. The failure of this conventional approach means that a new method is required to solve Equation (2.1) and provide a stable solution for θ . Thus, a unique frequency based method is developed, and tested in this section.

3.3.1 Method

The solution method presented, is based on the assumption that the frequencies within an acceleration signal are generated by pure rotation, as is the case for the model of Figure 2.1, and will also be present in rotation signal θ . This assumption is utilised in the method constructed as follows.

Consider the following generic expression for θ denoted θ_{sol} , that is constructed from sine and cosine curves:

$$\theta_{sol} = \sum_{i=0}^j (a_i \sin(\omega_i t) + b_i \cos(\omega_i t)) \quad (3.11)$$

where a_i and b_i are unknown constants, ω_i denotes a rotational frequency present in the signals, and j denotes the number of frequencies used to describe the signal over a period ΔT .

Since A_T is directly measured, the rotational frequencies ω_i can be found using the Fast Fourier Transform (FFT). This step may be avoided if typical head motion can be described by a small set of ω_i frequency terms. However, for this initial testing the 10 largest frequencies, including the zero frequency, are selected by computing the FFT over the selected signal period ΔT .

Substituting θ_{sol} from Equation (3.11), with known values of $\{\omega_i, i = 0, \dots, j\}$, into the linear Equation (4.5), gives an expression for A_T denoted $A_{T,fit}$:

$$A_{T,fit} = \sum_{i=0}^j (a_i \bar{A}_i(t) + b_i \bar{B}_i(t)) \quad (3.12)$$

where $\bar{A}_i(t)$ and $\bar{B}_i(t)$ are functions of time defined in terms of ω_i :

$$\bar{A}_i(t) = (-\sin(\omega_i t) - R/g \sin(\omega_i t) \omega_i^2) \quad (3.13)$$

$$\bar{B}_i(t) = (-\cos(\omega_i t) - R/g \cos(\omega_i t) \omega_i^2) \quad i = 0, \dots, j \quad (3.14)$$

Setting $A_{T,fit}$ in Equation (3.12) equal to the measured data $\{A_T(t_k), k = 0, \dots, N\}$

yields the following matrix system:

$$\begin{bmatrix} \bar{A}_0(t_0), & \bar{B}_0(t_0) & \cdots & \bar{A}_j(t_0) & \bar{B}_j(t_0) \\ \bar{A}_0(t_1), & \bar{B}_0(t_1) & \cdots & \bar{A}_j(t_1) & \bar{B}_j(t_1) \\ \vdots & \vdots & & \vdots & \vdots \\ \bar{A}_0(t_N), & \bar{B}_0(t_N) & \cdots & \bar{A}_j(t_N) & \bar{B}_j(t_N) \end{bmatrix} \begin{bmatrix} a_0 \\ b_0 \\ \vdots \\ a_j \\ b_j \end{bmatrix} = \begin{bmatrix} A_T(t_0) \\ A_T(t_1) \\ \vdots \\ A_T(t_N) \end{bmatrix} \quad (3.15)$$

where N denotes the number of sample time steps within the signal of length ΔT , and the parameters t_0 , t_1 , and t_N denote individual time points.

The system in Equation (3.15) can be solved using a linear least squares method to uniquely determine the constants $\{a_i, b_i, i = 0, \dots, j\}$. Substituting the optimal values of these coefficients into Equation (3.11), provides the solution for θ over the whole period ΔT . The method is summarised in the flow-chart in Figure 3.4.

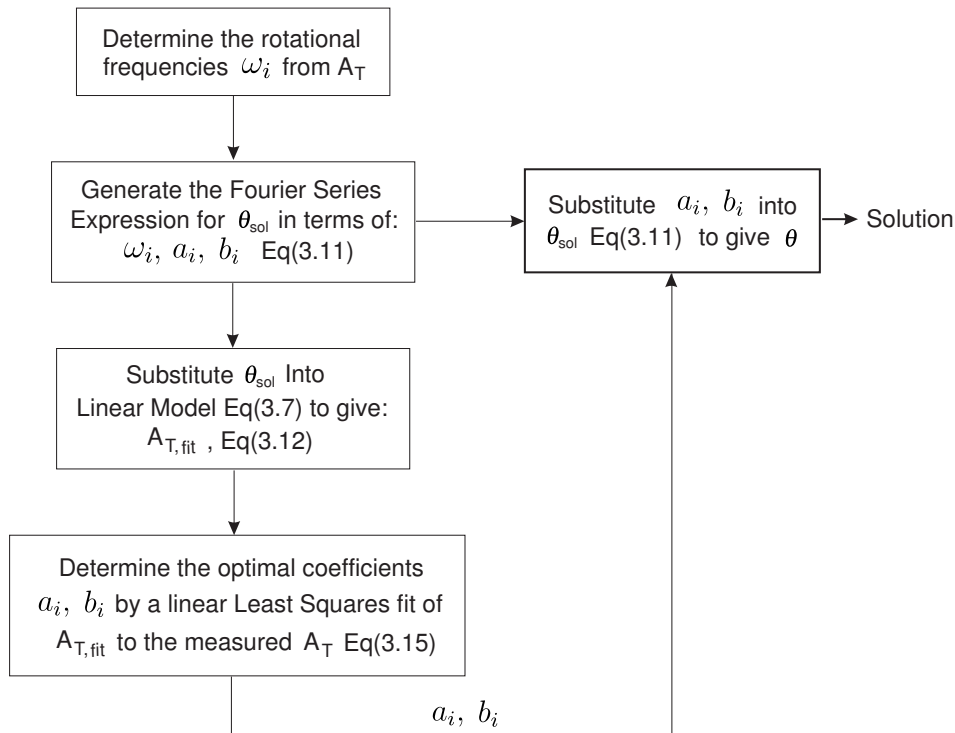


Figure 3.4: Flow-chart summarising the Fourier Series based method of solving orientation.

3.3.2 Results and Discussion

The frequency method of Figure 3.4 is evaluated using signals collected experimentally from the inverted pendulum of Figures 2.9 and 2.10. Two experiments were conducted to test the method at different frequency motions. First, a slower motion is investigated. The signal frequencies of the A_T from the accelerometer and the measured θ from the encoder denoted θ_{en} are analysed and compared. Figure 3.5 shows the frequency components of each signal for the same motion over a 10 second period generated by using a FFT.

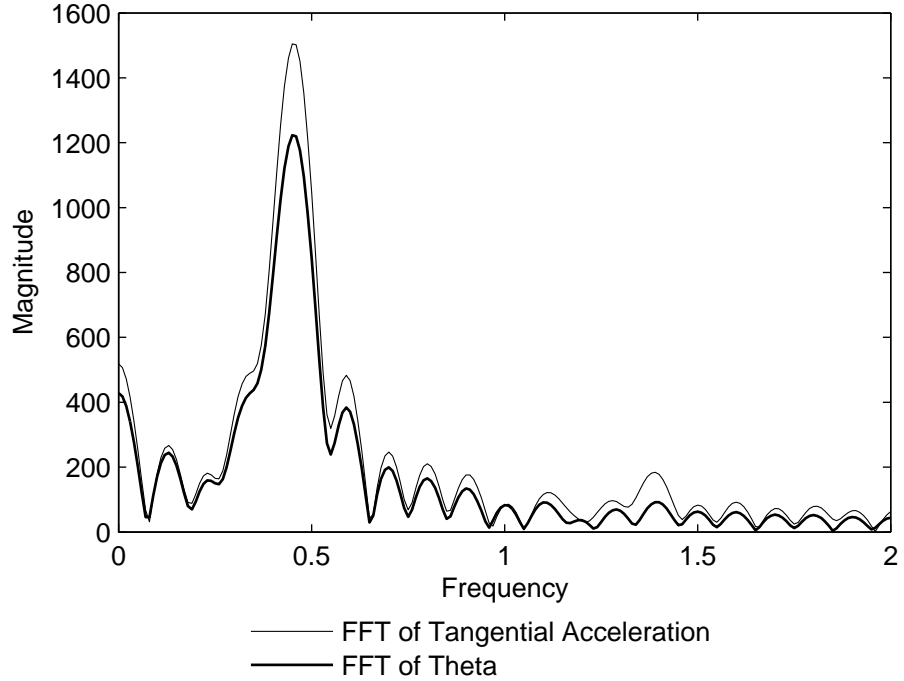


Figure 3.5: The FFT for both the measured A_T and measured θ_{en} from the optical encoder.

The results in Figure 3.5 show a good comparison in terms of the frequencies represented within each signal. This result validates the underlying assumption upon which this method is based. More specifically, Figure 3.5 shows that for the physical inverted pendulum, acceleration and rotational signals do contain the same frequency components, and are similar to what would be found in the intended application space.

Figure 3.6 shows the results of the frequency method of Figure 3.4 for the first case of slow motion. Figure 3.6 (A) shows the quality of the fit of the $A_{T,fit}$ expression of Equation (3.12) to the measured A_T in Equation (3.15). Figure 3.6 (B)

shows the resulting comparison to the true solution measured by the encoder, after substituting the optimised variables $\{a_i, b_i, i = 0..j\}$ into θ_{sol} of Equation (3.11). Similar results are shown for the case of higher frequency motion in Figure 3.7.

The fits achieved in Figures 3.6 and 3.7 show a stable solution is found for θ . The accuracy of the θ solution obtained by the method shows a good correlation with the fit achieved to the corresponding A_T signal over the same section. Although poor results are typically achieved at the end of the signal. The value at t_N would correspond to the next unknown value for θ in a recursive approach applied for a longer real time signal. The large error at this point would result in a poor estimate of the true signal.

By including more ω_i frequency terms in Equation (3.11) the results of Figures 3.6 and 3.7 can be improved. However, including more frequency terms in Equation (3.11) increases the computation needed. In addition, a large number of frequency terms in the method can result in instability, especially when shorter signals are considered. This instability is explained due to insufficient information being available to accurately determine the coefficients in Equation (3.15) for a large number of terms. Frequency terms in Equation (3.11) that are close to each other can effectively trade off with each other, whether or not the frequency actually exists in the measured A_T signal. For example, if the frequencies within the terms are close and the signal is short, a large value for the a_1 coefficient, in Equation (3.15), may be countered with a large a_2 coefficient of the opposite sign. These competing terms would result in a false representation of the magnitudes of the various frequencies, leading to instability in the overall solution.

To limit the number of ω_i terms, the basic method presented in Figure 3.4 was extended to allow optimal ω_i values, within a preset bound around the measured frequencies in Figure 3.5. In other words, some freedom was allowed in the frequencies to provide a good fit to the measured A_T signal, without requiring a large number of predefined frequencies. The essential idea was to have an objective function with the frequencies as the only inputs. For each fixed set of frequencies the method of Figure (3.4) is applied to find the best coefficients $\{a_i, b_i, i = 0..j\}$. The resulting least squares error is then computed between $A_{T,fit}$ of Equation (3.12) and the measured A_T . The set of frequencies that minimise the least squares error can be determined by a standard non-linear optimisation. However, this extended new method improved the fit to A_T with fewer frequencies, it did not improve the result

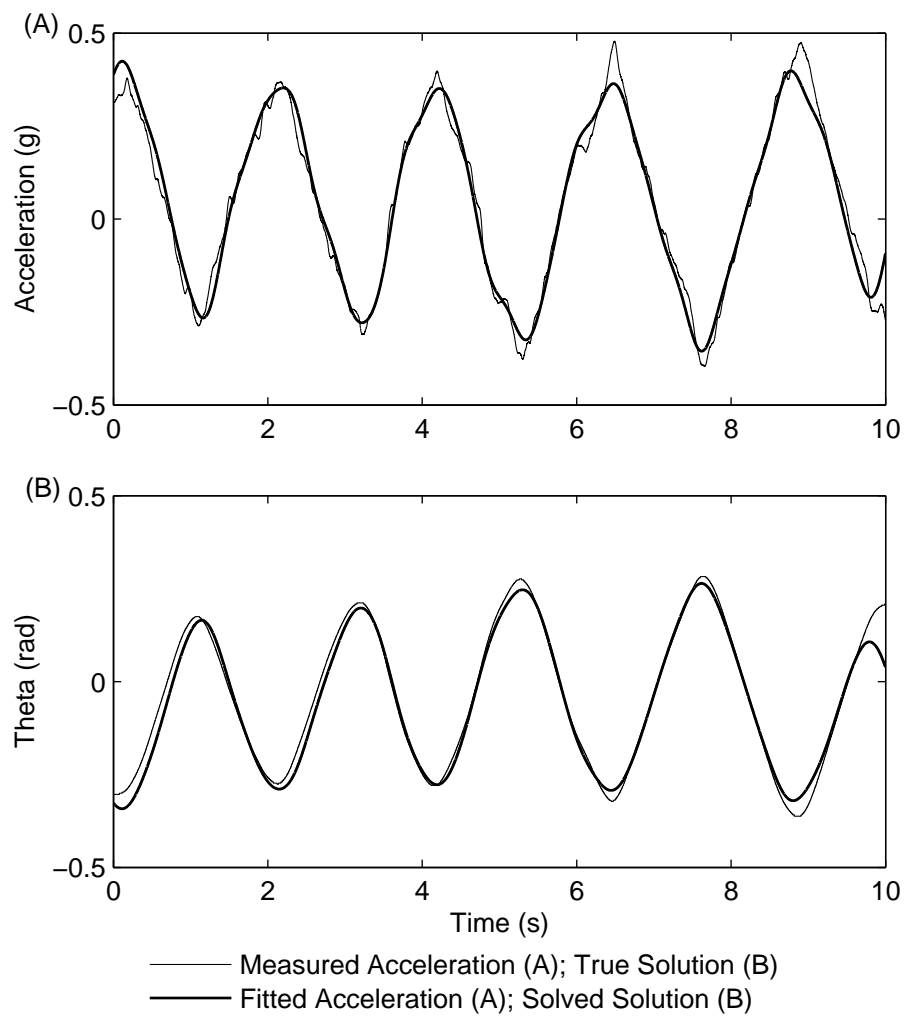


Figure 3.6: Acceleration fit and solution for slow motion using the frequency based method

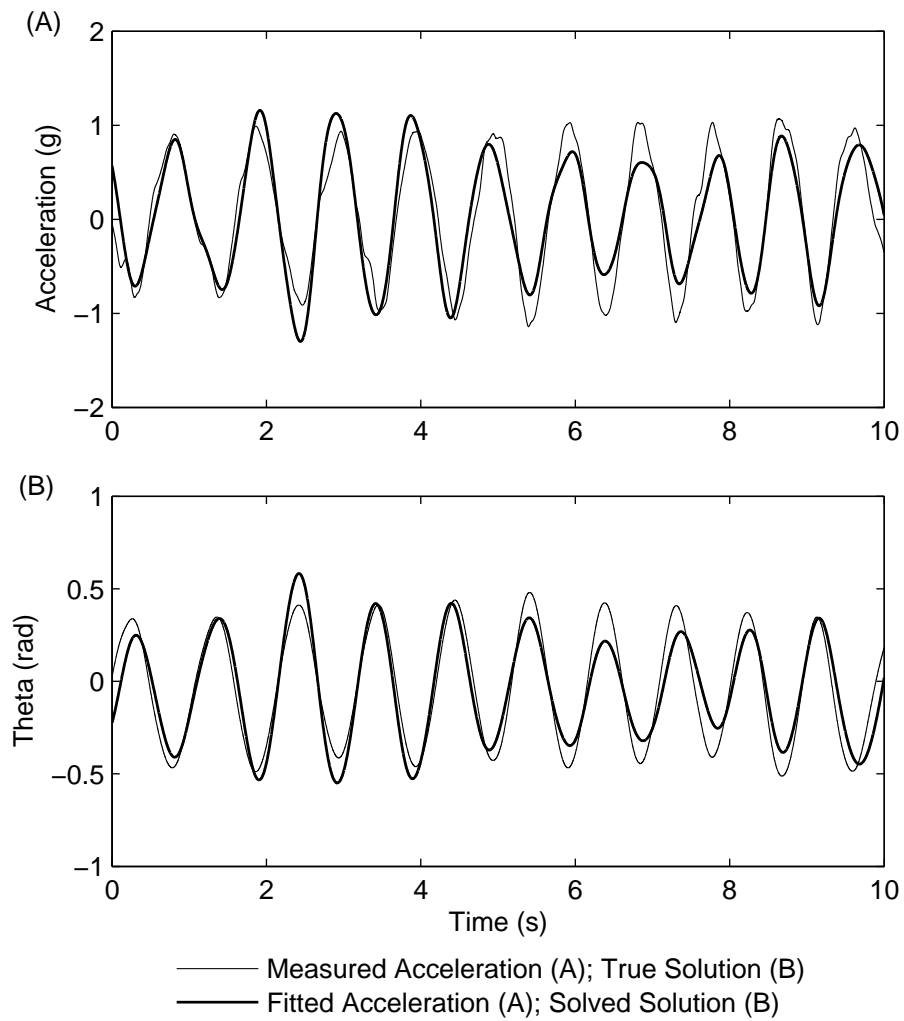


Figure 3.7: Acceleration fit and solution for higher frequency motion using the frequency based method

for θ compared to Figures 3.6 and 3.7, therefore the details of this method and results are not shown.

The reason that these frequency based approaches fail is that only one Equation (2.1) is used to find θ . As shown in Equation (3.8) there are in fact infinitely many solutions, θ , that satisfy Equation (3.7) by choosing different C_1 and C_2 constants. Forcing the solution to be of the form Equation (3.11), in principle would seem to avoid the exponential terms in Equation (3.9) from entering the solution to θ . The problem is that a low frequency sine wave could easily resemble the positive exponential term in Equation (3.9) for a small C_2 and restricted time interval. Therefore, there is no constraint on Equation (3.11) that can completely avoid some contribution from the C_2 in Equation (3.9) and thus the final solution for θ is corrupted and significant errors result, as shown in Figures 3.6 and 3.7.

3.4 Summary

Solving the model Equations (2.1) and (2.2) to provide a solution for the orientation of the pendulum proves a very difficult and challenging problem in creating a model based sensor for head tracking using only acceleration measurements. Applying a general engineering approach, and solving the equations numerically produces unstable results, as illustrated in Figures 3.1 and 3.2. Linearising Equation (2.1) allows an analytical solution to be formed. This analytical solution shows that the transient part of the solution becomes unstable due to the presence of a positive exponential power. Thus, the coefficient of the term containing this positive exponential power must be very precisely known to provide a stable overall solution. Therefore, the solution is ill-conditioned and is extremely sensitive to the initial conditions, and thus measurement noise and other errors.

There is a unique solution to Equations (2.1) and (2.2) corresponding to the true signal over the period considered. However, any explicit or implicit numerical method that relies on initial conditions to start it off must start at precisely the correct point otherwise the solution will move on an unstable transient of Equation (2.1).

The difficulty of determining a solution, θ , to the inverted pendulum model Equations (2.1) and (2.2) is supported in the literature by the fact that no stable

solution over any reasonable length of time is presented. As discussed in Section 1.3.1, Gillies et al. [2003] do solve the tangential equation. However, their solution is unstable over time, and they declare that it is of no use after a relatively very short 0.1 seconds.

A method based on a Fourier series was developed and presented in Figure 3.4. This method can produce stable results, as shown in Figures 3.6 and 3.7. However, the method is restricted by the signal motion, selected frequencies, and the length of signal solved over. Specifically this method fails to produce the required solution, only providing one possible solution to Equation (3.7) that contains transient terms from Equation (3.9). As a result, while the method can track a “true” solution, it is not fully accurate. Hence, an improved approach, beyond this novel frequency approach, is required to create the accelerometer model-based sensor for head tracking or similar applications.

Chapter 4

Initial Model Implementation

Finding a solution to Equation (2.1) is a challenging problem, with the conventional approach of Figures 3.1 and 3.2 being unstable and other initial approaches shown in Figures 3.6 and 3.7 producing stable, but inaccurate, results. The instability and ill conditioning observed in the numerical solutions to Equation (2.1) and the linearised model Equation (3.7), shown in Figures 3.1 – 3.3, is caused by the presence of a positive exponential power in the transient portion of the solution.

Within this chapter a unique mathematical approach is developed based on writing the analytical solution to the linearised model of Equation (2.1) in terms of arbitrary constants C_1 and C_2 and assuming the initial conditions are unknown. The independent radial Equation (2.2) is then utilised to find optimal and precise values for the unknown constants, C_1 and C_2 . Thus, providing an accurate measurement of rotation.

Two methods are developed using different linearised expressions for $\sin(\theta)$ in Equation (2.1). The first method linearises Equation (2.1) over a period of 0.1s [Keir et al., 2007b]. However, the results showed a large standard deviation in the predicted versus the measured angle θ . To improve performance, a piecewise solution method was developed allowing an approximate, but highly accurate, analytical solution to Equation (2.1) over the longer period of 0.3s [Keir et al., 2007a]. These two methods are presented, compared and evaluated using both simulated and experimental data.

4.1 Methods

4.1.1 Single Section

The linearisation, $\sin(\theta) = \theta$, in Equation (3.7) of Section 3.2 is only valid for small angles. It is thus not appropriate for representing the large rotations possible with head motion. This simplification is improved by fitting a more general linear relationship to $\sin(\theta)$ over a range of theta within a short time period.

The $\sin(\theta)$ linearisation is illustrated schematically in Figure 4.1. The parameter θ_{new} in Figure 4.1 (A) corresponds to the time t where θ is unknown, θ_{old} is a previously stored vector of known or identified θ values, and θ_{max} and θ_{min} are the maximum and minimum values of θ_{old} . These values of θ_{max} and θ_{min} define a specific section of the sine curve shown in Figure 4.1 (B). To find the best fit to $\sin(\theta)$ in this section of Figure 4.1 (B), 10 points $\theta_1, \dots, \theta_{10}$, are equally spaced in the interval $[\theta_{min}, \theta_{max}]$.

The linearisation of $\sin(\theta)$ is defined:

$$\sin(\theta) \simeq (b_1 + b_2\theta) \quad (4.1)$$

Substituting $\theta = \theta_i$, where $i = 1, \dots, 10$ into Equation (4.1) gives 10 equations in the unknowns b_1 and b_2 :

$$b_1 + b_2\theta_i = \sin(\theta_i) \quad i = 1, \dots, 10. \quad (4.2)$$

Equation (4.2) can be written as a matrix system:

$$\begin{bmatrix} 1 & \theta_1 \\ 1 & \theta_2 \\ \vdots & \vdots \\ 1 & \theta_{10} \end{bmatrix} \begin{bmatrix} b_1 \\ b_2 \end{bmatrix} = \begin{bmatrix} \sin(\theta_1) \\ \sin(\theta_2) \\ \vdots \\ \sin(\theta_{10}) \end{bmatrix} \quad (4.3)$$

This system can be solved by linear least squares to uniquely determine b_1 and b_2 .

The length of time that the linear representation of $\sin(\theta)$ in Equation (4.1) is valid, is highly dependent on the dynamics of θ . Fast and large rotations will result

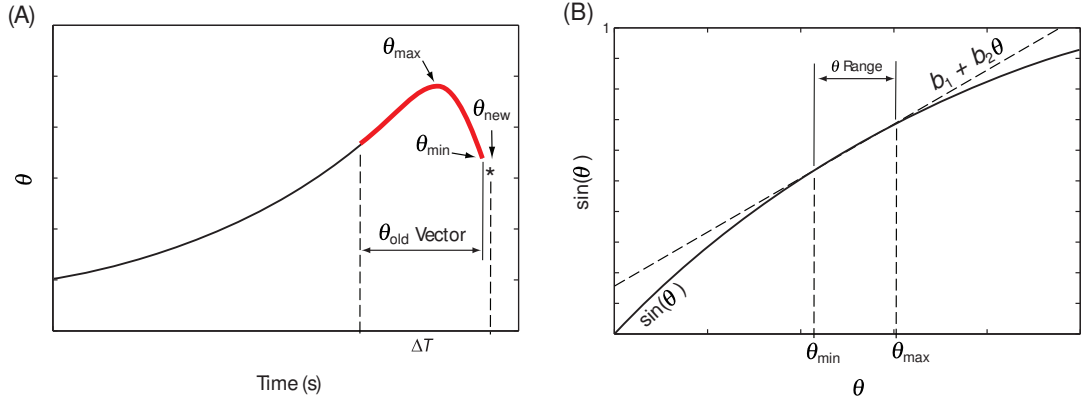


Figure 4.1: Linearisation of $\sin(\theta)$ over a short time period

in a wide range of θ between θ_{max} and θ_{min} and thus require a small period for ΔT in Figure 4.1 (A) to ensure the accuracy of the linearised fit to the sine curve in Figure 4.1 (B). For this method a time period of $\Delta T = 0.1\text{s}$ is used.

To get an idea of the error involved, consider the fast 2Hz head motion with an amplitude of 15° in Figure 4.2 (A). The values of θ_{max} and θ_{min} define the range of θ within $\Delta T = 0.1\text{s}$ as 17.6° at the steepest section of the signal. This signal oscillates about $\pi/2$ thus, the range of θ coincides with a point of maximum curvature for $\sin(\theta)$ in Figure 4.2 (B). Using Equations (4.1) - (4.3) to linearise $\sin(\theta)$ gives $\{b_1 = 0.9952; b_2 = 0\}$. Therefore the maximum error of 0.007 is given for this situation at θ_{max} and θ_{min} , and is representative of the worst case error.

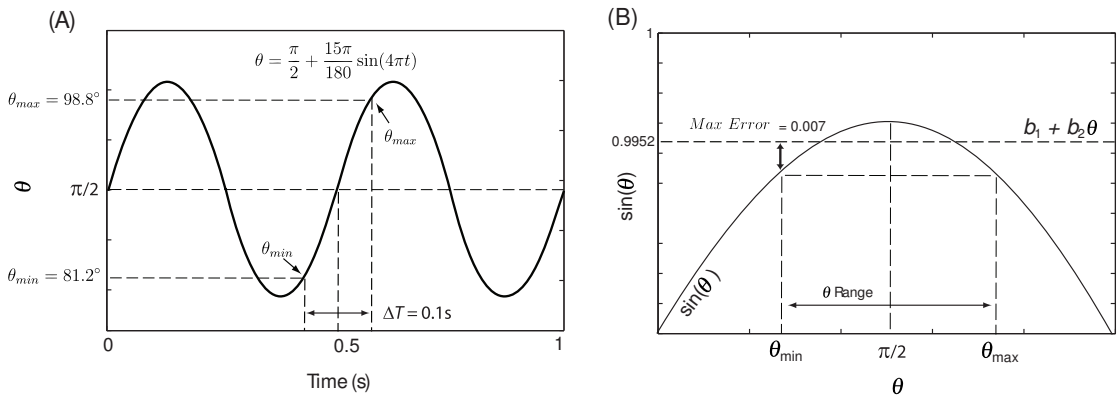


Figure 4.2: Maximum error in the $\sin(\theta)$ linearisation where $\Delta T = 0.1\text{s}$

The analytical solution of Equation (3.8) is incomplete, as the particular solution θ_p , is not given. However, A_T is measured at discrete times. Therefore, fitting a cubic function to A_T over the short time period allows θ_p to be analytically determined. Thus, an analytical solution can be found over the time period of interest.

The cubic functions approximating the measured tangential acceleration, A_T , over the period of $\Delta T = 0.1\text{s}$ are defined:

$$A_{T,fit} = u_1 + u_2t + u_3t^2 + u_4t^3 \quad (4.4)$$

Note that in practice A_T and A_R consist of discrete points, measured at 100Hz in this research. For the given time period of 0.1s the parameters u_1, \dots, u_4 in Equation (4.4) are determined by a linear least squares polynomial fitting algorithm. For example, “polyfit” in Matlab.

Substituting Equations (4.1) and (4.4) into Equation (2.1) gives:

$$(R/g)\ddot{\theta} - (b_1 + b_2\theta) = u_1 + u_2t + u_3t^2 + u_4t^3 \quad (4.5)$$

The analytical solution to Equation (4.5) exists and can be found using Maple and is defined:

$$\theta_{sol} = C_2e^{(mt)} + C_1e^{(-mt)} + f(t) \quad (4.6)$$

where C_1 and C_2 are unknown constants and:

$$m = \frac{\sqrt{(b_2g)}}{\sqrt{R}}$$

$$f(t) = \frac{1}{b_2^2g} \left(-gb_2(b_1 + u_1 + u_2t + u_3t^2 + u_4t^3) - 2R(3u_4t + u_3) \right)$$

The solution, θ_{sol} , in Equation (4.6) is very sensitive to the value of C_2 due to the positive $e^{(mt)}$ term, as demonstrated in Figure 3.3 of Section 3.2. Thus, optimal and precise values of C_1 and C_2 are required to provide an accurate approximation of the solution to the tangential Equation (2.1).

The radial ODE, Equation (2.2), is an independent model for describing θ and thus, provides a means to solve for C_1 and C_2 . However, Equation (2.2) contains a nonlinear cosine term that prevents a simple analytical approach to determining C_1 and C_2 . A quadratic function is therefore fitted to this cosine term in a similar way that the linear function was fitted to the sine term in Equations (4.1) – (4.3). A quadratic function was chosen for increased accuracy and since there would already be a quadratic term due to the presence of the $\dot{\theta}^2$ in Equation (2.2). This

approximation to $\cos(\theta)$ is defined:

$$\cos(\theta) \simeq c_1 + c_2\theta + c_3\theta^2 \quad (4.7)$$

where c_1 , c_2 , and c_3 are evaluated by a linear least squares fit of the quadratic function to $\cos(\theta)$ over the range of θ within time period, using the method in Equation (4.3). Substituting in $\cos(\theta)$ from Equation (4.7), and θ_{sol} from Equation (4.6) into Equation (2.2) provides an expression for A_R in terms of C_1 and C_2 , defined:

$$\begin{aligned} A_{R,sol} &= (R/g)\dot{\theta}_{sol}^2 - (c_1 + c_2\theta_{sol} + c_3\theta_{sol}^2) \\ &= \frac{R}{g}(C_2me^{(mt)} - C_1me^{(-mt)} + \dot{f}(t))^2 - \\ &\quad c_3(C_2e^{(mt)} + C_1e^{(-mt)} + f(t))^2 - \\ &\quad c_2(C_2e^{(mt)} + C_1e^{(-mt)} + f(t)) - c_1 \end{aligned} \quad (4.8)$$

where all terms have been defined previously.

The optimal values of C_1 and C_2 in Equation (4.6) could be defined theoretically as the best least squares fit to the actual θ values. But in practice for the application considered in this thesis, the measured θ is not available to constrain C_1 and C_2 in the considered time interval. However, since $A_{R,sol}$ in Equation (4.8) is directly derived from θ_{sol} in Equation 4.6, and the measured A_R is directly determined from the physical θ dynamics, Equations (4.6) and (4.8) are theoretically equivalent. In other words, the optimal C_1 and C_2 that best fit θ_{sol} in Equation 4.6 to the measured θ also correspond to the optimal C_1 and C_2 that best fit $A_{R,sol}$ in Equation (4.8) to the measured A_R . Note that in practice noise may prevent these optimal values of C_1 and C_2 from perfectly coinciding.

The ‘‘best fit’’ of $A_{R,sol}$ in Equation (4.8) to the measured radial acceleration A_R is defined in a least squares sense over the short time period of $\Delta T = 0.1s$, as follows. First, consider the following objective function:

$$\Omega(C_1, C_2) = \sum_{i=0}^k \left(A_{R,sol}(t_k - i\Delta t) - A_R(t_k - i\Delta t) \right)^2 \quad (4.9)$$

where k is the number of data points in the fitted period prior to the current time point, $t = t_k$, and Δt is the fixed time interval between the points. Note that,

$\Delta T = 0.1\text{s}$ and $\Delta t = 0.01\text{s}$ corresponding to a measurement frequency of 100Hz and $k = 10$. The minimum value of the surface $\Omega(C_1, C_2)$ in Equation (4.9) provides the optimal value of the unknown constants C_1 and C_2 , and occurs where the gradient of Ω with respect to C_1 and C_2 is 0.

Setting the gradient $\nabla_{C_1, C_2} \Omega = 0$ results in two equations:

$$\frac{\partial}{\partial C_1} \left(\sum_{i=0}^k \left(A_{R,sol}(t_k - i\Delta t) - A_R(t_k - i\Delta t) \right)^2 \right) = 0 \quad (4.10)$$

$$\frac{\partial}{\partial C_2} \left(\sum_{i=0}^k \left(A_{R,sol}(t_k - i\Delta t) - A_R(t_k - i\Delta t) \right)^2 \right) = 0 \quad (4.11)$$

Equations (4.10) and (4.11) are a coupled set of multivariate polynomials. After computation in Maple, Equation (4.10) is order 4 in the variable C_1 and order 3 in the variable C_2 , and Equation (4.11) the opposite, order 4 in the variable C_2 , and order 3 in the variable C_1 . Solving Equations (4.10) and (4.11) in Maple thus yields nine different pairs of solutions including complex solutions. These solutions are denoted as $\{C_1^{(i)}, C_2^{(i)}, i = 1, \dots, 9\}$.

The correct solution corresponding to the global minima is defined:

$$\{C_1^{(j)}, C_2^{(j)}\} = \{C_{1,true}, C_{2,true}\} \quad (4.12)$$

where $C_1^{(j)} \in \mathbb{R}$, $C_2^{(j)} \in \mathbb{R}$ and

$$\Omega(C_1^{(j)}, C_2^{(j)}) = \min_{i \in \{1, \dots, 9\}} (\Omega(C_1^{(i)}, C_2^{(i)})) \quad (4.13)$$

In essence, the optimal solution is the pair $\{C_1^{(j)}, C_2^{(j)}\}$ that is real valued and has minimal Ω .

The optimal C_1 and C_2 of Equation (4.12) are substituted into Equation (4.6) to obtain θ_{sol} throughout the current time interval ΔT and thus find θ and the head orientation at the current time t_k . The parameter θ_{old} is then updated to include θ_{sol} at time t_k and the overall process is repeated for the next time step and solution. Figure 4.3 summarises this method in a flow-chart.

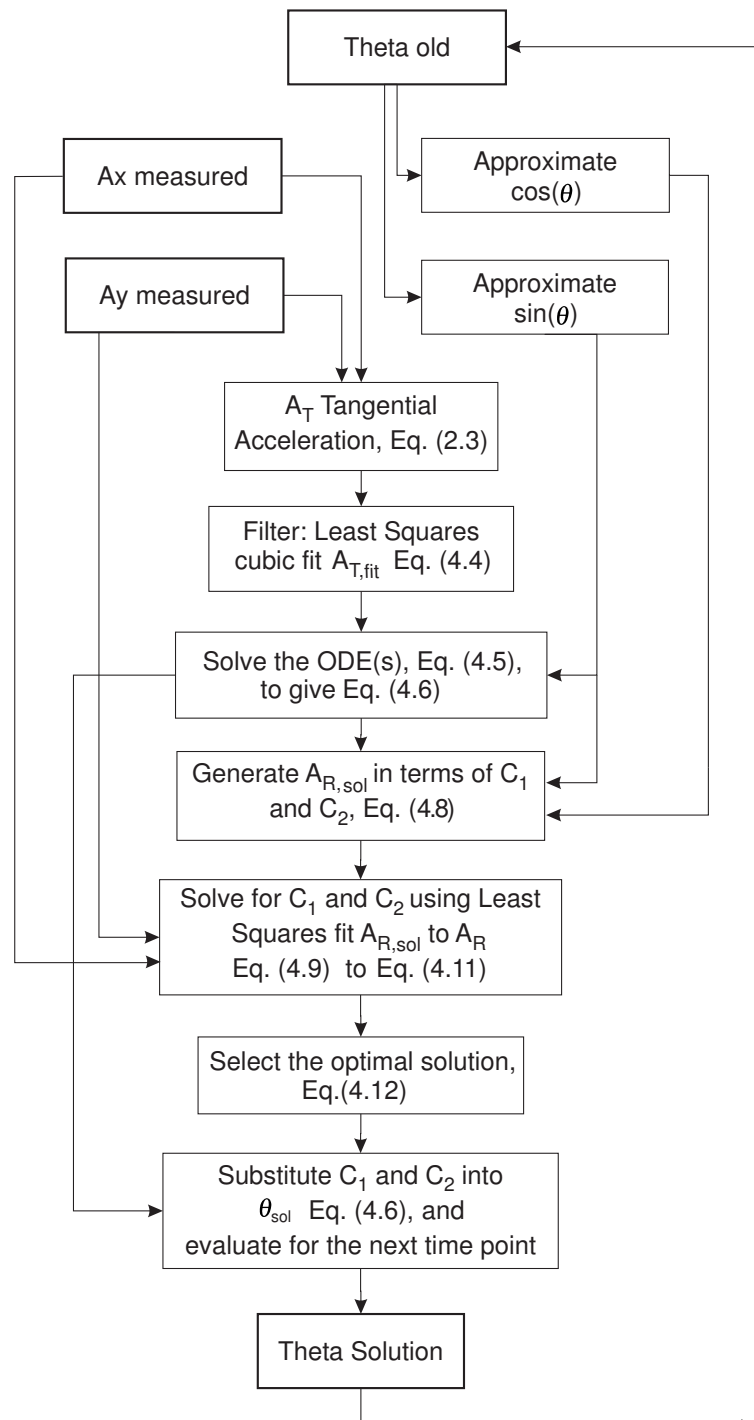


Figure 4.3: Flow-chart for the solution of θ

4.1.2 Multiple Piecewise Sections

The single section method of Equations (4.1) to (4.13) restricts the time interval ΔT in Figure 4.1 (A) to a sufficiently small length where the $\sin(\theta)$ linearisation in Equation (4.1) remains accurate. A small time interval ΔT corresponds to a small time period of dynamic motion, which given noisy signals allows a lot of freedom for the solution to move. As a result it provides less constraint on the optimal C_1 and C_2 . Extending the length of ΔT in Figure 4.1 (A) should provide more robustness against noise. A linear piecewise function for $\sin(\theta)$ would eliminate or ameliorate this restriction of the single section method.

To enable an increase in ΔT , while still maintaining the quality of the $\sin(\theta)$ linearisation, a piecewise linear approximation is given. A simple analytical solution is then developed across this approximation, using one C_1 and C_2 rather than a separate C_1 and C_2 for each small time interval of $\Delta T = 0.1\text{s}$ as in the process shown in Figure 4.3.

The piecewise linearisation of $\sin(\theta)$ is extended from Figure 4.1 and is shown in Figure 4.4. Figure 4.4 (A) plots the past values of theta against time with θ_{new} , denoted by an “*”, representing the unknown θ at the current time step. A longer period of $\Delta T = 0.3\text{s}$ is divided into three equal sections of length $\delta T = 0.1\text{s}$. The range of θ within each section is shown in Figure 4.4 (B). The best linear approximation to $\sin(\theta)$ over each period in Figure 4.4 (B) is found using an approach similar to Equations (4.1) – (4.3). The method is described in detail for these three sections, but can be easily extended to a higher number, with the trade off that the simple cubic function may not be valid over longer periods of ΔT , especially at higher frequencies.

With $\delta T = 0.1\text{s}$ in Figure 4.4 the piecewise approximation to $\sin(\theta)$ is defined:

$$\sin(\theta(t)) \simeq b_{1,i} + b_{2,i}\theta \quad 0.1(i-1) \leq t \leq 0.1i, \quad i = 1, \dots, 3 \quad (4.14)$$

where $b_{1,i}$ and $b_{2,i}$ are found by solving Equation (4.3) over the i th section for $i = 1, \dots, 3$. A least squares cubic $A_{T,fit}$ defined by Equation (4.4) is now fitted over $\Delta T = 0.3\text{s}$. Substituting Equation (4.14) and the extended least squares cubic, $A_{T,fit}$ for A_T into Equation (2.1) yields a set of three differential equations describing

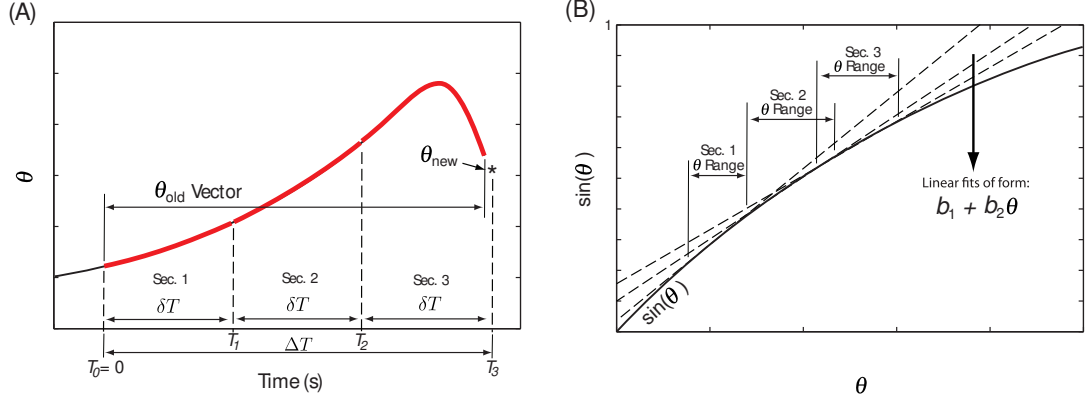


Figure 4.4: A piecewise linearisation of $\sin(\theta)$ allows the model to be fitted to a longer period

the motion:

$$(R/g)\ddot{\theta} - (b_{1,1} + b_{2,1}\theta) = A_{T,fit} \quad 0.0 \leq t \leq 0.1 \quad (4.15)$$

$$(R/g)\ddot{\theta} - (b_{1,2} + b_{2,2}\theta) = A_{T,fit} \quad 0.1 < t \leq 0.2 \quad (4.16)$$

$$(R/g)\ddot{\theta} - (b_{1,3} + b_{2,3}\theta) = A_{T,fit} \quad 0.2 < t \leq 0.3 \quad (4.17)$$

An analytical solution to θ in the set of Equations (4.15) - (4.17) can be found by solving the first ODE analytically, then using the end point value of the resulting solution as the initial condition for the second ODE, and so on up to the third ODE.

The solution $\theta_{sol,1}$ to the first interval is given by Equation (4.6) with b_1 and b_2 replaced by $b_{1,1}$ and $b_{2,1}$ in Equation (4.15). However, the second and third solutions $\theta_{sol,2}$ and $\theta_{sol,3}$ to Equations (4.16) and (4.17) are more difficult to write simply. With the aid of Maple the general solution is constructed as follows:

$$\begin{aligned} \theta_{sol,i} = & (\bar{A}_{1,i}C_1 + \bar{A}_{2,i}C_2 + \bar{A}_{3,i})\mathbf{e}^{m_i(t-T_{i-1})} + \\ & (\bar{B}_{1,i}C_1 + \bar{B}_{2,i}C_2 + \bar{B}_{3,i})\mathbf{e}^{-m_i(t-T_{i-1})} - \\ & \frac{1}{b_{2,i}^2 g} (b_{2,i}g(b_{1,i} + u_1 + u_2t + u_3t^2 + u_4t^3) + 2R(u_3 + 3u_4t)) \end{aligned} \quad (4.18)$$

which has a differential of:

$$\begin{aligned} \dot{\theta}_{sol,i} = & m_i(\bar{A}_{1,i}C_1 + \bar{A}_{2,i}C_2 + \bar{A}_{3,i})\mathbf{e}^{m_i(t-T_{i-1})} - \\ & m_i(\bar{B}_{1,i}C_1 + \bar{B}_{2,i}C_2 + \bar{B}_{3,i})\mathbf{e}^{-m_i(t-T_{i-1})} - \\ & \frac{1}{b_{2,i}^2g}(b_{2,i}g(u_2 + 2u_3t + 3u_4t^2) + 6Ru_4) \end{aligned} \quad (4.19)$$

Note that the differential $\dot{\theta}_{sol,i}$ in Equation (4.19) is required to enable a piecewise definition of all the unknown parameters in Equation (4.18) in terms of the unknown constants C_1 and C_2 . The parameters in Equations (4.18) and (4.19) are defined as follows:

$$\begin{aligned} T_i &= i\delta T \\ m_i &= \frac{(b_{2,i}g)^{1/2}}{R^{1/2}} \\ \bar{A}_{1,i} &= \frac{(b_{2,i}g)^{1/2}q_{1,i} + dq_{1,i}R^{1/2}}{2(b_{2,i}g)^{1/2}} \\ \bar{A}_{2,i} &= \frac{(b_{2,i}g)^{1/2}q_{2,i} + dq_{2,i}R^{1/2}}{2(b_{2,i}g)^{1/2}} \\ \bar{A}_{3,i} &= \frac{1}{2b_{2,i}^{5/2}g^{3/2}} \left((b_{2,i}g)^{3/2}(b_{1,i} + u_1 + u_2T_{i-1} + u_3T_{i-1}^2 + u_4T_{i-1}^3) + u_2(b_{2,i}gR^{1/2}) \right. \\ &\quad \left. + 2u_3((b_{2,i}g)^{1/2}R + b_{2,i}gR^{1/2}T_{i-1}) + 3u_4(+2R^{3/2} + 2(b_{2,i}g)^{1/2}RT_{i-1} + b_{2,i}gR^{1/2}T_{i-1}^2) \right. \\ &\quad \left. + q_{3,i}b_{2,i}^{5/2}g^{3/2} + dq_{3,i}b_{2,i}^2gR^{1/2} \right) \\ \bar{B}_{1,i} &= \frac{(b_{2,i}g)^{1/2}q_{1,i} - dq_{1,i}R^{1/2}}{2(b_{2,i}g)^{1/2}} \\ \bar{B}_{2,i} &= \frac{(b_{2,i}g)^{1/2}q_{2,i} - dq_{2,i}R^{1/2}}{2(b_{2,i}g)^{1/2}} \\ \bar{B}_{3,i} &= \frac{1}{2b_{2,i}^{5/2}g^{3/2}} \left((b_{2,i}g)^{3/2}(b_{1,i} + u_1 + u_2T_{i-1} + u_3T_{i-1}^2 + u_4T_{i-1}^3) - u_2(b_{2,i}gR^{1/2}) \right. \\ &\quad \left. + 2u_3((b_{2,i}g)^{1/2}R - b_{2,i}gR^{1/2}T_{i-1}) + 3u_4(-2R^{3/2} + 2(b_{2,i}g)^{1/2}RT_{i-1} - b_{2,i}gR^{1/2}T_{i-1}^2) \right. \\ &\quad \left. + q_{3,i}b_{2,i}^{5/2}g^{3/2} - dq_{3,i}b_{2,i}^2gR^{1/2} \right) \end{aligned} \quad (4.20)$$

The unknown coefficients $q_{1,i}$, $q_{2,i}$, $q_{3,i}$ and $dq_{1,i}$, $dq_{2,i}$, $dq_{3,i}$ in Equations (4.20) are

formulated such that:

$$\begin{aligned}\theta_{sol,i}(T_{i-1}) &= \theta_{sol,i-1}(T_{i-1}) = q_{1,i}C_1 + q_{2,i}C_2 + q_{3,i} \\ \dot{\theta}_{sol,i}(T_{i-1}) &= \dot{\theta}_{sol,i-1}(T_{i-1}) = dq_{1,i}C_1 + dq_{2,i}C_2 + dq_{3,i} \quad i = 2, 3\end{aligned}\quad (4.21)$$

In other words, $q_{1,i}, \dots, dq_{3,i}$ are the coefficients of C_1 and C_2 for each initial condition of Equations (4.15) – (4.17). For the case where $i = 1$, $q_{1,i}, q_{2,i}, q_{3,i}$ and $dq_{1,i}, dq_{2,i}, dq_{3,i}$ are defined by putting $t = 0$ into Equation (4.18) and (4.19):

$$\begin{aligned}\theta_{sol,1}(0) &= C_1 + C_2 - \frac{1}{b_{2,i}^2 g} (b_{2,i}g(b_{1,i} + u_1) + 2Ru_3) \\ \dot{\theta}_{sol,1}(0) &= -m_i C_1 + m_i C_2 - \frac{1}{b_{2,i}^2 g} (b_{2,i}gu_2 + 6Ru_4)\end{aligned}\quad (4.22)$$

giving:

$$\begin{aligned}q_{1,i} &= 1 & dq_{1,i} &= -m_i \\ q_{2,i} &= 1 & dq_{2,i} &= +m_i \\ q_{3,i} &= -\frac{1}{b_{2,i}^2 g} (b_{2,i}g(b_{1,i} + u_1) + 2Ru_3) & dq_{3,i} &= -\frac{1}{b_{2,i}^2 g} (b_{2,i}gu_2 + 6Ru_4)\end{aligned}\quad i = 1. \quad (4.23)$$

For $i = 2, 3$ the coefficients, $q_{1,i}, q_{2,i}, q_{3,i}$ and $dq_{1,i}, dq_{2,i}, dq_{3,i}$ are defined recursively for computational efficiency and ease of programming, as follows:

$$\begin{aligned}q_{1,i} &= \bar{A}_{1,i-1} \mathbf{e}^{m_{i-1}(T_{i-1}-T_{i-2})} + \bar{B}_{1,i-1} \mathbf{e}^{-m_{i-1}(T_{i-1}-T_{i-2})} \\ q_{2,i} &= \bar{A}_{2,i-1} \mathbf{e}^{m_{i-1}(T_{i-1}-T_{i-2})} + \bar{B}_{2,i-1} \mathbf{e}^{-m_{i-1}(T_{i-1}-T_{i-2})} \\ q_{3,i} &= \bar{A}_{3,i-1} \mathbf{e}^{m_{i-1}(T_{i-1}-T_{i-2})} + \bar{B}_{3,i-1} \mathbf{e}^{-m_{i-1}(T_{i-1}-T_{i-2})} - \\ &\quad \frac{1}{b_{2,i-1}^2 g} (b_{2,i-1}g(b_{1,i-1} + u_1 + u_2 T_{i-1} + u_3 T_{i-1}^2 + u_4 T_{i-1}^3) + 2R(u_3 + 3u_4 T_{i-1})) \\ dq_{1,i} &= m_{i-1} \bar{A}_{1,i-1} \mathbf{e}^{m_{i-1}(T_{i-1}-T_{i-2})} - m_{i-1} \bar{B}_{1,i-1} \mathbf{e}^{-m_{i-1}(T_{i-1}-T_{i-2})} \\ dq_{2,i} &= m_{i-1} \bar{A}_{2,i-1} \mathbf{e}^{m_{i-1}(T_{i-1}-T_{i-2})} - m_{i-1} \bar{B}_{2,i-1} \mathbf{e}^{-m_{i-1}(T_{i-1}-T_{i-2})} \\ dq_{3,i} &= m_{i-1} \bar{A}_{3,i-1} \mathbf{e}^{m_{i-1}(T_{i-1}-T_{i-2})} - m_{i-1} \bar{B}_{3,i-1} \mathbf{e}^{-m_{i-1}(T_{i-1}-T_{i-2})} - \\ &\quad \frac{1}{b_{2,i-1}^2 g} (b_{2,i-1}g(u_2 + 2u_3 T_{i-1} + 3u_4 T_{i-1}^2) + 6Ru_4)\end{aligned}\quad i = 2, 3 \quad (4.24)$$

In summary, Equations (4.18) – (4.24) fully determine the analytical solution to

Equations (4.15) – (4.17) in terms of the unknown parameters C_1 and C_2 in Equation (4.18). The overall solution defined over the whole period ΔT is written more compactly as follows:

$$\theta_{sol}(t) = \sum_{i=1}^3 \theta_{sol,i}(t) (H(t - T_i) - H(t - T_{i-1})) \quad (4.25)$$

where H is the Heaviside function defined:

$$\begin{aligned} H(t - T_i) &= 1, & t < T_i \\ &= 0, & t \geq T_i \end{aligned} \quad (4.26)$$

The piecewise solution θ_{sol} of Equation (4.25) is then substituted into Equation (4.8) and C_1 and C_2 evaluated over $\Delta T = 0.3s$ in the same way as the single section method over $\Delta T = 0.1s$, using Equations (4.9) – (4.13). The method is summarised in the same way as Figure 4.3 with Equations (4.1), (4.5) and (4.6) replaced with Equations (4.14), (4.15) – (4.17) and (4.25), respectively. Hence the same flowchart process of Figure 4.3 applies to this extended, potentially more robust approach.

4.1.3 Analysis and Performance Metrics

The two methods of Equations (4.1) – (4.13) and Equations (4.14) – (4.25) are validated using both synthetic and experimental data. Due to the generally symmetric nature of head motion [Shaw and Liang, 1992], it is reasonable to use a modified sine wave as a basic representation of head motion. This simplification allows the algorithms to be easily tested with different dynamics and noise. The main goals of this validation testing include:

- An analysis using synthetic data to determine the robustness to noise and accuracy of these algorithms;
- To determine and evaluate the robustness and performance of the methods to dynamic motion over the range typically experienced during head motion;
- To test these methods with experimental data, collected using the inverted pendulum apparatus in Figures 2.9 and 2.10.

For the synthetic data, an artificially generated θ represents the “true” head motion and is used to generate the “measured” acceleration signals using the model Equations (2.1) and (2.2). For the experimental data, the true head motion is the angular motion of the inverted pendulum as recorded by the optical encoder measurement. The acceleration signals are directly measured using an accelerometer. In both cases, the error is represented by the absolute error in degrees and the relative percentage error between the calculated θ using the two methods of Equations (4.1) – (4.13) and Equations (4.14) – (4.25), and the “true” θ . The results are summarised by reporting the mean, standard deviation and maximum error. These performance metrics are calculated after any initial transient behaviour in the solution has died away.

4.2 Results and Discussion

4.2.1 Robustness to Noise

A synthetic θ signal is generated using modified sine waves to represent typical head motion. This signal is used to represent the “true” θ , denoted θ_{true} and is defined here as:

$$\theta_{true} = 0.128 + 0.16 \sin(4t + 1.6) + 0.16e^{-(t+0.4)} \cos(2t + 0.8) \quad (4.27)$$

θ_{true} is substituted into the model Equations (2.1) and (2.2) to derive synthetic signals for $A_{T,true}$ and $A_{R,true}$:

$$A_{T,true} = (R/g)\ddot{\theta}_{true} - \sin(\theta_{true}), \quad (4.28)$$

$$A_{R,true} = (R/g)\dot{\theta}_{true}^2 - \cos(\theta_{true}). \quad (4.29)$$

However, to accurately simulate real acceleration, signal noise must be added.

Artificial noise is generated to approximate the experimental noise in Table 2.3, which was measured during model validation. The noise on the measured acceleration signals A_T and A_R is comprised of two sources. The first source is a high frequency raw noise from the accelerometer and circuitry. The second source is a lower frequency modelling error, for example out of plane motion that is not cap-

tured by the encoder. Both sources of noise can be simulated by high and low frequency sine waves. Normalised noise signals modelled on the experimental noise are defined:

$$A_{T,noise} = 0.48 \cos(63.3t) + 0.40 \cos(105.7t) + 0.32 \sin(213t) \quad (4.30)$$

$$A_{R,noise} = 0.40 \cos(63.3t) + 0.26 \sin(63.3t) - 0.35 \cos(105.7t) - \\ 0.20 \sin(105.7t) - 0.30 \cos(213t) - 0.10 \sin(213t) \quad (4.31)$$

where the frequencies 63.3, 105.7 and 213 were determined by fitting to experimental noise signal. The noise signals of Equations (4.30) and (4.31) are added to $A_{T,true}$ and $A_{R,true}$ from Equation (4.28) and (4.29). The resulting functions of time are sampled every 0.01s providing a representation of the “real” measured accelerations $A_{T,real}$ and $A_{R,real}$:

$$A_{T,real} = A_{T,true} + \epsilon_T \bar{A}_{T,true} A_{T,noise} \quad (4.32)$$

$$A_{R,real} = A_{R,true} + \epsilon_R \bar{A}_{R,true} A_{R,noise} \quad (4.33)$$

where ϵ_T and ϵ_R define three different noise amplitudes:

$$\epsilon_T = 0\%, 5.4\%, 10.8\% \quad (4.34)$$

$$\epsilon_R = 0\%, 21.9\%, 43.8\% \quad (4.35)$$

and $\bar{A}_{T,true}$ and $\bar{A}_{R,true}$ are the mean absolute signal amplitudes given by:

$$\bar{A}_{T,true} = \frac{1}{n} \sum_{i=1}^n |A_{T,true,i}| \quad (4.36)$$

$$\bar{A}_{R,true} = \frac{1}{n} \sum_{i=1}^n |A_{R,true,i}| \quad (4.37)$$

where n defines the number of points within the total length of the 4.0s signal tested.

For simplicity in the results that follow, the three noise levels of Equations (4.34) and (4.35) are referred to as 0, Mean, and $2 \times \text{Mean}$, with the Mean referring to the mean experimental percentage errors of 5.4% on A_T and 21.9% on A_R first derived in Table 2.3. Thus, these three levels represent typical, no error and outlying noise cases.

The single section method of Equations (4.1) – (4.13) is denoted Method A, and

the piecewise method of Equations (4.14) – (4.25) is denoted Method B. Both methods are tested with the synthetic acceleration signals derived in Equations (4.32) and (4.33), at the three noise levels, corresponding to Equations (4.34) and (4.35). Method A is implemented with an interval of 0.1s and Method B was implemented using three equal sections over 0.3s. The algorithm of Figure 4.3 is applied over time steps of 0.01s from an initial time 0s to an end time of 4.0s, which covers several motion cycles.

The results are shown in Table 4.1 and plotted for the Mean noise case in Figure 4.5. A calculation of rotation using the static tilt method of Equation (2.6) in Section 2.2.1 is also included in the figure for comparison. However, clearly this static method should not perform well, as it fails to take into account the effects of acceleration due to motion.

Table 4.1: Error response to the presence of noise

Noise	Max (deg)	STD (deg)	Mean (deg)	%
(A) None	0.14	0.01	0.001	0.02
Mean	2.0	0.39	0.42	6.8
2×Mean	2.9	0.56	0.63	10.0
(B) None	0.17	0.02	0.005	0.08
Mean	1.1	0.19	0.17	2.8
2×Mean	1.6	0.28	0.30	4.7

In the zero noise case, Table 4.1 shows that Methods A and B perform extremely well finding the correct solution for θ with a maximum error of 0.14° , which is due to discretisation and round off error. The results deteriorate, as expected, when noise is applied to the simulated data. Both methods have a mean error of less than 1° for each noise case. However, Method B shows superior performance with the maximum, mean and standard deviation of the error being approximately half that of Method A for the same synthetic signal.

The results in Table 4.1 thus suggest Method B is a significantly more accurate method than Method A. The increase in accuracy of Method B is due to solving over a longer period, which increases the amount of motion signal relative to the noise present, thus further constraining the solution via an improved signal to noise ratio.

Also illustrated by Figure 4.5 is the robustness of the methods to unknown

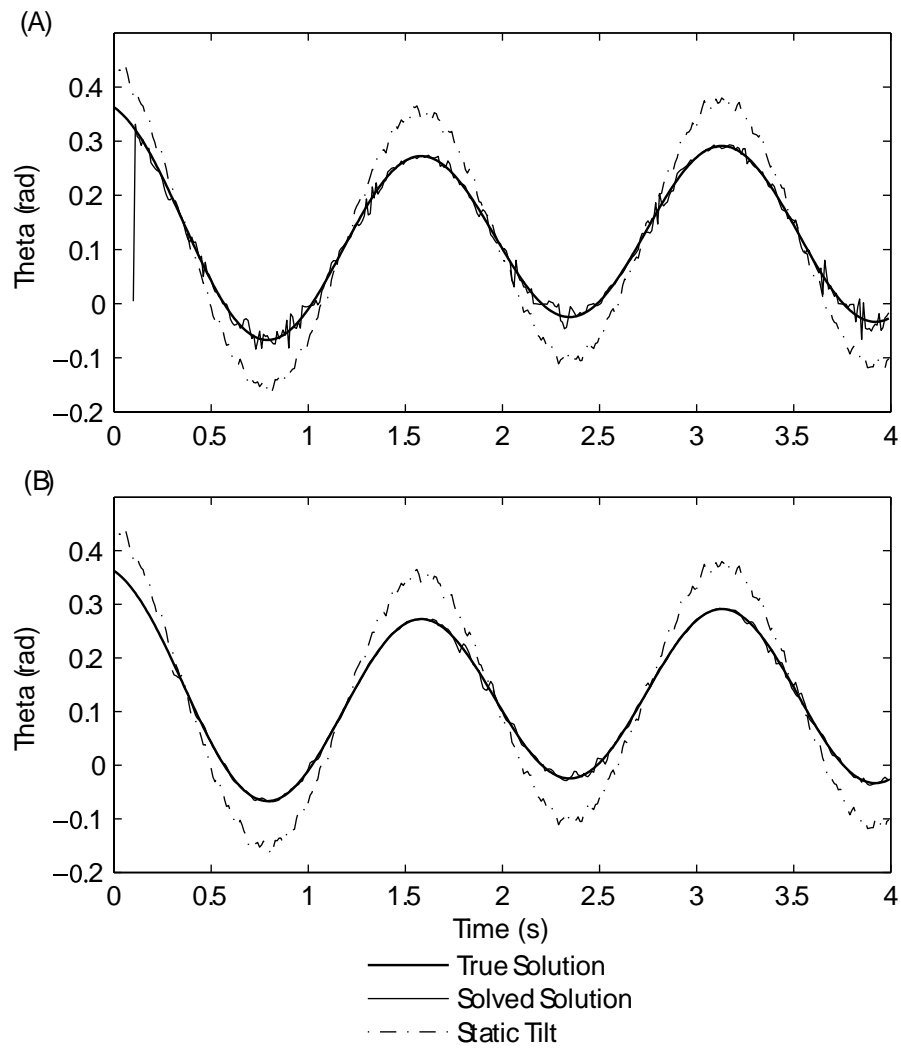


Figure 4.5: Response to the Mean noise added to simulated data using the single section method, Method A, and piecewise section method, Method B. The methods both track quickly to the true solution, despite non a non zero initial condition, and $\theta_{old} = 0$ value.

starting conditions. Each method requires knowledge of prior θ values to make accurate approximations to the sine and cosine curves. In the absence of such information the initial θ_{old} vector is set to 0. However, as seen in Figure 4.5, both methods quickly track to the true solution and any transient dynamics due to the wrong initial conditions die away after a short period of time.

Accelerometer Placement

Further improvements can be achieved by optimising the accelerometer placement. Aligning A_R with gravity gives poor sensitivity to static rotations along this axis. This poor sensitivity is illustrated in Figure 2.11 with the measured A_R having a very small amplitude and a large mean error of 21.9%. Table 4.2 shows the results using Method A and B for the same signals used for the results in Table 4.1, but shifting θ by adding 45° . Note that the settling time of the initial transient section (not shown) is increased due to the large difference between the true θ and the initial assumption that $\theta_{old} = 0$. Shifting the placement of the accelerometer in this way reduces the mean absolute percentage error by a degree of magnitude.

Table 4.2: Error response when accelerometer placement is shifted

Noise	Max (deg)	STD (deg)	Mean (deg)	%
(A) Mean	0.38	0.083	0.085	0.79
(B) Mean	0.20	0.022	0.030	0.28

Using the same absolute noise for a change in the accelerometer placement may not be truly representative of a real case. However, the results of Table 4.2 illustrate the potential for improved performance by carefully positioning the accelerometer so that it is not directly above the centre of rotation. This approach would thus separate the vertical and radial axes in Figure 2.1. In practice, optimal accelerometer placement may be restricted by physical constraints imposed by the application.

4.2.2 Dynamic Performance

One of the key drivers for this work is to improve orientation accuracy in a fully dynamic application. To quantify the dynamic performance of the algorithms of Equations (4.1) – (4.13) and Equations (4.14) – (4.25), a synthetic signal θ_{true} is

generated using a simple sine wave:

$$\theta_{true} = \bar{a} \frac{\pi}{180} \sin(2\pi \bar{f} t) \quad (4.38)$$

where the amplitude $\bar{a} = 10^\circ$ and frequency \bar{f} is varied from 0.1Hz to 2Hz. The $A_{T,true}$ and $A_{R,true}$ signals are generated by substituting Equation (4.38) into Equations (2.1) and (2.2) as was done in Equations (4.28) and (4.29). The “real” A_T and A_R signals $A_{T,real}$ and $A_{R,real}$ are then represented by putting $\epsilon_T = 5.4\%$ and $\epsilon_R = 21.9\%$ into Equations (4.32) and (4.33), corresponding to the mean noise case in Table 4.1. The resulting functions are then discretised as function of time, to match a 100Hz sampling rate. Method A of Equations (4.1) – (4.13), Method B of Equations (4.14) – (4.25), and the static tilt method of Equation (2.6) from Section 2.2.1, are compared by plotting the percentage error in the solution against each frequency, \bar{f} , from 0.1Hz to 2Hz in Figure 4.6.

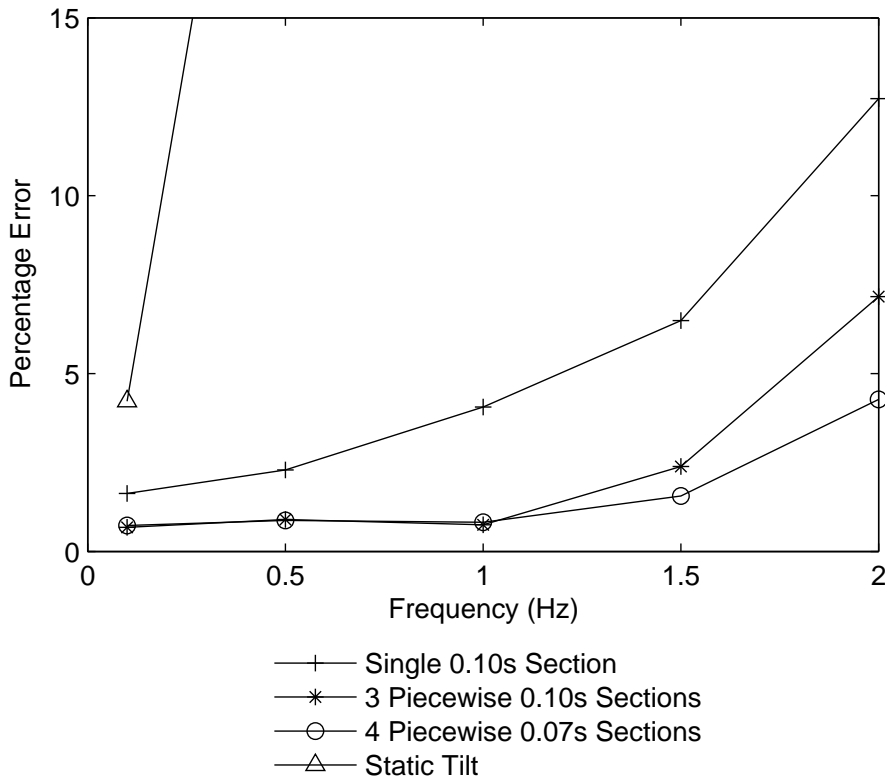


Figure 4.6: The response of the methods presented to increasing dynamics

The results for the static tilt method in Figure 4.6 confirm that its use is rightly limited to stationary or near stationary orientation measurements. Note that the result at 0.1Hz is perhaps unfairly represented. The poor result is largely due to the noise on A_T , as no smoothing or fitting takes place with the implementation of

this method. However, the general trend is that this method cannot account for the increased dynamics and the performance thus quickly drops away as frequency is increased.

The key result in Figure 4.6 is that fitting the model to more data, which is made feasible by the piecewise Method B, improves performance. However, this performance is still limited at higher frequencies by the approximations to A_T and $\sin(\theta)$ given by Equations (4.1), (4.14) and (4.4). The limitations are described as follows.

1. The cubic fit of Equation (4.4) to A_T over the whole period limits the dynamics of A_T permissible within the period. With a 3Hz signal this approach would result in fitting the cubic to almost a complete sine wave period. Consequently, the piecewise method in its current form fails to produce useful results at these higher frequency dynamic inputs.
2. The sine linearisation made in Equations (4.1) and (4.14) for each method becomes less accurate as the range of θ within the fixed 0.1s time periods increases with frequency.

The first limitation could be overcome by, for example, fitting piecewise polynomials over A_T . The second limitation could be overcome by fitting more sections for the same period of time, ΔT . For example, if the number of sections is chosen to be $N = 4$ in Equation (4.14), and $\Delta T = 0.28$, giving shorter sections of $\delta T = 0.07$ s, then with the same cubic A_T , the results are improved as also shown in Figure 4.6. Both of these extensions are investigated in detail in the following chapter.

4.2.3 Experimental Results

Results so far have been based only on simulated data and noise. To validate the methods experimentally in a real environment, the inverted pendulum apparatus of Figures 2.9 and 2.10 is used with an encoder to provide the “true” measure of θ for comparison of Method B and the static tilt method. Method A is ignored based on the simulated data results.

Three experiments were conducted using different frequencies and amplitudes

to cover a wide range of potential head motion. The acceleration data collected was solved for rotation using the piecewise algorithm Method B, of Equations (4.14) – (4.25), with $N = 3$, $\delta T = 0.1s$ sections. A comparison of the output solution from Method B to the reference encoder signal is shown in Figure 4.7 and error metrics are given in Table 4.3.

All three data sets have a mean error less than 1° , including the extreme case of Figure 4.7(C), which oscillates between -36° and $+63^\circ$. Although the maximum error was 3.5° in this case, it is due to the excessively large θ seen. The maximum percentage error relative to the range of motion is 14.70%, with a mean of 3.79%. These overall results validate the premise that an accelerometer combined with an accurate system model can be used to accurately determine dynamic orientation.

Table 4.3: Experimental error results

Data	Max (deg)	STD (deg)	Mean (deg)	%
A ($\approx 0.75\text{Hz}$)	1.7	0.40	0.61	4.25
B ($\approx 1\text{Hz}$)	0.91	0.23	0.27	5.23
C (random)	3.5	0.65	0.92	3.79

4.3 Summary

This chapter presents two methods for solving dynamic rotation using an accelerometer for single degree of rotational freedom. The first method, Method A of Equations (4.1) to (4.13), uses a single section to linearise the sine function in terms of θ within the model equations. However, this restriction limits the length of data that the model can be fitted to in the solution process. The second method, Method B of Equations (4.14) to (4.25), uses a piecewise approach to the linearisation. This approach allows more data to be fitted improving the overall orientation result. The two main contributions included within the chapter are:

- The presentation of an entirely unique and innovative method to solve the unstable tangential ODE, Equation (2.1).
- Validation of the methods and results in simulation and an experimental setting proving the concept that in principle, dynamic model-based orientation tracking can be achieved using an accelerometer.

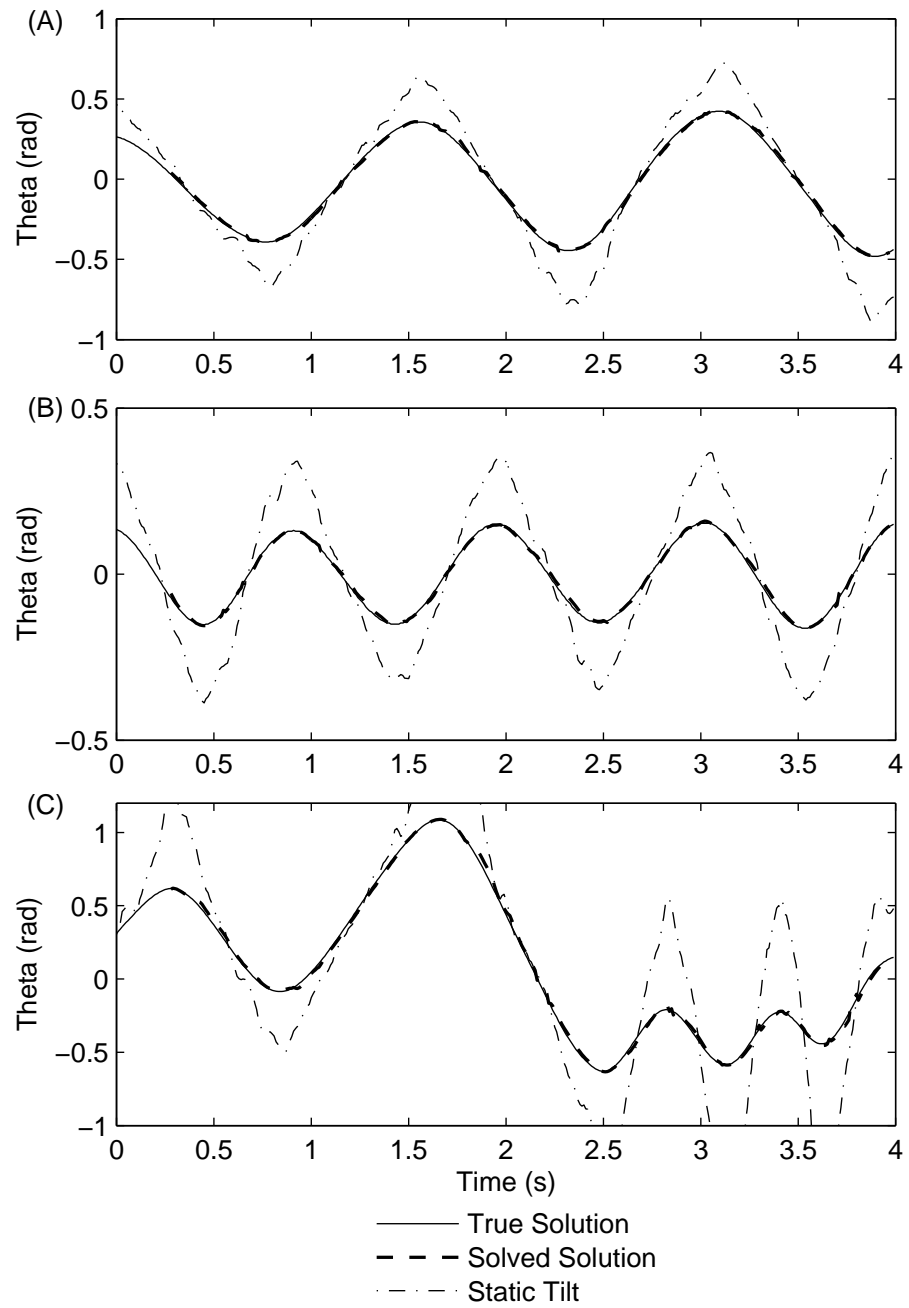


Figure 4.7: Experimental results using the three section piecewise method for (A), (B), and (C) data sets compared to θ_{en}

Comparisons between the methods were made using simulated data with different noise levels applied, and the results given in Tables 4.1 to 4.2 and Figure 4.5. Further comparisons were made with respect to different frequency signals as shown in Figure 4.6. The final Method B was validated with experimental data collected using an accelerometer and an inverted pendulum apparatus. The approximated angle was compared to the true rotational angle measured by an optical encoder and found to be consistently accurate with errors typically well less than 1° .

The piecewise Method B outperforms the single section Method A, with much lower standard deviation and approximately half the error in θ as shown in Table 4.1 and Figure 4.6. However, these results are limited to lower frequency signals, less than 2Hz, by the linearisation period of $\sin(\theta)$ and the fit of the cubic function to A_T . The methods need further improvement to reach the expected dynamic range of head motion, of up to 3Hz.

Chapter 5

Optimised Method and Comparisons

Chapter 4 presented two initial methods described in Equations (4.1) – (4.13) and Equations (4.14) – (4.25) for identifying rotation using the model of Equations (2.1) and (2.2). These methods overcame the instability and ill conditioning discussed in Chapter 3 where conventional approaches failed to achieve accurate results. The methods in Equations (4.1) – (4.13) and Equations (4.14) – (4.25) work perfectly when no noise is present and in experimental tests achieve results with mean absolute errors less than 1° . However, their application is limited to lower frequencies by the polynomial fits made in the algorithmic approaches taken.

Figure 4.6 illustrated the advantages of fitting the model to more data and improving the linearisation of the sine term in Equation (2.1), especially at higher frequency motion. In this chapter these concepts are extended to a more generic method, eliminating the restrictions imposed on the signals by polynomial fitting to the data. This change also broadens the potential uses of the method to other applications that have more dynamic motion than head motion.

5.1 Method

5.1.1 Initial Improvements

Increasing dynamic motion has two major limiting effects on the performance of the piecewise method described by Equations(4.14) – (4.25). Firstly, the range of θ within the interval δT shown in Figure 4.4 increases, demanding a linear fit over a greater portion of the sine curve, and thus reducing the validity of the linearised

approximation in Equation (4.14). Secondly, higher frequency motion results in more complex signals within the period ΔT also shown in Figure 4.4. The simple cubic function of Equation (4.4) fitted to A_T is limited in its ability to fit these more complex signal characteristics. Therefore, to overcome these limitations, the following approach is taken.

The three section approach of Equations (4.14) – (4.25) is first extended to an arbitrary number of sections. For the n th section, the length, δT_n , is defined:

$$\delta T_n = T_n - T_{n-1} \quad (5.1)$$

where T_n is the time at the end of the section and is chosen so that the range of θ , $\delta\theta_n$, within each section is limited as follows:

$$\delta\theta_n = \theta_{max,n} - \theta_{min,n} < 0.1\text{rad} \quad (5.2)$$

Linear expressions are fitted to $\sin(\theta)$ for each period δT_n using the approach in Equations (4.1) – (4.3). The piecewise representation across the whole period ΔT in Equation (4.14) then becomes:

$$\sin(\theta(t)) \simeq b_{1,n} + b_{2,n}\theta \quad T_{n-1} \leq t \leq T_n, \quad n = 1, \dots, N \quad (5.3)$$

where N is the number of sections. Thus, Equations (5.2) – (5.3) define a new approach to improving the $\sin(\theta)$ linearisation by choosing small enough time intervals that restrict the range of θ within each section.

Figure 5.1 compares the θ ranges for the old method of Equation (4.14) where the sections are of constant length δT , against this new adaptive approach of Equations (5.2) – (5.3). Figure 5.1 (A) shows that during rapid motion large changes of θ can occur within the sections of fixed length δT . However, this behaviour is eliminated by the new approach shown in Figure 5.1 (B).

To address the issue arising from the limited ability of the cubic function to fit more complex A_T signals over the whole period ΔT , a continuous piecewise cubic function [Ichida and Kiyono, 1977] is fitted to A_T across the sections defined by Equation (5.2). The resulting approximation to A_T is defined:

$$A_{T,fit,new} = S_n(t) \quad T_{n-1} \leq t \leq T_n, \quad n = 1, \dots, N \quad (5.4)$$

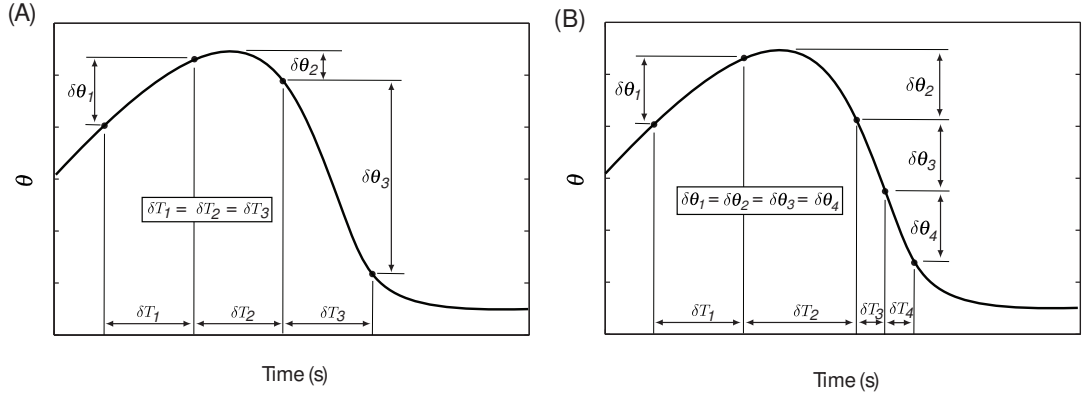


Figure 5.1: Two methods of determining the $\sin(\theta)$ linearisation range; (A) Using a constant δT for each section, (B) Limiting $\delta\theta$ within each section

where each S_n is a cubic function defined:

$$S_n(t) = y_{n-1} + m_{n-1}(t - T_{n-1}) + w_n(t - T_{n-1})^2 + z_n(t - T_{n-1})^3$$

$$T_{n-1} \leq t \leq T_n, \quad n = 1, \dots, N \quad (5.5)$$

where y and m denote the values of the approximating function $S(t)$ and its derivative $S'(t)$ at the knots. For the n th section, the condition for continuity of $S(t)$ and its derivative at T_{n-1} is:

$$y_{n-1} = S_{n-1}(T_{n-1}) = y_{n-2} + m_{n-2}(\delta T_{n-1}) + w_{n-1}(\delta T_{n-1})^2 + z_{n-1}(\delta T_{n-1})^3$$

$$m_{n-1} = S'_{n-1}(T_{n-1}) = m_{n-2} + 2w_{n-1}(\delta T_{n-1}) + 3z_{n-1}(\delta T_{n-1})^2$$

$$n \geq 2 \quad (5.6)$$

The initial conditions for the first section y_0 and m_0 in Equation (5.5) with $n = 1$ and the constants w_n and z_n for $n = 1, \dots, N$, are unknown parameters. These parameters are found by a least squares fit of S_n for $n = 1, \dots, N$ in Equation (5.5) to the measured A_T over the whole period, ΔT . Figure 5.2 schematically illustrates the resulting polynomials over two sections of different lengths δT .

A comparison of the approximating function $A_{T,fit}$ for A_T from Equation (4.4) is made with $A_{T,fit,new}$ in Equation (5.4). This comparison is illustrated in Figure 5.3 for the synthetic acceleration signal $A_{T,true}$ generated from Equation (4.38) and (4.28) where θ has an amplitude \bar{a} of 10° and a frequency \bar{f} of 3Hz. $A_{T,fit}$ from Equation (4.4), which uses a single cubic section over the period $\Delta T = 0.3s$, performs poorly at such a high frequency, having a mean error of 8.5%. However, $A_{T,fit,new}$

from Equation (5.4), which uses multiple cubic sections performs much better with a mean error of 0.5%.

Substituting Equations (5.3) and (5.4) into Equation (2.1), where S is the fitted A_T , produces a set of linear ODEs similar to those in Equations (4.15) – (4.17).

$$(R/g)\ddot{\theta} - (b_{1,n} + b_{2,n}\theta) = S_n \quad T_{n-1} \leq t \leq T_n, \quad n = 1, \dots, N \quad (5.7)$$

Equation (5.7) is solved using the method of Equations (4.18) to (4.25) generating a piecewise solution for θ_{sol} in terms of C_1 and C_2 . The optimal value of C_1 and C_2 are then determined using Equations (4.7) – (4.13) over the whole period ΔT . Evaluating the solution at $t = T_N$ provides the θ for the current time step.

However, the method of Equations (5.2) – (5.7) is still fundamentally limited by the fact that the $\sin(\theta)$ linearisation of Equation (5.3) and the cubic function of Equation (5.4) are represented over the same period of length δT_n of Equation (5.2). Merely limiting the range of theta as shown in Figure 5.1 does not necessarily provide a good fit for $A_{T,fit,new}$ in Equation (5.4) over the same section. For example, very small oscillations in θ would not suggest that any sections within ΔT are required. However, small oscillations of θ would result in a complex acceleration signal resulting in a poor cubic fit to the measured A_T . This approach could be extended to prevent such situations. For example, a threshold could be set on the mean fitting error to the measured A_T data. However, such approaches can get increasingly complex, computationally intensive and a consistent threshold would be hard to find.

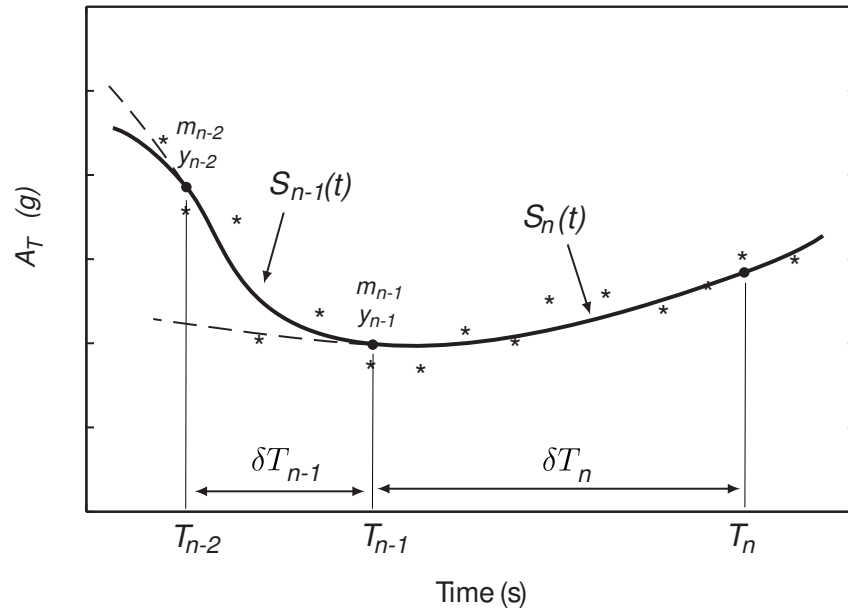


Figure 5.2: Schematic of piecewise cubic sections fitted the measured A_T data

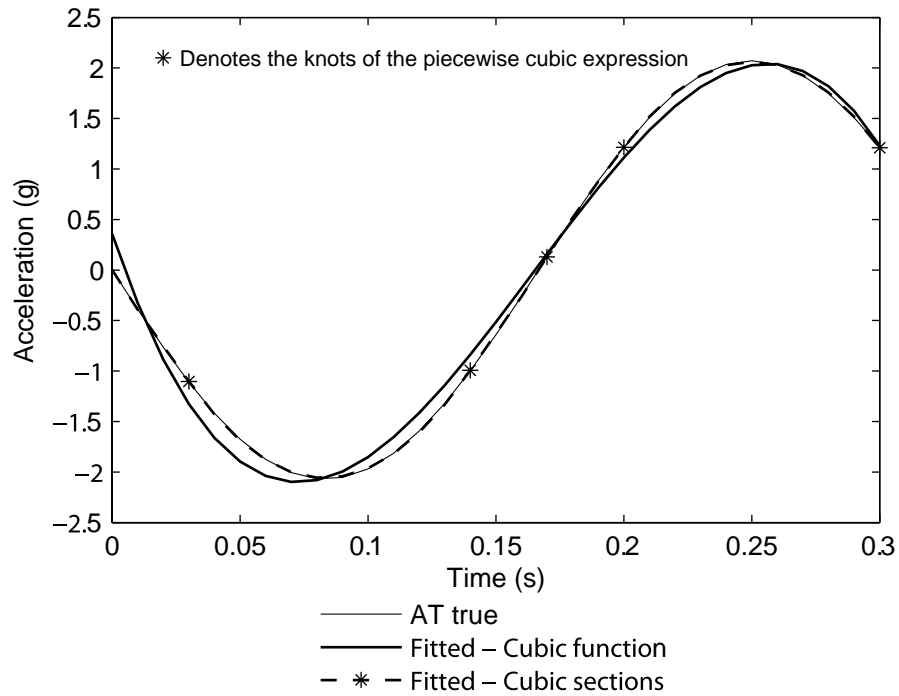


Figure 5.3: Comparison of the fit of a single cubic expression versus multiple cubic sections to a synthetic A_T signal with no noise added, generated from a 3Hz θ signal with a 10° amplitude

5.1.2 Generalised Approach

The piecewise methods of Equations (4.14) – (4.25) and Equations (5.2) – (5.7) are refined where the length of each section, δT , is equal to the resolution of the sample rate, Δt , and the number of sections, N , is equal to the number of time steps, k . Thus, an individual linear ODE of the form in Equation (4.15) is constructed for each sampling step. When the combined set of these linear ODEs are solved analytically based on the formulas in Equations (4.18) – (4.25) the solution approximates that of the original non linear ODE, Equation (2.1). This concept is illustrated in Figure 5.4, where i is used to denote an individual time step or section. Figure 5.4 (A) describes the measured tangential acceleration A_T , Figure 5.4 (B) shows the previously calculated θ_{old} vector and the the next point θ_{new} which is to be determined, and Figure 5.4 (C) illustrates the linearisation of $\sin(\theta)$ about the mean of each section.

Equation (4.4) from the piecewise method presented in Chapter 4 used a cubic fit to the measured acceleration to enable an analytical solution and aid in filtering. In this method, the raw acceleration measurements are used with a linear expression defining A_T between the measurements. For a given set of measurements $A_{T,0}, \dots, A_{T,k}$ taken at points t_0, \dots, t_k shown in Figure 5.4 (A), the resulting approximation is defined:

$$A_{T,fit} = \sum_{i=1}^k A_{T,fit,i} (H(t - t_i) - H(t - t_{i-1})) \quad (5.8)$$

where substituting $T_i = t_i$ into Equation (4.26) redefines H , the Heaviside function as:

$$\begin{aligned} H(t - t_i) &= 1, & t < t_i \\ &= 0, & t \geq t_i \end{aligned} \quad (5.9)$$

and $A_{T,fit,i}$ defines the linear expression for A_T over the i th section:

$$A_{T,fit,i} = u_{1,i} + u_{2,i}t \quad i = 1, \dots, k \quad (5.10)$$

where:

$$\begin{aligned} u_{1,i} &= A_{T,i} - (i - 1)(A_{T,i} - A_{T,i-1}) \\ u_{2,i} &= \frac{A_{T,i} - A_{T,i-1}}{\Delta t} \end{aligned} \quad (5.11)$$

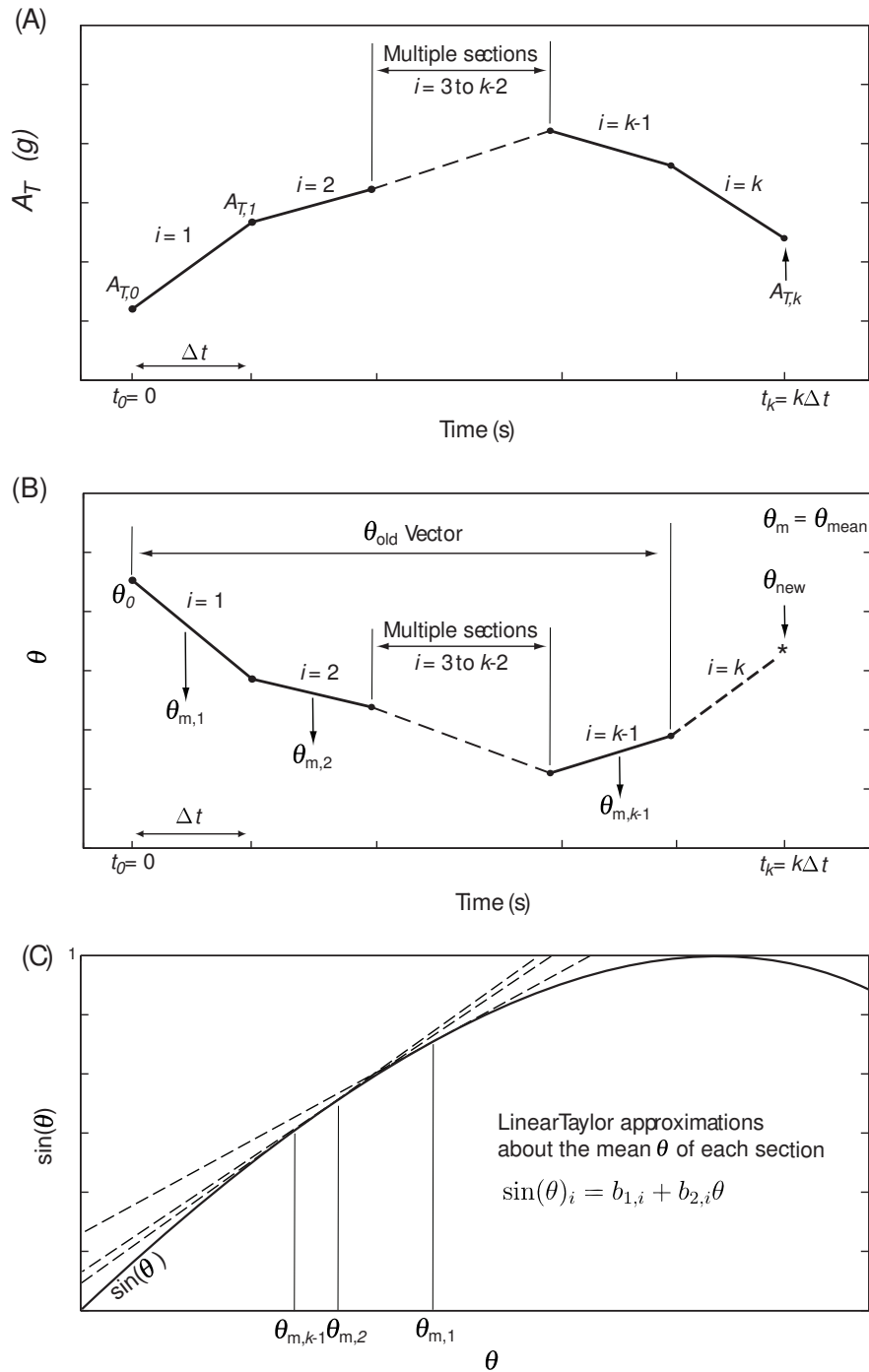


Figure 5.4: The generalised method showing A_T , θ and $\sin(\theta)$

A new approach to linearising $\sin(\theta)$ is shown in Figure 5.4. This new approach is required for the case where θ_i and θ_{i+1} are the same. In this limiting case, only a point is defined on the sine curve making a linear least squares fit, as was done in Equations (4.1) – (4.3), impossible. It is assumed that there is only a very small range of θ within each section of length Δt . Thus, the sine curve can be linearised by the tangent to the curve about the mean θ . The mean θ , $\theta_{m,i}$ is therefore defined:

$$\theta_{m,i} = \frac{(\theta_{i-1} + \theta_i)}{2} \quad (5.12)$$

The linear tangent is generated using a first order Taylor series approximation in Equation (5.13).

$$f(a) + \frac{f'(a)}{1!}(x - a) \quad (5.13)$$

where f denotes a function of x to be fitted about a point a . Evaluating Equation (5.13) for the sine function about $\theta_{m,i}$ defines $\sin(\theta)$ for each section. The expression for $\sin(\theta)$ over the solution period is represented as follows:.

$$\sin(\theta)_i = b_{1,i} + b_{2,i}\theta \quad i = 1, \dots, k \quad (5.14)$$

where:

$$\begin{aligned} b_{1,i} &= \sin(\theta_{m,i}) - \cos(\theta_{m,i})\theta_{m,i} \\ b_{2,i} &= \cos(\theta_{m,i}) \end{aligned} \quad (5.15)$$

For the k th section $\theta_k = \theta_{new}$ is unknown, as shown in Figure 5.4 (B). Thus, the approximation to $\sin(\theta)$ with $i = k$ in Equation (5.14) is made with the assumption:

$$\begin{aligned} b_{1,k} &= b_{1,k-1} \\ b_{2,k} &= b_{2,k-1} \end{aligned} \quad (5.16)$$

In other words, the linearisation of $\sin(\theta)$ in the $(k - 1)$ section is extended to the k th section.

Substituting Equations (5.10) and (5.14) into the model Equation (2.1) provides a set of linear ODEs, describing the motion over the solution period:

$$(R/g)\ddot{\theta} - (b_{1,i} + b_{2,i}\theta) = A_{T,fit,i} \quad i = 1, \dots, k \quad (5.17)$$

where $A_{T,fit,i}$ is defined in Equation (5.10).

The analytical solution to Equation (5.17) is the same as Equation (4.18) – (4.25) except u_1, u_2, u_3, u_4 are defined as follows:

$$\begin{aligned} u_1 &= u_{1,i} \\ u_2 &= u_{2,i} \\ u_3 &= 0 \\ u_4 &= 0 \quad i = 1, \dots, k \end{aligned} \quad (5.18)$$

In addition the time that denotes the end of each section T_i of Figure 4.4 and Equation (4.18) is changed to t_i to be equivalent to sampling time.

However, to better physically and geometrically interpret the parameters C_1 and C_2 , and allow a computationally faster solution method, the solution to the set of Equations (5.17) is represented in terms of the initial conditions θ_0 and $\dot{\theta}_0$.

To perform this reformulation, the parameters of Equation (5.18) are substituted into Equations (4.18) and (4.19) and evaluated at $t = 0$ for $i = 1$, which yields:

$$\theta_{sol,1}(0) = \theta_0 = C_1 + C_2 - \frac{1}{b_{2,1}}(b_{1,1} + u_{1,1}) \quad (5.19)$$

$$\dot{\theta}_{sol,1}(0) = \dot{\theta}_0 = -m_1 C_1 + m_1 C_2 - \frac{u_{2,1}}{b_{2,1}} \quad (5.20)$$

Solving Equations (5.19) and (5.20) for C_1 and C_2 gives:

$$\begin{aligned} C_1 &= \frac{1}{2}\theta_0 - \frac{1}{2m_1}\dot{\theta}_0 + \frac{1}{2b_{2,i}^{3/2}g^{1/2}}((b_{2,i}g)^{1/2}(b_{1,1} + u_{1,1}) - u_{2,1}R^{1/2}) \\ C_2 &= \frac{1}{2}\theta_0 + \frac{1}{2m_1}\dot{\theta}_0 + \frac{1}{2b_{2,i}^{3/2}g^{1/2}}((b_{2,i}g)^{1/2}(b_{1,1} + u_{1,1}) + u_{2,1}R^{1/2}) \end{aligned} \quad (5.21)$$

Equations (5.21) along with the parameters of Equation (5.18) are then substituted into the solution of Equations (4.18) and (4.19). These manipulations provide the required solution θ_{sol} in terms of θ_0 and $\dot{\theta}_0$.

For ease of future reference, this reformulated solution is summarised as follows:

$$\theta_{sol}(t) = \sum_{i=1}^k \theta_{sol,i}(t) (H(t - t_i) - H(t - t_{i-1})) \quad (5.22)$$

$$\begin{aligned}
& \theta_{sol,i}(t) \equiv \text{Equation (4.18)} \\
\text{where: } & \{u_1, \dots, u_4\} \equiv \text{Equation (5.18)} \\
& \{C_1, C_2\} \equiv \text{Equation (5.21)}
\end{aligned} \tag{5.23}$$

and H is the Heaviside function defined in Equation (5.9). For completeness, the full expressions for θ_{sol} are derived independently from the solution of Equation (4.18) in Appendix A.

Another change to the approach of Equations (4.14) – (4.25) is to replace the $\cos(\theta)$ approximation in Equation (4.7) by the following linear expression:

$$\cos(\theta)_i = c_{1,i} + c_{2,i}\theta \quad i = 1, \dots, k \tag{5.24}$$

where $c_{1,i}$ and $c_{2,i}$ are derived using the same approach as for $b_{1,i}$ and $b_{2,i}$ in Equation (5.14), and are defined:

$$\begin{aligned}
c_{1,i} &= \cos(\theta_{m,i}) + \sin(\theta_{m,i})\theta_{m,i} \\
c_{2,i} &= -\sin(\theta_{m,i})
\end{aligned} \tag{5.25}$$

With small sections, the cosine curve is close to linear. Therefore, Equation (5.24) is an accurate approximation as well as minimising computation due to the simpler linear expression.

In a similar way to Equation (5.16), the linearisation of $\cos(\theta)$ in the $(k-1)$ th section is extended to the k th section as follows:

$$\begin{aligned}
c_{1,k} &= c_{1,k-1} \\
c_{2,k} &= c_{2,k-1}
\end{aligned} \tag{5.26}$$

Substituting Equations (5.22) – (5.24) into Equation (2.2) gives a new expression for A_R :

$$A_{R,sol} = \sum_{i=1}^k A_{R,sol,i}(H(t - t_i) - H(t - t_{i-1})) \tag{5.27}$$

where $A_{R,sol,i}$ defines an expression for A_R over the i th section:

$$A_{R,sol,i} = (R/g)\dot{\theta}_{sol,i}^2 - (c_{1,i} + c_{2,i}\theta_{sol,i}) \quad i = 1, \dots, k \tag{5.28}$$

and H is the Heaviside function defined in Equation (5.9).

$A_{R,sol}$ in Equation (5.27) is now in terms of the unknown θ_0 and $\dot{\theta}_0$ values in Equation (5.22). Finding the optimal θ_0 and $\dot{\theta}_0$ values follows a similar approach to the method of Equations (4.9) – (4.13) for finding the optimal C_1 and C_2 values. More specifically, the θ_0 and $\dot{\theta}_0$ values that enable the best least squares fit of $A_{R,sol}$ in Equation (5.27) to the measured radial acceleration A_R from Equation (2.4) are found. The time points in Equation (5.27), t_0, \dots, t_k , are where A_R is measured, with t_k defined as the time point where θ is unknown as shown in Figure 5.4.

Consider the following objective function:

$$\Omega(\theta_0, \dot{\theta}_0) = \sum_{i=0}^k \left(A_{R,sol}(t_k - i\Delta t) - A_R(t_k - i\Delta t) \right)^2 \quad (5.29)$$

where $A_{R,sol}$ is defined by Equations (5.27) and (5.28) and Δt is the sampling period of the measured A_R . Note that $A_{R,sol}(t_k - i\Delta t)$ only requires $\theta_{sol,i}$ and $\dot{\theta}_{sol,i}$ at the measured points which correspond to all the initial conditions of Equations (4.21) – (4.24) combined with Equation (5.23), all of which have already been calculated and stored as a result of constructing the solution θ_{sol} in Equations (5.22) and (5.23). Thus, using these precalculated values along with $\theta_{sol,k}$, an analytical expression for the objective function in Equation (5.29) can be readily derived with minimal computation.

Setting the gradient $\nabla_{\theta_0, \dot{\theta}_0} \Omega = 0$ of Equation (5.29) yields:

$$\frac{\partial}{\partial \theta_0} \left(\sum_{i=0}^k \left(A_{R,sol}(t_k - i\Delta t) - A_R(t_k - i\Delta t) \right)^2 \right) = 0 \quad (5.30)$$

$$\frac{\partial}{\partial \dot{\theta}_0} \left(\sum_{i=0}^k \left(A_{R,sol}(t_k - i\Delta t) - A_R(t_k - i\Delta t) \right)^2 \right) = 0 \quad (5.31)$$

However, continually evaluating all 9 solutions of the coupled set of multivariate polynomials in Equations (5.30) and (5.31) is time consuming. Furthermore in practice, it is only one of these solutions that minimises the objective function in Equation (5.29) which is required. Given that the algorithm moves forward with only small time steps of 0.1s, a close approximation to the optimal θ_0 and $\dot{\theta}_0$ values is already known from the previous time step. Based on this observation, the following

simplification can be made.

Given a computed $x_0 = \theta_{0,old}$ and $y_0 = \dot{\theta}_{0,old}$ from the previous time step the following approximate objective $\bar{\Omega}(\theta_0, \dot{\theta}_0)$ function is defined:

$$\begin{aligned} \bar{\Omega}(\theta_0, \dot{\theta}_0) = & \Omega|_{x_0, y_0} + \frac{\partial}{\partial \theta_0}(\Omega)|_{x_0, y_0}(\theta_0 - \theta_{0,old}) + \frac{\partial}{\partial \dot{\theta}_0}(\Omega)|_{x_0, y_0}(\dot{\theta}_0 - \dot{\theta}_{0,old}) + \\ & \frac{\partial}{2\partial \theta_0^2}(\Omega)|_{x_0, y_0}(\theta_0 - \theta_{0,old})^2 + (\theta_0 - \theta_{0,old}) \frac{\partial}{\partial \theta_0 \partial \dot{\theta}_0}(\Omega)|_{x_0, y_0}(\dot{\theta}_0 - \dot{\theta}_{0,old}) + \\ & \frac{\partial}{2\partial \dot{\theta}_0^2}(\Omega)|_{x_0, y_0}(\dot{\theta}_0 - \dot{\theta}_{0,old})^2 \end{aligned} \quad (5.32)$$

Setting the gradient $\nabla_{\theta_0, \dot{\theta}_0} \bar{\Omega} = 0$ now yields two first order multivariate polynomial equations in θ_0 and $\dot{\theta}_0$:

$$\frac{\partial}{\partial \theta_0} \bar{\Omega} = 0 \quad (5.33)$$

$$\frac{\partial}{\partial \dot{\theta}_0} \bar{\Omega} = 0 \quad (5.34)$$

There is now only one solution of Equations (5.33) and (5.34) to compute which is a significant saving computationally.

This estimated solution is the optimal solution which minimises $\bar{\Omega}$ of Equation (5.32) and is denoted $\{\theta_{0,est}, \dot{\theta}_{0,est}\}$. To ensure the estimate corresponds closely to the true global minima of the surface Ω in Equation (5.29), $\{\theta_{0,est}, \dot{\theta}_{0,est}\}$ are denoted as $\{\theta_{0,old}, \dot{\theta}_{0,old}\}$ in Equation (5.32). Solving Equations (5.33) and (5.34) now defines a new estimate for $\{\theta_{0,est}, \dot{\theta}_{0,est}\}$. This iterative process is repeated until the change in the objective function, $\Omega(\theta_{0,est}, \dot{\theta}_{0,est})$, is less than 0.001 or 10 iterations have passed. This method converges to the solution very quickly, typically in 2 or 3 iterations, providing significant computational savings.

The final optimal solution $\{\theta_{0,opt}, \dot{\theta}_{0,opt}\}$ is then substituted into Equations (5.22) and (5.23) and θ_{sol} evaluated at the time $t = t_k$ in Figure 5.4 to obtain $\theta = \theta_{new}$. The value for θ_{old} is then updated to include θ_{new} at time t_k and the overall process is repeated again for the next time step and solution. The final algorithm is summarised in the flowchart of Figure 5.5.

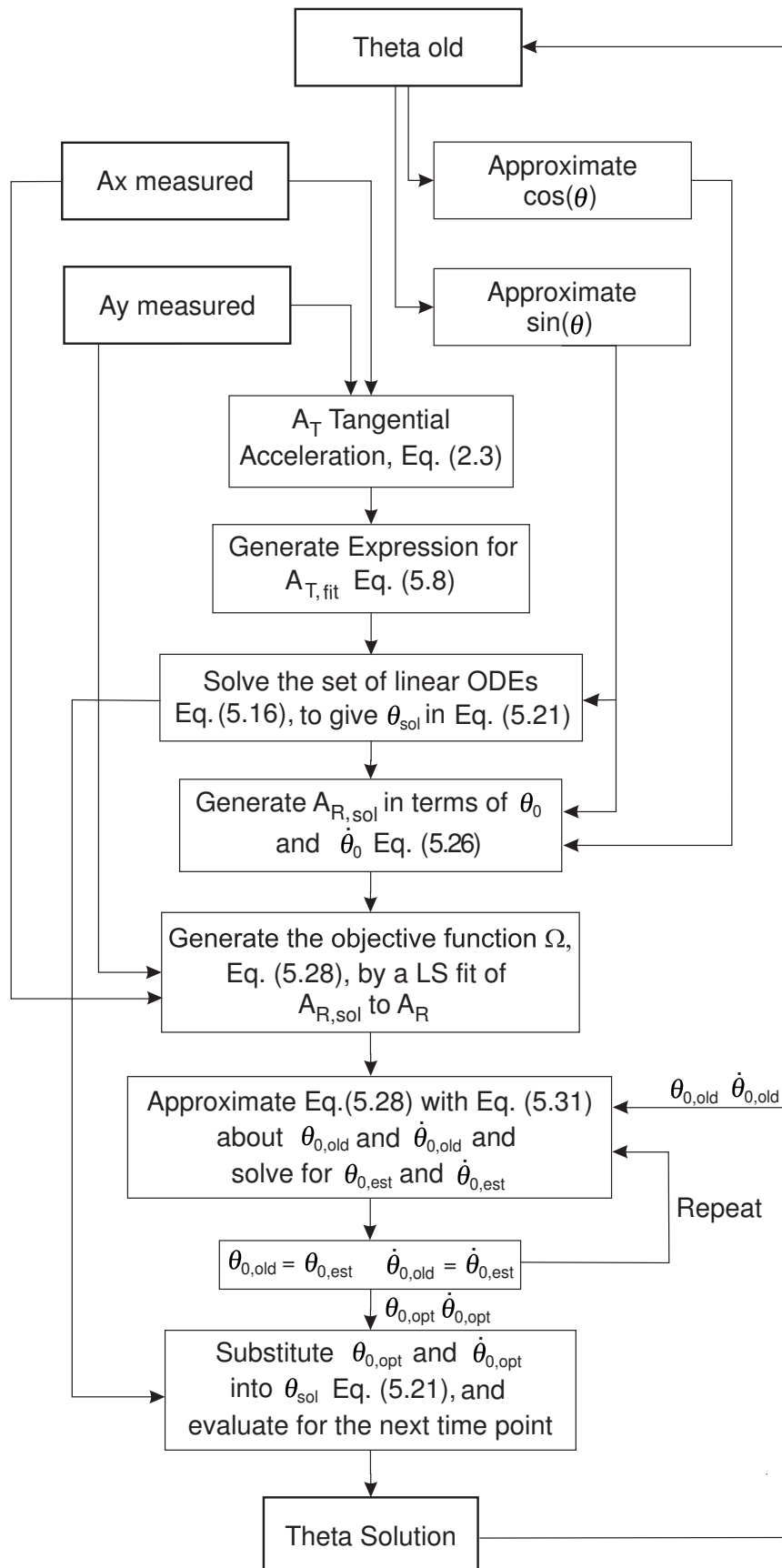


Figure 5.5: Flowchart for the generalised method

5.2 Results and Discussion

5.2.1 Dynamic Performance

The dynamic performance of the generalised method of Equations (5.8) – (5.34) and Figure 5.5 is compared to the single section method of Equations (4.1) – (4.13) and the piecewise method of Equations (4.14) – (4.25) from Chapter 4. Synthetic signals are generated for θ_{true} from Equation (4.38) where the amplitude $\bar{a} = 10^\circ$ and frequency \bar{f} is varied from 0.1 – 3Hz. This approach is designed to test the generalised method up to the highest frequency expected in head motion.

The acceleration signals, $A_{T,true}$ and $A_{R,true}$, are derived by substituting θ_{true} into Equations (2.1) and (2.2). The “real” $A_{T,real}$ and $A_{R,real}$ signals are generated from Equations (4.32) and (4.33), where the noise is defined in Equations (4.30) and (4.31) and scaled to the mean experimental noise by setting $\epsilon_T = 5.4\%$ and $\epsilon_R = 21.9\%$ in the respective equations. The resulting functions for Equations (4.32) and (4.33) are then discretised to achieve a sample rate of 100Hz as before.

The signals generated from 0.1 – 2Hz are the same as those used to generate the results over this range shown in Figure 4.6. Hence, a direct comparison between the methods is enabled over this range, but not for 2 – 3Hz. The generalised method is therefore applied over a 4 second signal length, using the time period of $\Delta T = 0.3s$.

The results of the generalised method of Equations (5.10) – (5.34) are given in Figure 5.6, which also plots the performance of the single 0.1s section and the 3 piecewise 0.1s section methods, which are repeated here from Figure 4.6. Figure 5.6 shows that the generalised method is a significantly more accurate method over all frequencies, with improved robustness to increasing dynamics. However, Figure 5.6 also shows that the method’s accuracy decreases with increasing frequency. This trend is due to the measurement frequency staying fixed at $\Delta t = 0.01s$ at higher motion frequencies. Thus, less information is captured for each cycle.

In principle this trend could be prevented by a higher measurement frequency, but in practice this rate may be limited by the hardware and, equally importantly, the signal to noise ratio. Noise defined by Equations (4.30) and (4.31) has been applied independently of the signal frequencies during this testing. This approach

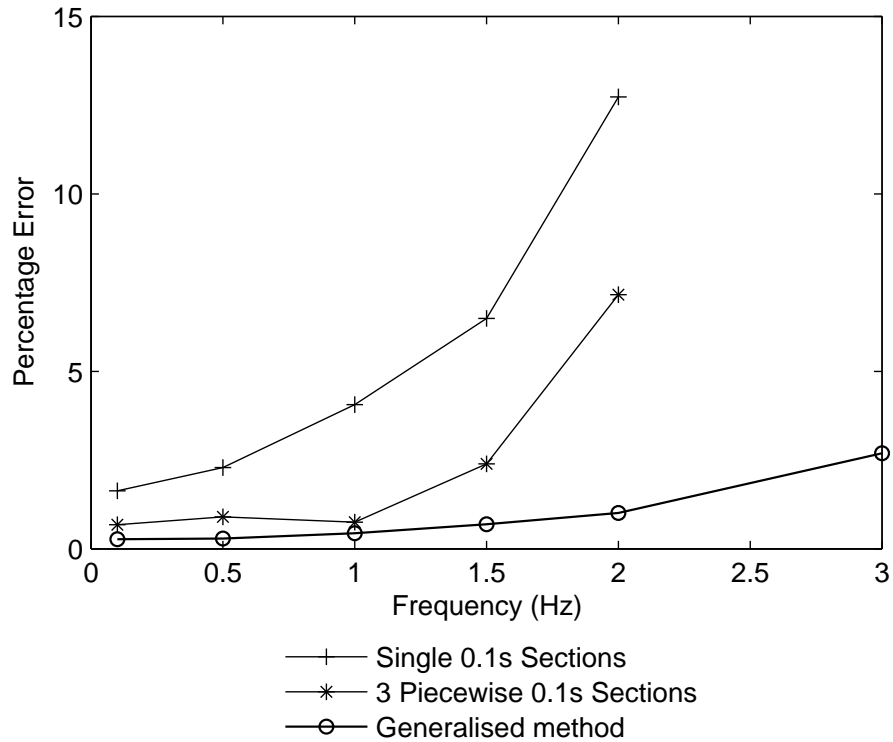


Figure 5.6: The improved response of the Generalised Method to increasing dynamics

is unlikely to completely and accurately represent experimental results. However, it does provide an initial test of the methods prior to experimental validation.

For example, in an extreme case a full cycle of a 10Hz signal is only captured by 10 noisy measurements when sampled at 100Hz. Sampling the 10Hz at signal at 1000Hz would effectively give no difference in error to a 1Hz signal sampled at 100Hz. Hence, the results of Figure 5.6 can be readily scaled within reason, in this fashion.

A further practical consideration is that at higher frequencies the centripetal component of acceleration in Equation (2.2) can be significant. Centripetal acceleration is derived from the rotational velocity $\dot{\theta}$. Thus, in terms of the pendulum model, the centripetal acceleration reaches a maximum at the centre, and is zero at the stationary end points of the manual oscillatory cycle. This behaviour can result in the radial acceleration A_R being double the frequency of the tangential acceleration A_T if the frequency of oscillation is high enough. Therefore, the measured A_R can become a very poor quality signal at higher frequencies of motion.

5.2.2 Experimental Results and Comparisons

To further validate the new method and Figure 5.6, experimental data is collected for the simple one degree of rotational freedom case using the inverted pendulum apparatus of Figures 2.9 and 2.10. These experiments were conducted in a similar way to those used to verify the piecewise method of Equations (4.14) – (4.25). These experiments also utilised an ADXRS150 MEMS gyroscope [Analogue Devices Inc, 2007] and an Inertia Cube 3 [Inetersense Inc, 2007] to provide a means of comparison with inertial systems commonly utilised to determine orientation.

The Inertia Cube 3 is an expensive and specialised item of equipment. To gain the best results from this device, its enhancement setting was set to option “2” and the prediction feature disabled. The heading of the device was reset at the start of each experiment to ensure that the reported pitch agreed with the in plane motion of the pendulum. The gyro was also attached so that its axis sensitive to rotation was in the plane of motion. The gyro, Inertia Cube 3, and accelerometer are seen attached to the pendulum in Figure 5.7.

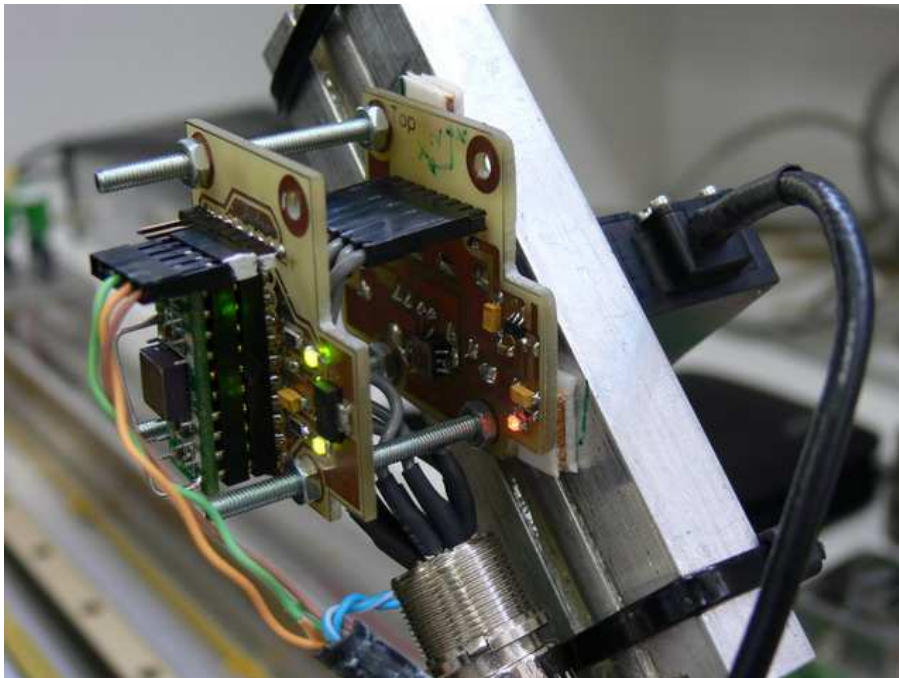


Figure 5.7: Sensing devices used for comparisons attached to the pendulum. From left to right, the gyroscope, accelerometer, and Inertia Cube 3 (black box)

The manual oscillation of the pendulum was synchronised to audible signals, covering a range frequencies from 0 – 3Hz. This procedure provided accurate rota-

tion frequencies, and corresponding acceleration signals. This approach enabled the validation and comparisons of the generalised method of Equations (5.8) – (5.34) to be made with other devices over a broad dynamic range. A signal of length 4 seconds is utilised. The results from the generalised method along with the Inertia Cube 3, and Analogue Devices gyro are summarised in Table 5.1. The performance metrics include the maximum, mean, and standard deviation of the absolute error, and the relative mean percentage error. The mean absolute percentage error for each measurement device or method is plotted against the frequency in Figure 5.8.

Table 5.1: Generalised method experimental error results for frequency

	Frequency	Max (deg)	STD (deg)	Mean (deg)	%
Generalised Method	$\approx 0.25\text{Hz}$	0.49	0.11	0.13	1.43
	$\approx 0.50\text{Hz}$	0.53	0.12	0.17	1.40
	$\approx 1.00\text{Hz}$	0.51	0.13	0.22	1.46
	$\approx 2.00\text{Hz}$	0.72	0.18	0.25	3.78
	$\approx 3.00\text{Hz}$	1.02	0.28	0.43	13.6
Inertia Cube 3	$\approx 0.25\text{Hz}$	0.71	0.15	0.23	2.48
	$\approx 0.50\text{Hz}$	1.06	0.25	0.46	2.87
	$\approx 1.00\text{Hz}$	1.36	0.21	0.30	4.12
	$\approx 2.00\text{Hz}$	1.39	0.23	0.28	5.58
	$\approx 3.00\text{Hz}$	1.48	0.26	0.40	9.72
Gyroscope	$\approx 0.25\text{Hz}$	1.32	0.31	0.37	4.01
	$\approx 0.50\text{Hz}$	0.78	0.21	0.31	4.26
	$\approx 1.00\text{Hz}$	0.70	0.19	0.28	4.04
	$\approx 2.00\text{Hz}$	0.83	0.19	0.32	6.45
	$\approx 3.00\text{Hz}$	0.91	0.22	0.36	9.12

Figure 5.8 illustrates the strength of the performance of the generalised method. This method outperforms both the Inertia Cube 3 and a simple MEMS gyro at frequencies below 2Hz. However, at the higher frequency of 3 Hz the experimental results show the same trend observed with synthetic results in Figure 5.6. This latter result is partly explained by the noise and sampling rate, as discussed earlier.

However, direct manual oscillation of the pendulum, without inducing any out of plane disturbances is a challenging task, especially at higher frequencies. These other disturbances contribute to increased modelling error within the acceleration signals at higher frequencies and therefore are a potentially less suitable test for the method. Further work in the future should extend the model and methods to out of plane motions.

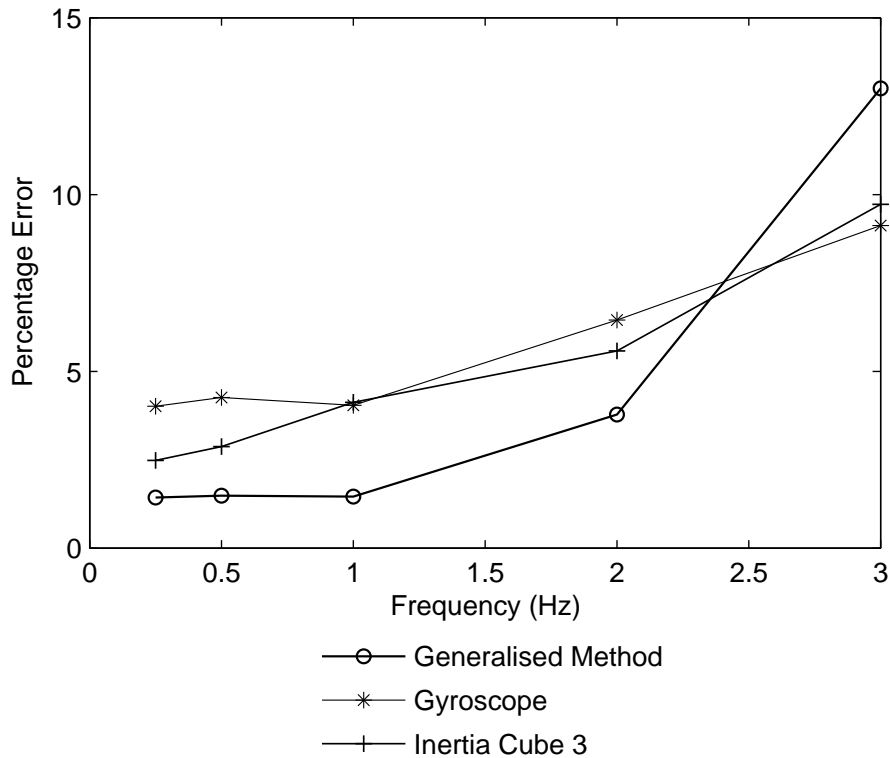


Figure 5.8: Experimentally derived frequency response and comparisons of the generalised method with the Inertia Cube 3 and Gyroscope.

Overall, due to significant modelling error, particularly at higher frequencies, the results do not reach the same levels of performance as those demonstrated with the synthetic data in Figure 5.6. However, the mean absolute percentage error of 1.4% and 1.46% at 0.5Hz and 1Hz compares very favourably with the experimental results for the piecewise method of Equations (4.14) – (4.25), which achieved errors of 4.25% and 5.23% for 0.75Hz and 1Hz respectively, as shown in Table 4.3 and Figure 4.7.

The gyro and Inertia Cube show a similar trend in Figure 5.8. This similarity in the trend occurs because the Inertia Cube 3 relies heavily on its gyros during highly dynamic motion. For the short 4 second section of signals analysed and compared in the results of Table 5.1 and Figure 5.8, the gyro performs well. Over longer durations, the drift as discussed in Section 1.4, corrupts the results. The Inertia Cube 3 compensates for this drift by using its accelerometers and magnetometers. However, at continued high frequency motion some drift can be observed in the orientation solution from the Inertia Cube 3.

Results from each device for a random motion signal are shown for a much longer 15 second signal in Figure 5.9. The corresponding absolute error for each result is plotted in Figure 5.10 and the performance metrics of the absolute error summarised in Table 5.2.

Table 5.2: Generalised method experimental error results for a 15 second signal

Device/Method	Max (deg)	STD (deg)	Mean (deg)	%
Generalised Method	2.51	0.41	0.42	2.61
Inertia Cube 3	3.70	0.87	0.97	5.98
Gyroscope	12.4	4.00	5.62	19.11

Over the 15 second signal, the generalised method shows greater accuracy than the other devices. The generalised method has a mean absolute percentage error of 2.61% which is approximately half the error of the Inertia Cube 3 having a mean absolute percentage error 5.98%. The generalised method and the Inertia Cube 3 both perform much better than the gyroscope, which performs poorly over the longer signal due to drift. The general method shows superior performance because the method remains inherently registered to gravity, while the Inertia Cube 3 and gyro experience drift. Thus in this case the generalised method is more robust.

5.3 Summary

This chapter presented approaches to overcome the limitations of the single section method of Equations (4.1) – (4.13) and piecewise method of Equations (4.14) – (4.25) that were presented in Chapter 4. These limitations restricted the performance at the higher frequencies of 1–2Hz, likely to be encountered in head tracking applications. Various approaches to improving this dynamic performance were discussed. The generalised method of Equations (5.8) – (5.34) and Figure 5.5 provides a simple and robust solution.

This generalised method extended the method of Equations (4.14) – (4.25) to a solution that is constructed over each sampling time step. This construction forms a linear ODE for each small period Δt which improves the accuracy of the linearisation and avoids complex adaptive solutions. Solving the set of ODEs provides a highly accurate and robust solution for θ across the range of frequencies that this application is concerned with.

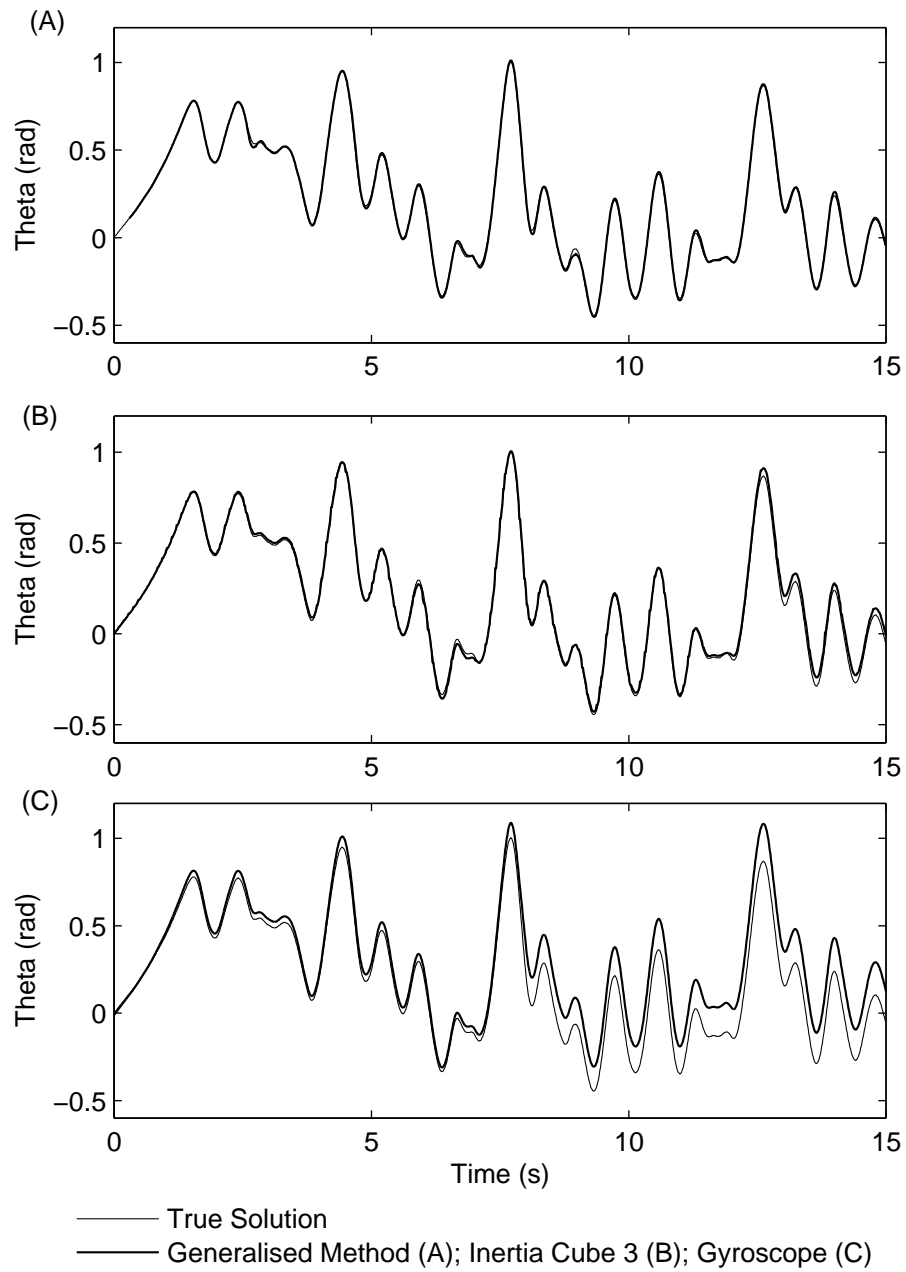


Figure 5.9: Experimental comparisons to determining orientation, θ , using the Generalised Method (A), Inertia Cube 3 (B), and Gyroscope (C)

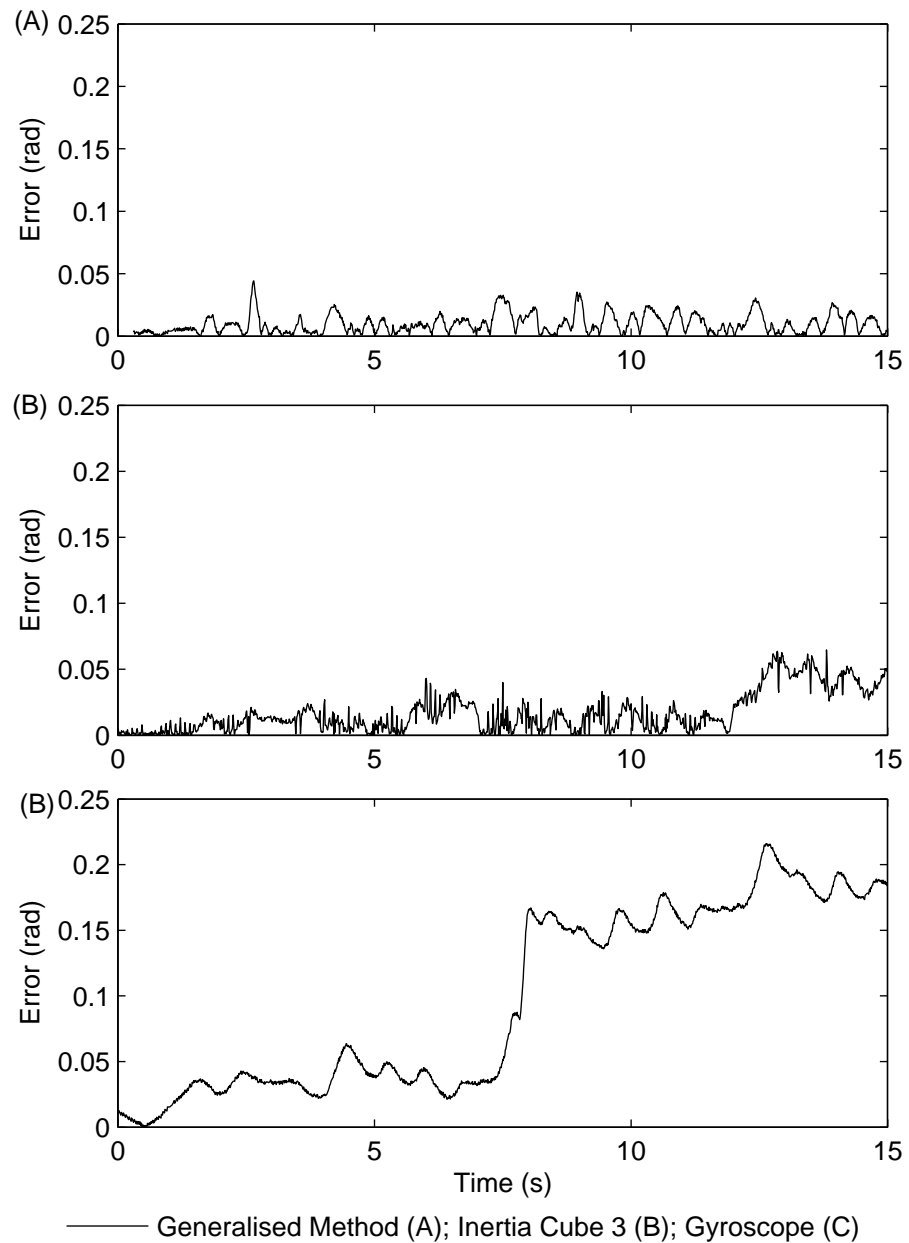


Figure 5.10: Absolute error in θ for the signal and solution methods of Figure 5.9. The Generalised Method (A), Inertia Cube 3 (B), and Gyroscope (C)

The generalised method is validated first using synthetic data, and compared to the previous methods in Figure 5.6. The comparison in Figure 5.6 shows improved performance in both accuracy and robustness to higher signal frequencies. Experimental comparisons to an Inertia Cube 3, MEMS gyroscope and optical encoder on the inverted pendulum, validate the new method, outperforming the other devices at frequencies below 2Hz, as seen in Figure 5.8. The typical absolute errors that occurred were in the order of 1.4%. At higher frequencies the method does not perform as well due to a low sampling rate, and increased model error and noise. Another advantage was illustrated for a longer more realistic signal in Figures 5.9 and 5.10, where the method is seen to be more robust in terms of drift, which the gyroscope, and at high frequencies, the Inertia Cube 3 can suffer from.

The results shown in Figures 5.8, 5.9 and 5.10 prove that tracking orientation using an accelerometer and model not only works but works well exceeding the performance of the other inertial orientations sensing devices. However, this proof is only achieved for the relatively simple case of a single degree of rotational freedom. The challenge addressed in the next chapter is whether this model can be further extended, by introducing additional dynamics.

Chapter 6

Extension to Full 2D Dynamics

Chapters 4 and 5 clearly showed that accurate orientation can be determined for a dynamic system using a non stationary accelerometer above a fixed centre of rotation. This proof of concept was derived for an inverted pendulum model of one degree of rotational freedom. Thus, the generalised method of Equations (5.8) – (5.34) can only be applied to applications with a fixed point of rotation.

However, for practical use in tracking head motion, other dynamics must be included in the methods. In this chapter, the model for one degree of rotational freedom described by Equations (2.1) and (2.2) is extended to include translation of the pivot point in the plane of motion. This motion would cover the practical case of tracking head motion for a walking individual. This extension is achieved through the inclusion of a second accelerometer measuring the translational acceleration and then applying an extended method, similar to the generalised method, to the effective relative acceleration at the end of the pendulum.

6.1 Extending the Model

The inverted pendulum model for head motion of Figure 2.1 and Equations (2.1) and (2.2) is extended by including translation of the pivot within the plane of motion. The schematic in Figure 2.1 is expanded in Figure 6.1 to include a second accelerometer, Accelerometer 2, with axes $A_{x,2}(t)$ and $A_{y,2}(t)$ at angle λ_2 to the horizontal axis, A_H . The accelerations, $A_h(t)$ and $A_v(t)$, which are due to the horizontal and vertical translational motion of the centre of rotation, are also included.

The first accelerometer, Accelerometer 1, is mounted at a point of radius R from the pivot on the pendulum. It has axes denoted $A_{x,1}(t)$ and $A_{y,1}(t)$. This accelerometer senses the combined acceleration due to both the rotation and the translation of the centre of rotation.

Although Accelerometer 2 is schematically shown in Figure 6.1 at the centre of rotation, this accelerometer can, in theory, be placed anywhere on the rigid body that supports the pendulum. This placement will provide the acceleration at the centre of rotation. Thus, for head tracking, this accelerometer can be placed at the centre of the back inline with the shoulders, within a tight fitting backpack containing other components of the wearable computing system required for AR systems.

The new model that extends Equations (2.1) – (2.2) is developed by resolving acceleration in terms of g along each respective axis, A_T , A_R , A_V , A_H in Figure 6.1. Note that the measured dynamic accelerations due to tangential, centripetal, A_v and A_h , will contribute in the opposite direction to that shown in Figure 6.1, as before. Also note that all accelerations and rotations ($\theta(t)$, $\dot{\theta}(t)$) remain functions of time. However, the “(t)” is dropped for clarity. Thus, including the additional A_h and A_v acceleration components along the A_T and A_R axes, and new expressions defining A_h and A_v along the A_V and A_H axes provides the extended model:

$$A_T = (R/g)\ddot{\theta} - \sin(\theta) - A_h \cos(\theta) - A_v \sin(\theta) \quad (6.1)$$

$$A_R = (R/g)\dot{\theta}^2 - \cos(\theta) + A_h \sin(\theta) - A_v \cos(\theta) \quad (6.2)$$

$$A_H = -A_h \quad (6.3)$$

$$A_V = -A_v - 1 \quad (6.4)$$

Equations (6.3) and (6.4) are limited to the case where λ_2 is constant in Figure 6.1. However, Equations (6.1) and (6.2) provide general model equations for any translation of the centre of rotation, provided that A_h and A_v can be measured. Thus, it is possible to extend this model to multiple inverted pendulum sections, with accelerometers placed at the pivots of each respective pendulum. These accelerometers provide the necessary A_h and A_v accelerations to determine the relative acceleration at the end of the each pendulum.

In this chapter, the extended model of Figure 6.1 with a constant λ_2 is used

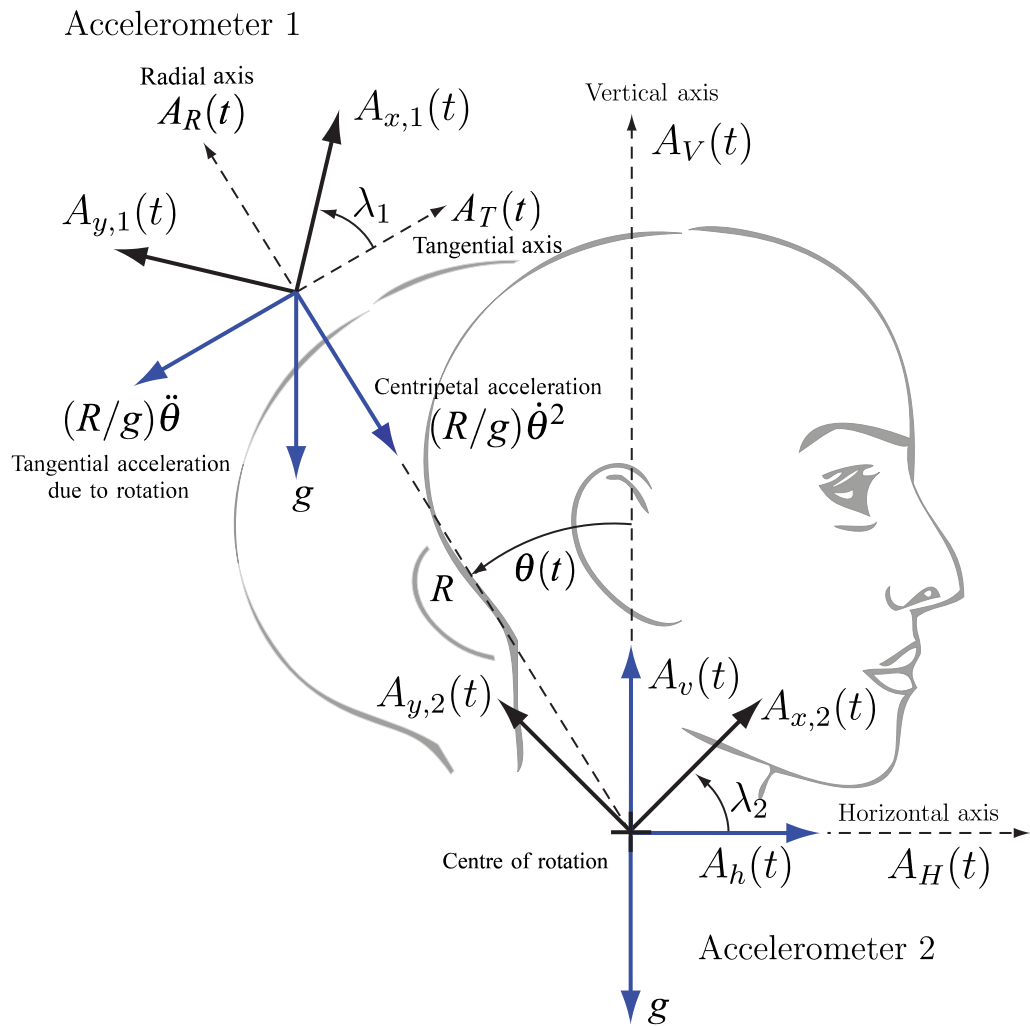


Figure 6.1: Schematic of the extended inverted pendulum model, including rotation and translation of the centre of rotation in a 2 dimensional plane

to prove the concept. Thus, the actual tangential (A_T), radial (A_R), vertical (A_V) and horizontal (A_H) accelerations are derived from the measured accelerations of Accelerometers 1 and 2 in the same way as Equations (2.3) and (2.4) and are defined:

$$A_T = A_{x,1} \cos(\lambda_1) - A_{y,1} \sin(\lambda_1) \quad (6.5)$$

$$A_R = A_{x,1} \sin(\lambda_1) + A_{y,1} \cos(\lambda_1) \quad (6.6)$$

$$A_H = A_{x,2} \cos(\lambda_2) - A_{y,2} \sin(\lambda_2) \quad (6.7)$$

$$A_V = A_{x,2} \sin(\lambda_2) + A_{y,2} \cos(\lambda_2) \quad (6.8)$$

A comparison of A_T and A_R from the model Equations (6.1) and (6.2) is made with the experimentally measured A_T and A_R of Equations (6.5) and (6.6) in Section 6.3.1 to verify that this extended model is valid.

6.2 Method

The method presented in this section extends the generalised method of Equations (5.8) – (5.34) and the piecewise method of Equations (4.14) – (4.25) to the extended model of Figure 6.1 for one degree of rotation and one degree of translation. Note that this method accurately determines the orientation θ in the presence of a disruptive translation to the centre of rotation. However, the method is not concerned with determining the translation itself.

The addition of translational motion to the pendulum pivot in the model introduces an $A_h \cos(\theta)$ and $A_v \sin(\theta)$ term to the tangential acceleration model Equation (6.1). The A_h and A_v parameters are found by rearranging Equations (6.3) and (6.4) in terms of the measured A_H and A_V :

$$A_h = -A_H \quad (6.9)$$

$$A_v = -A_V - 1 \quad (6.10)$$

where the parameters A_H and A_V are derived directly from the measured accelerations of Accelerometer 2 in Equations (6.7) and (6.8).

The same piecewise approach of the generalised method is applied to each individual time step, Δt , within this extended method. Thus, A_T is defined in Equations

(5.8) – (5.11). Similarly A_h and A_v are piecewise defined:

$$A_{h,fit} = \sum_{i=1}^k A_{h,fit,i} (H(t - t_i) - H(t - t_{i-1})) \quad (6.11)$$

$$A_{v,fit} = \sum_{i=1}^k A_{v,fit,i} (H(t - t_i) - H(t - t_{i-1})) \quad (6.12)$$

where H is the Heaviside function defined in Equation (5.9) and $A_{h,fit,i}$ and $A_{v,fit,i}$ define the linear expressions for A_h and A_v over the i th section:

$$A_{h,fit,i} = h_{1,i} + h_{2,i}t \quad i = 1, \dots, k \quad (6.13)$$

$$A_{v,fit,i} = v_{1,i} + v_{2,i}t \quad i = 1, \dots, k \quad (6.14)$$

where $h_{1,i}$, $h_{2,i}$ and $v_{1,i}$, $v_{2,i}$ are defined for Equations (6.13) (6.14) as follows:

$$\begin{aligned} h_{1,i} &= A_{h,i} - (i-1)(A_{h,i} - A_{h,i-1}) \\ h_{2,i} &= \frac{A_{h,i} - A_{h,i-1}}{\Delta t} \\ v_{1,i} &= A_{v,i} - (i-1)(A_{v,i} - A_{v,i-1}) \\ v_{2,i} &= \frac{A_{v,i} - A_{v,i-1}}{\Delta t} \end{aligned} \quad (6.15)$$

The trigonometric terms within Equation (6.1) are linearised in Equations (5.14) and (5.24) for $\sin(\theta)$ and $\cos(\theta)$ respectively. However, to improve robustness, and counter any increased noise in θ_{old} caused by the second accelerometer, the mean θ for each section, $\theta_{m,i}$, in Equations (5.15) and (5.25) is redefined:

$$\theta_{m,i} = \frac{1}{4} \sum_{i=i-2}^{i+1} \theta_i \quad i = 2, \dots, k-2 \quad (6.16)$$

$$\theta_{m,1} = \theta_{m,2} \quad (6.17)$$

$$\theta_{m,k-1} = \theta_{m,k-2} \quad (6.18)$$

$$\theta_{m,k} = \theta_{m,k-2} \quad (6.19)$$

Substituting the linear expressions for A_T , A_h , A_v , $\sin(\theta)$ and $\cos(\theta)$ from the respective Equations (5.10), (6.13), (6.14), (5.14) and (5.24), for the i th section,

into Equation (6.1) and collecting terms gives a linear, non homogeneous differential equation:

$$(R/g)\ddot{\theta} + E(t)\theta = F(t) \quad (6.20)$$

where:

$$\begin{aligned} E(t) &= E_{1,i} + E_{2,i}t & t_{i-1} \leq t \leq t_i \\ F(t) &= F_{1,i} + F_{2,i}t & t_{i-1} \leq t \leq t_i \quad i = 1, \dots, k \end{aligned} \quad (6.21)$$

and the linear coefficients $E_{1,i}$, $E_{2,i}$, $F_{1,i}$, and $F_{2,i}$ defined:

$$\begin{aligned} E_{1,i} &= -b_{2,i} - h_{1,i}c_{2,i} - v_{1,i}b_{2,i} \\ E_{2,i} &= -h_{2,i}c_{2,i} - v_{2,i}b_{2,i} \\ F_{1,i} &= u_{1,i} + b_{1,i} + h_{1,i}c_{1,i} + v_{1,i}b_{1,i} \\ F_{2,i} &= u_{2,i} + h_{2,i}c_{1,i} + v_{2,i}b_{1,i} \end{aligned} \quad (6.22)$$

Note that when the pivot of the pendulum is stationary, all $A_{h,i}$ and $A_{v,i}$ parameters are zero. Substituting $A_{h,i} = 0$ and $A_{v,i} = 0$ into Equations (6.20) – (6.22) reproduces the same set of ODEs defined in Equation (5.17) of the generalised method. For the case where the centre of rotation undergoes translation and $A_{h,i}$ and $A_{v,i}$ are no longer zero, the method becomes more advanced as described here.

An analytical solution to Equation (6.20) does not exist. However, an analytical solution does exist to the homogeneous equation, which is derived by setting $F(t) = 0$ in Equation (6.20). The resulting equation is defined:

$$(R/g)\ddot{\theta} + (E_{1,i} + E_{2,i}t)\theta = 0 \quad i = 1, \dots, k \quad (6.23)$$

The analytical solution to Equation (6.23) can be readily computed in Maple and is defined:

$$y_{c,i}(t) = C_1 \text{AiryAi}(M_i) + C_2 \text{AiryBi}(M_i) \quad i = 1, \dots, k \quad (6.24)$$

where:

$$M_i = \left(-\frac{E_{2,i}^{1/3}(E_{1,i} + E_{2,i}(t))}{E_{2,i}R^{1/3}} \right) \quad (6.25)$$

and *AiryAi* and *AiryBi* are wave functions related to Bessel functions and are built into both Maple and Matlab.

The standard solution to a linear non homogeneous ODE is a linear combination of the complementary and particular solutions. Following this standard theory, the solution is constructed as follows.

$$\theta_{sol,i} = y_{c,i}(t) + y_p(t) \quad i = 1, \dots, k \quad (6.26)$$

where $y_{c,i}(t)$ is the the complementary solution of Equation (6.23) and $y_p(t)$ is a particular solution to the linear ODE in Equation (6.20).

The complementary solution $y_{c,i}(t)$ in Equation (6.26) represents the transient response and only applies over i th section defined by the period $t_{i-1} < t < t_i$. The particular solution $y_p(t)$ is a numerical solution of the full linear ODE of Equation (6.20) with essentially arbitrary initial conditions. For simplicity, these initial conditions are set to zero.

In many engineering problems the particular solution $y_p(t)$ represents the steady state solution which is independent of the initial conditions. The problem as discussed in earlier chapters is that $y_p(t)$ is highly sensitive to initial conditions, as the transient solution $y_c(t)$ in Equation (6.26) does not die away. If the initial conditions for $\theta_{sol,i}$ are known very precisely there is no need for $y_{c,i}(t)$ in Equation (6.26). However, initial conditions are never known precisely in practice.

It is vital to separate the solutions $y_{c,i}(t)$ and $y_p(t)$ to accurately determine $\theta_{sol,i}$ in Equation (6.26). A further fundamental point is that the underlying differential equation must be linear to allow a solution of the form of Equation (6.26). This point emphasises the importance of the formulation of Equation (6.20) as no such construction can be applied to the full non linear model of Equations (6.1) and (6.2).

The analytical solution of $y_{c,i}(t)$ is substituted into Equation (6.26) and the solution arranged in terms of the unknown initial conditions, $\theta_{0,i}$ and $\dot{\theta}_{0,i}$. The expression is formed similarly to Equation (4.18) as:

$$\theta_{sol,i} = (\hat{A}_{1,i}\theta_{0,i} + \hat{A}_{2,i}\dot{\theta}_{0,i} + \hat{A}_{3,i})y_{1,i}(t) + (\hat{B}_{1,i}\theta_{0,i} + \hat{B}_{2,i}\dot{\theta}_{0,i} + \hat{B}_{3,i})y_{2,i}(t) + y_p(t) \quad (6.27)$$

where $y_{1,i}(t)$ and $y_{2,i}(t)$ are formed using the *AiryAi* and *AiryBi* basis functions:

$$y_{1,i}(t) = \text{AiryAi}(M_i) \quad (6.28)$$

$$y_{2,i}(t) = \text{AiryBi}(M_i) \quad (6.29)$$

where M_i defined in Equation (6.25). The parameters $\hat{A}_{1,i}$, $\hat{A}_{2,i}$, $\hat{A}_{3,i}$, $\hat{B}_{1,i}$, $\hat{B}_{2,i}$, $\hat{B}_{3,i}$, $\theta_{0,i}$, and $\dot{\theta}_{0,i}$ are defined recursively as follows:

$$\begin{aligned} \hat{A}_{1,i} &= \frac{\dot{y}_{2,i}(t_{i-1})}{y_{1,i}(t_{i-1})\dot{y}_{2,i}(t_{i-1}) - y_{1,i}(t_{i-1})y_{2,i}(t_{i-1})} \\ \hat{A}_{2,i} &= \frac{y_{2,i}(t_{i-1})}{y_{1,i}(t_{i-1})\dot{y}_{2,i}(t_{i-1}) - y_{1,i}(t_{i-1})y_{2,i}(t_{i-1})} \\ \hat{A}_{3,i} &= \frac{\dot{y}_{2,i}(t_{i-1})y_p(t_{i-1}) - y_{2,i}(t_{i-1})\dot{y}_p(t_{i-1})}{y_{1,i}(t_{i-1})\dot{y}_{2,i}(t_{i-1}) - y_{1,i}(t_{i-1})y_{2,i}(t_{i-1})} \\ \hat{B}_{1,i} &= \frac{\dot{y}_{1,i}(t_{i-1})}{y_{1,i}(t_{i-1})\dot{y}_{2,i}(t_{i-1}) - y_{1,i}(t_{i-1})y_{2,i}(t_{i-1})} \\ \hat{B}_{2,i} &= \frac{y_{1,i}(t_{i-1})}{y_{1,i}(t_{i-1})\dot{y}_{2,i}(t_{i-1}) - y_{1,i}(t_{i-1})y_{2,i}(t_{i-1})} \\ \hat{B}_{3,i} &= \frac{\dot{y}_{1,i}(t_{i-1})y_p(t_{i-1}) - y_{1,i}(t_{i-1})\dot{y}_p(t_{i-1})}{y_{1,i}(t_{i-1})\dot{y}_{2,i}(t_{i-1}) - y_{1,i}(t_{i-1})y_{2,i}(t_{i-1})} \\ \theta_{0,i} &= \theta_{sol,i-1}(t_{i-1}), \quad i \geq 2 \\ \dot{\theta}_{0,i} &= \dot{\theta}_{sol,i-1}(t_{i-1}), \quad i \geq 2 \\ \theta_{0,1} &= \theta_0 \\ \dot{\theta}_{0,1} &= \dot{\theta}_0 \end{aligned} \quad (6.30)$$

For given points t_0, \dots, t_k over the whole period ΔT , $\theta_{sol,i}$ can be summarised as follows:

$$\theta_{sol}(t) = \sum_{i=1}^k \theta_{sol,i}(t) (H(t - t_i) - H(t - t_{i-1})) \quad (6.31)$$

where H is the Heaviside function defined in Equation (5.9), and $\theta_{sol,i}$ is given in Equation (6.27).

To improve the robustness of the solution, given noisy accelerometer data for A_T , A_h , and A_v , used in forming the linear ODE, Equation (6.20), the solution period is increased from $\Delta T = 0.3\text{s}$ in the generalised method of Equations (5.8) – (5.34) to $\Delta T = 0.45\text{s}$. This extra data provides more information to fit to the model, and constrain the solution. The length of ΔT is limited by the size of the numeric solution $y_p(t)$ and the rounding issues this can introduce at very large values.

Another trade off of extending ΔT is that it reduces the responsiveness of the method to the last accelerometer measurements. In other words, finding the optimal initial conditions to minimise the objective function in Equation (5.29) over the whole period ΔT may not provide the optimal value for θ_{new} when the initial conditions are substituted into Equation (6.31). Thus, the objective function of Equation (5.29) is modified to optimise the fit to the radial acceleration over only the last $K = 30$ time points:

$$\hat{\Omega}(\theta_0, \dot{\theta}_0) = \sum_{i=0}^K \left(A_{R,sol}(t_k - i\Delta t) - A_R(t_k - i\Delta t) \right)^2 \quad (6.32)$$

where $A_{R,sol}$ is defined by Equations (5.27) and (5.28). Note that K in Equation (6.32) is less than k , which denotes the total number of sections within ΔT as illustrated in Figure 5.4.

Setting the gradient $\nabla_{\theta_0, \dot{\theta}_0} \hat{\Omega} = 0$ of Equation (6.32) yields:

$$\frac{\partial}{\partial \theta_0}(\hat{\Omega}) = 0 \quad (6.33)$$

$$\frac{\partial}{\partial \dot{\theta}_0}(\hat{\Omega}) = 0 \quad (6.34)$$

The solutions to Equations (6.33) and (6.34) correspond to the stationary points of the $\hat{\Omega}$ surface in Equation (6.32). The global minimum solution of Equations (6.33) and (6.34) corresponds to the optimum θ_0 and $\dot{\theta}_0$ and can be found using the method described in Equations (4.12) and (4.13), where C_1 and C_2 are replaced by θ_0 and $\dot{\theta}_0$. This method of selecting the optimal initial conditions was found to be more robust for the more complex surface generated by this extended method than the approximated surface method of Equations (5.32) – (5.34).

Finally, note that the actual ΔT value selected can be based on the dynamics of the system being measured, in this case head motion. It is also a compromise versus the lag induced and thus the AR or other system requirement. The overall point is that the algorithms are readily generalised to meet any specific application need.

6.3 Results and Discussion

6.3.1 Model Validation

The extended model of Equations (6.1) – (6.10) is verified in a similar fashion as that the initial model of Equations (2.1) – (2.2) in Section 2.3. Again, the inverted pendulum apparatus is used. However, unlike the initial model validation where the cart was clamped in place, for this case it is permitted to move.

Optical encoders provide an independent measure of rotation and horizontal cart position. Figures 6.2 and 6.3 show the accelerometers mounted on the apparatus. Note that the second accelerometer is mounted on the pendulum at the pivot, rather than on the cart. This placement is used because initial testing showed that when mounted on the cart significant noise was generated by the cart motion on the track due to un-modelled dynamics resulting from slack within the pivot bearing arrangement and a rough guide track

The parameters A_H and A_V of Figure 6.1 are derived from the second accelerometer on the pendulum using the known encoder measurement of rotation, θ_{en} :

$$A_H = A_{x,2} \cos(\theta_{en} + \lambda_{2a}) - A_{y,2} \sin(\theta_{en} + \lambda_{2a}) \quad (6.35)$$

$$A_V = A_{x,2} \sin(\theta_{en} + \lambda_{2a}) + A_{y,2} \cos(\theta_{en} + \lambda_{2a}) \quad (6.36)$$

where λ_{2a} is the fixed angle the accelerometer x axis makes with the pendulum, similar to λ_1 for Accelerometer 1. Thus, the required accelerations for the centre of rotation of the pendulum are found without the need to fix the inadequacies of the experimental apparatus to prove the method.

An experiment was undertaken that captured measurements from the two calibrated accelerometers, a gyroscope, and an Inertia Cube 3. The accelerometers were calibrated using the procedure described in Section 2.2.3 and the Inertia Cube 3 was used with zero heading and enhancement set to option 2, as before in Section 5.2.2. These devices can be seen in the apparatus set up shown in Figures 5.7, 6.2 and 6.3.

The experimental measurements were collected while manually moving both the

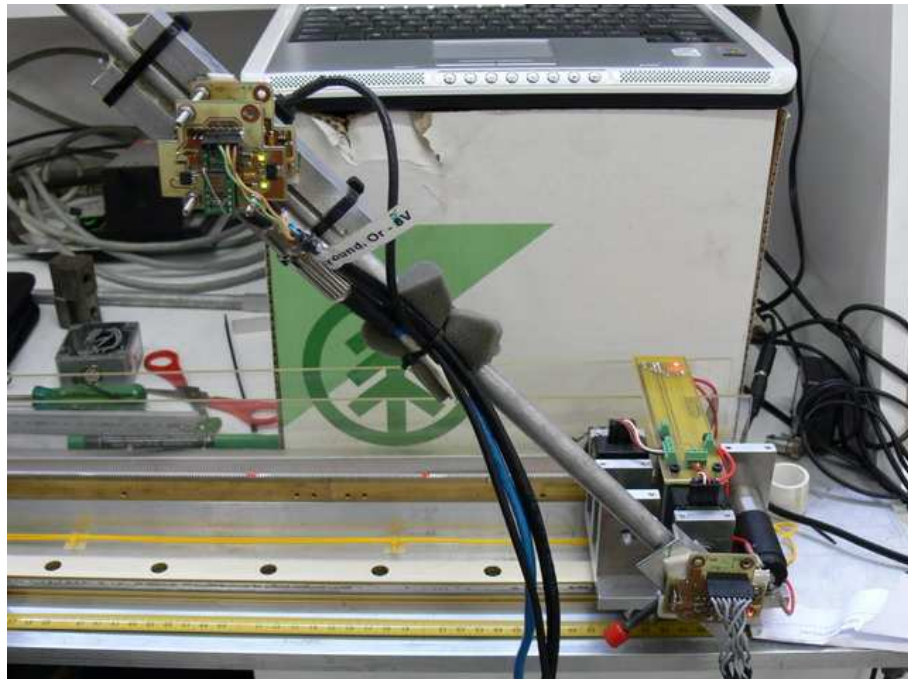


Figure 6.2: The inverted pendulum apparatus with two accelerometers attached and cart free to move, also attached is the Inertia Cube 3 and gyroscope

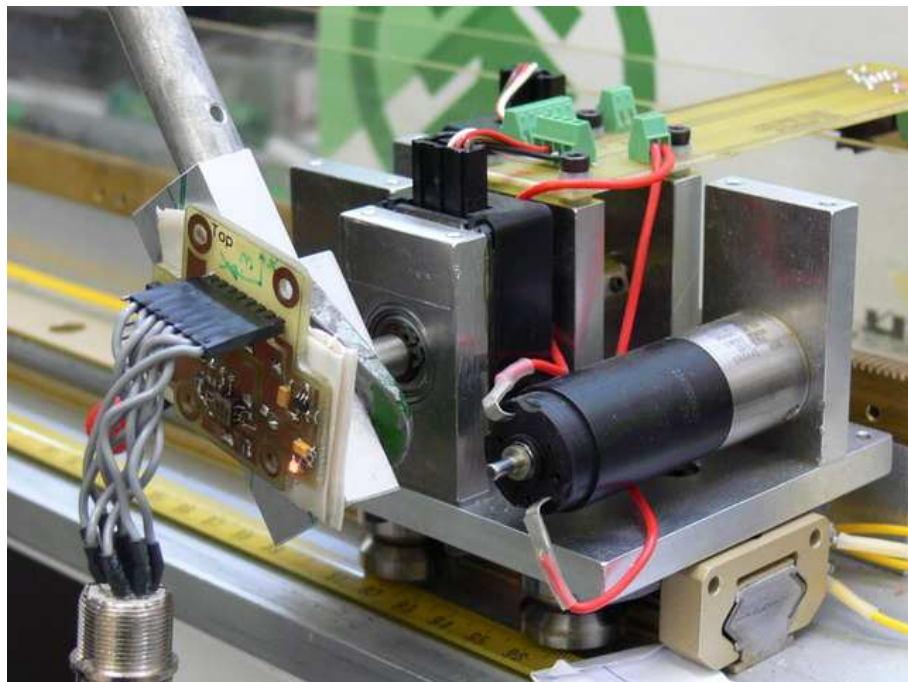


Figure 6.3: Close up view of cart system of the inverted pendulum with Accelerometer 2 mounted on the pendulum, at the centre of rotation in this case

cart and pendulum. Figure 6.4 shows the cart displacement and total acceleration, A_H and A_V , for a 10 second period of motion. The cart displacement of approximately 15cm is measured using the optical encoder attached to the cart running to the track, and A_H and A_V are derived from Accelerometer 2 measurement in Equations (6.35) and (6.36).

The measured A_H and A_V of Figure 6.4 are filtered and substituted into Equations (6.9) and (6.10) to find the accelerations A_h and A_v that are due to only the motion of the cart. The values for A_h and A_v along with θ_{en} , can be substituted into the model Equations (6.1) and (6.2) to generate values for A_T and A_R . Figure 6.5 shows the comparison of A_T and A_R derived from the model Equations (6.1) and (6.2) with the measured values from Accelerometer 1 in Figure 6.1 and Equations (6.5) and (6.6).

The quality of the fit for the experimentally measured data to the model is summarised in by the mean, standard deviation, and mean percentage of the absolute error in Table 6.1. These results show a good general fit to A_T with 4.6% mean absolute error. However, A_R suffers from poor signal quality when near vertical giving 20.7% mean absolute error. These values compare well to the respective mean absolute error percentages of 5.4% and 21.9% for A_T and A_R from the previous model validation when the cart was fixed, summarised in Table 2.3.

Table 6.1: Acceleration model error

Error Measure	Acceleration	
	A_R (mg)	A_T (mg)
Mean	3.1	9.3
STD	3.0	7.3
Mean %	20.7	4.6

The measured acceleration results remain a good fit to the model, despite the increased noise caused by the cart motion on the track. This noise is much higher than would be expected during head tracking. However, because the method utilises the acceleration for the top accelerometer relative to the bottom, motion experienced by both accelerometers is effectively removed from the model. These results confirm the validity of the model to this experimental set up.

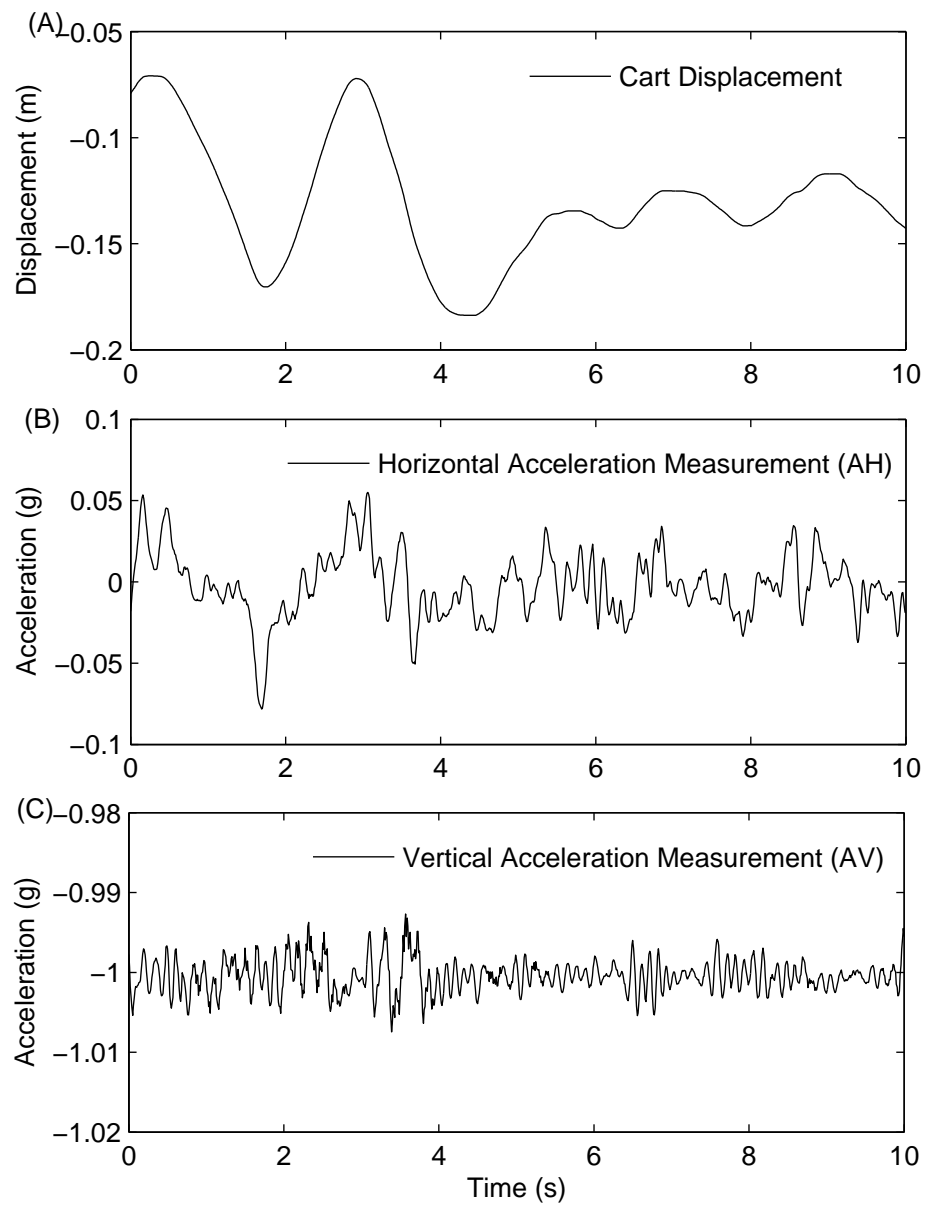


Figure 6.4: Cart displacement and total acceleration: (A) Measured displacement via cart encoder; (B) Measured horizontal acceleration, A_H , via Accelerometer 2 and Equation (6.35); (C) Measured vertical acceleration, A_V , via Accelerometer 2 and Equation (6.36)

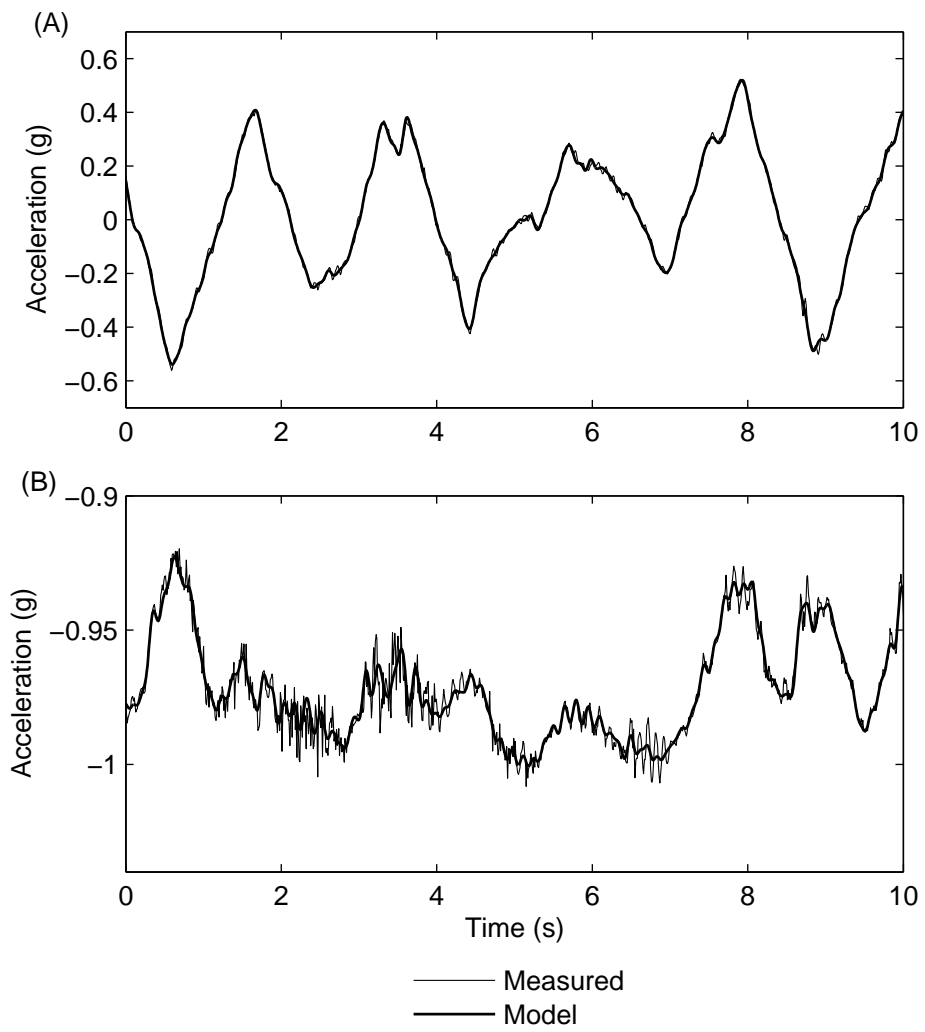


Figure 6.5: Measured and model accelerations: (A) Tangential acceleration, A_T ; (B) Radial acceleration, A_R

6.3.2 Experimental Results and Comparisons

The extended method of Equations (6.9) – (6.34) is used to solve for orientation for a case of full two dimensional translation and rotation. The same data from the model validation of Section 6.3.1 is used. More specifically, the unfiltered measured signals of A_H and A_V seen in Figure 6.4 (B) and (C) derived from Accelerometer 2, and A_T and A_R seen in Figure 6.5 from Accelerometer 1. The method is applied over the 10 second, 100Hz sampled signal with the period in the algorithm set to $\Delta T = 0.45s$, and a shorter fit period of the last 0.3s to the measured A_R defined by setting $K = 30$ in Equation (6.32).

The extended method results are compared to the results from the Inertia Cube 3 and gyroscope, similar to the generalised method validation in Chapter 5. Results are shown for each method or device in Figure 6.6 with the corresponding absolute error plotted in Figure 6.7. These results are summarised by the metrics describing the absolute error in Table 6.2.

Table 6.2: Extended method experimental error results for the 10 second signal

Device/Method	Max (deg)	STD (deg)	Mean (deg)	%
Extended Method	1.63	0.30	0.36	3.82
Inertia Cube 3	1.62	0.41	0.61	6.58
Gyroscope	3.24	0.79	1.08	11.06

The extended method performs better than the Inertia Cube 3 and gyroscope for this signal. More specifically, a mean absolute percentage error of 3.82% is achieved, compared with 6.58% and 11.06% for the Inertia Cube 3 and gyroscope respectively. However, the resulting signal is not as smooth as was the case for pure rotation seen in Figure 5.9. This increased noise within the solution can be attributed to the, now three, linear fits to noisy acceleration signals A_T , A_h , and A_v , within the linearised model Equation (6.20). Solving over a longer period $\Delta T = 45$ does reduce these aberrations. However, increasing this time period further does not continue this improved trend, and merely increases computation and potential lag.

Further comparison with the results in Table 5.2 for the pure rotation case shows that, even with the less dynamic signal of Figure 6.6 (compared to Figure 5.9), the accuracy attained by the generalised method for the stationary cart achieves a lower mean absolute percentage error of 2.61% compared to 3.82% for the moving cart.

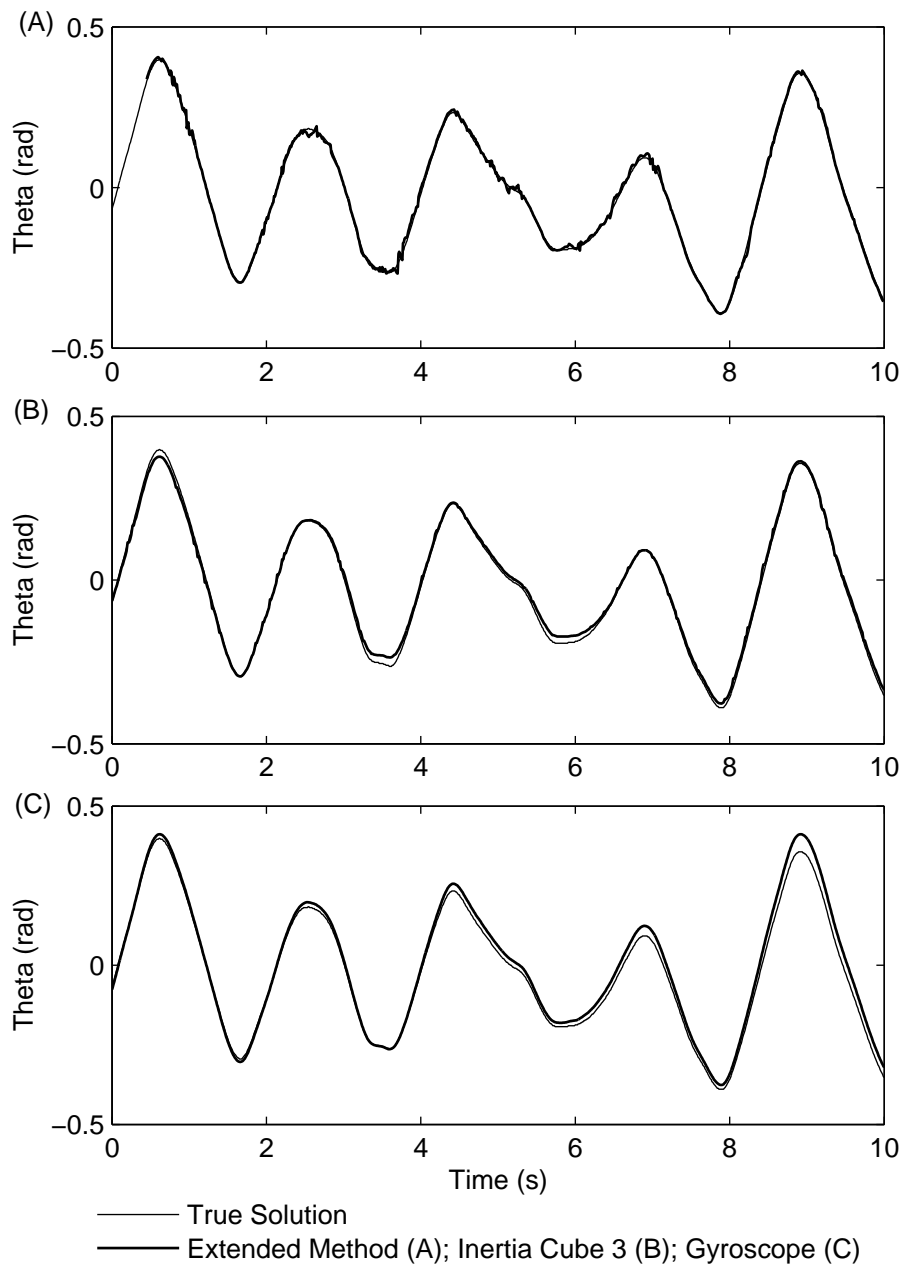


Figure 6.6: Experimental comparisons to determining orientation, θ , using the Extended Method (A), Inertia Cube 3 (B), and Gyroscope (C)

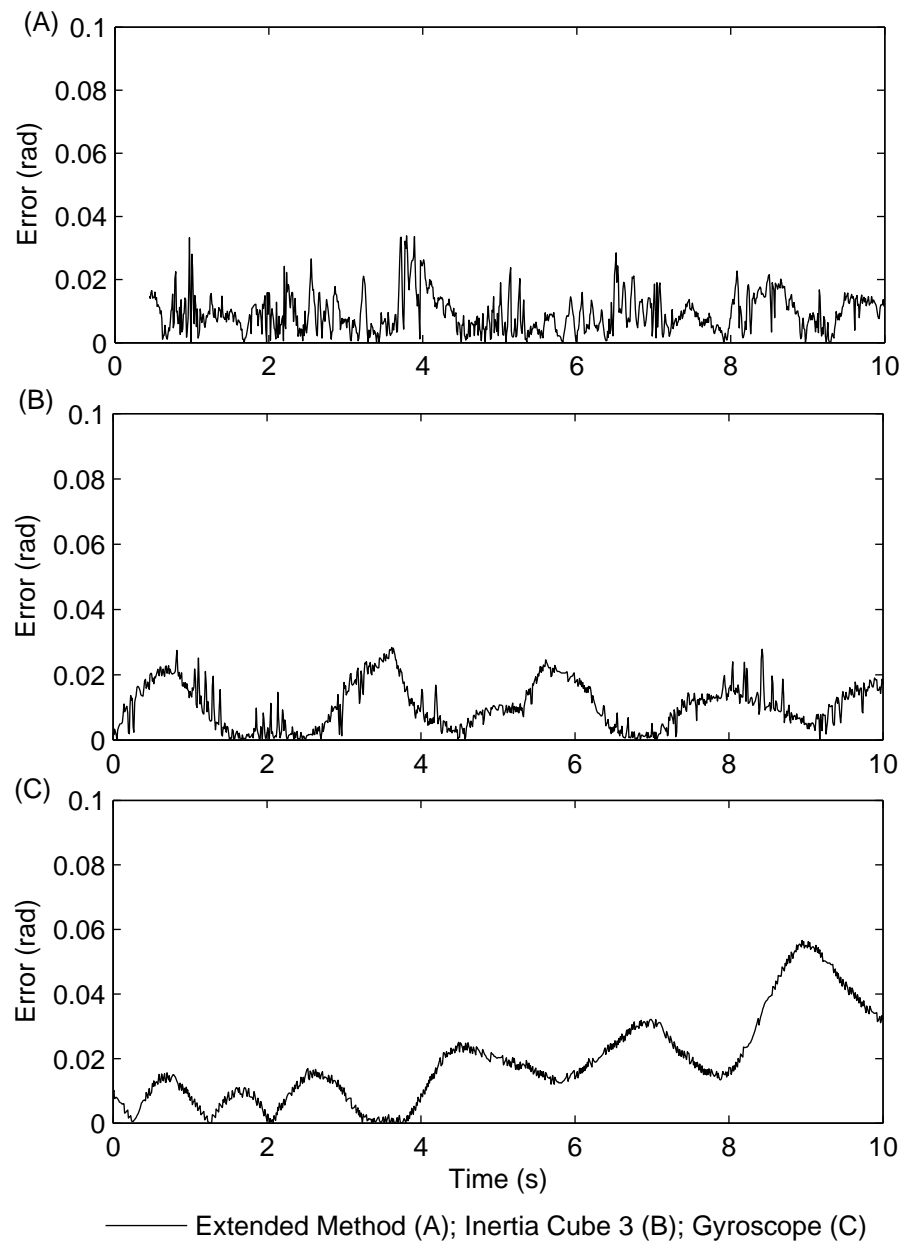


Figure 6.7: Absolute error in θ for the signal and solution methods of Figure 6.6. The Extended Method (A), Inertia Cube 3 (B), and Gyroscope (C)

However, this result is expected given the added complexity and room for error within the extended method.

The Inertia Cube 3 performs similarly for both cases with approximately double the error of the generalised and extended methods. The gyroscope appears to perform better within these results. However, this result is simply explained by the shorter signal used in this case not allowing as much time for its result to drift.

6.4 Summary

The generalised method of Equations (4.14) – (4.25) presented in Chapter 5 is limited to finding orientation for a case of one degree of rotational freedom. For head tracking, other dynamics due to motion of the user would clearly corrupt the accelerometer signals due to rotation alone. The inverted pendulum model of Figure 2.1 and Equations (2.1) and (2.2) solved in the generalised method is extended to include motion of the pivot. The resulting accelerations from this motion, A_h and A_v , are used to generate new model Equations (6.1) and (6.2) for the relative tangential and radial accelerations at the end of the inverted pendulum.

The generalised method of Equations (4.14) – (4.25) is modified to generate a solution to the new model Equations (6.1) and (6.2). The linearised tangential Equation (6.20) unfortunately does not have an analytical solution. Thus, this new extended method of Equations (6.9) – (6.34) presented, utilises the analytical homogeneous solution, combined with the numerical solution, to form the solution θ_{sol} in terms of unknown initial conditions θ_0 and $\dot{\theta}_0$.

Both the model of Equations (6.1) and (6.2) and the extended method for the solution of θ from Equations (6.9) – (6.34) were validated experimentally. This validation was achieved by moving both the cart and pendulum of the inverted pendulum apparatus, with accelerometers measuring A_T , A_R , A_h , and A_v . The fit of the measured accelerations A_T and A_R to the model Equations (6.1) and (6.2) shows good agreement, as seen in Figure 6.5, similar to the initial validation for the fixed pivot system in Section 2.3.

The extended method was also compared to the Inertia Cube 3 and Analogue Devices gyroscope in Figures 6.6 and 5.10. The extended method, although not as

accurate as it was for the stationary cart, still outperforms the other devices. In particular it achieves a mean absolute percentage error of 3.82% over the 10 second signal tested.

The extended method of Equations (6.9) – (6.34) presented in this chapter clearly shows that accurate orientation can be determined for the inverted pendulum model of head motion while undergoing dynamic rotation and translation of the pivot in a single vertical plane. This case and method cover a far more general scenario than a single rotational degree of freedom case. It, also provides an approach that can be readily generalised to other vertical head motion planes.

Chapter 7

Conclusions

Achieving precise and accurate image registration is one of the most significant unsolved problems within AR systems, particularly under any significant speed or frequency of motion. As a result, registration error is a major issue hindering the more widespread growth of AR applications. Overcoming the challenges that accurate viewpoint tracking presents within AR systems will improve performance for existing applications, and enable new AR development.

Many tracking methods exist, although typically these perform relatively poorly or are unsuitable in highly dynamic environments that many AR applications seek to expand into. Thus, applications in these more challenging environments, such as outdoors, are not well catered for by existing commercial tracking solutions. To fully enable AR growth, accurate but, low cost approaches based on simple, existing sensor platform technologies are required.

7.1 Objectives and Approach

The key objective for this thesis was to improve dynamic orientation tracking of the head using low cost inertial sensors. The approach taken was to extend the excellent static orientation sensing abilities of accelerometers to a dynamic case by utilising a model of head motion. Other approaches to sensing dynamic orientations using inertial devices rely heavily on rate gyroscopes. However, these gyroscopes suffer from inherent drift due to the required integration of noisy rotational rate measurements to determine orientation. These approaches then apply methods that intermittently correct for the drift, often utilising accelerometers. Generally devices

using these approaches produce good results for relatively slow or lower frequency motions. However, their performance drops significantly during motions with faster dynamics due to the inability to accurately correct for drift in these situations. Thus, they cannot address the needs of emerging AR application spaces.

The approach presented in this thesis is restricted to motion in a vertical plane. Thus, applying to pitch and roll orientations of head motion. Importantly, it is these orientations that are most perturbed during walking or running. The relatively simple model-based sensor approach developed to represent head motion is based on an inverted pendulum with a dual axis accelerometer attached in the plane of motion. This positioning corresponds to attaching the accelerometer to a helmet or other type of head gear, as is the case with existing inertial orientation devices.

Initially, the case of a single degree of rotational freedom is considered. ODEs describing the rotational motion of the pendulum were formed by resolving the tangential and radial accelerations at the point that the accelerometer is attached to the pendulum. These model equations, proved difficult and unstable to solve, with conventional engineering approaches and other initial methods failing to produce stable solutions for orientation. Although it is a well defined model, solving the equations for orientation is not typical, and no stable solution over any useful time period was found in the literature. The analytical solution to the linear tangential ODE illustrated that the instability present in the solutions is due to the presence of a positive exponential power in the transient solution. This solution is essentially ill-conditioned with any error in the initial conditions, leading to error in the coefficient of the exponential terms, resulting in instability. As a result, novel methods are required to develop the solutions in a stable and accurate form.

7.2 The Unique Solution Method

A unique mathematical approach to solving the model equations simultaneously to give orientation was presented. This method is based around constructing a linear piecewise approximation to the non linear tangential ODE. The first piecewise section is solved in terms of unknown initial conditions. Each subsequent piecewise section has its initial conditions defined by the solution of the previous section, represented in terms of the original unknown initial conditions from the beginning

of the period. Thus, a piecewise analytical solution is achieved in terms of unknown initial conditions that approximates the solution to the non linear tangential ODE.

This approximate solution for orientation is then substituted into the independent radial ODE and the unknown initial conditions optimised by fitting the generated expression to the measured radial acceleration. The optimal initial conditions are then substituted into the solution of the tangential ODE providing orientation. Thus, the method effectively allows a solution to a nonlinear ODE to be generated in terms of unknown initial conditions, that are then optimally determined from a second independent ODE.

This unique approach overcomes the instability and ill-conditioning that resulted in all other attempted solution methods applied to the model equations failing. This important result forms the significant contribution of this thesis. The method provides a means to a solution for a coupled set of unstable independent nonlinear ODEs that are not solvable by any other conventional method. This method, or parts of the method, may well find useful application within other research areas. However, more specifically, this thesis presents the stable and accurate solution for orientation from the inverted pendulum model equations, not found within the literature over any significant time period. This result alone could prove useful in areas involving other physiological measures and studies where the inverted pendulum model is often applied, or other similar inherently or innately unstable systems.

7.3 Validation of the Methods

The methods were validated experimentally with data collected using accelerometers and an inverted pendulum apparatus over a range frequencies from 0 – 3Hz, typical for pitch and roll head motions. For a fixed cart the best method developed achieved absolute percentage errors of approximately 1.4% for signal frequencies of 1Hz or less. Higher frequencies resulted in a reduction in performance. However, increasing the sampling rate should dramatically reduce this effect.

The extended method operates on the acceleration of the pendulum relative to the centre of rotation. Thus, this method relies on a second accelerometer to measure the acceleration at the centre of rotation. Initial validation of the extended method achieved by moving the cart and pendulum shows a reduction in performance from

an absolute percentage error of 2.61% for the stationary cart to 3.82% for the moving cart over the signals tested. This is not surprising given that the relative acceleration would effectively double the noise present.

Within these limited two dimensional validation tests, the accelerometer model-based method outperforms the Inertia Cube 3, the best existing multi-sensor platform solution, with the results approximately half the mean absolute percentage error of the Inertia Cube 3 results for frequencies less than 2Hz. The gyroscope performs relatively well over such short signal lengths. However, as expected drifts significantly over longer periods.

The key advantage of the accelerometer model-based method presented within this thesis is that the orientation solution remains registered to the gravitational vector at all times as described by the model equations. Thus, this method is immune to drift that can be observed at high frequencies with the Inertia Cube 3 and clearly with gyroscope based solutions, and does not need to rely on any other sensing modality.

7.4 Potential Application Benefits

The accelerometer model-based method presented within this thesis proves the concept, in two dimensions, that accelerometers combined with an accurate motion model can accurately determine orientation within a dynamic system. Theoretically, this two dimensional model can easily be extended to the more general three dimensional case. Hence, it can be readily applied to head tracking within AR applications. The same advantages of this method apply in the three dimensional case as applied in the two dimensions examined here.

The accurate performance demonstrated by the method in two dimensions will be maintained given that the relationship of the accelerometer axes to gravity described in the the model equations still holds. Increasing sampling rate within the method will improve the dynamic performance, providing more data points to describe the measured acceleration signals. Real-time application of the methods presents no significant challenge given an increase in speed of 100 to 1000 times is typically attained for optimised code running on a digital signal processor (DSP). Therefore, the objective of improving the dynamic performance of head tracking for

AR applications can be realistically expected to be achieved.

The accuracy of the methods presented still remain far from the ideal performance of 0.0057° suggested in the literature which is a very challenging requirement. This value is suggested as a target to achieve a resultant 1mm registration error with all error sources and delays are included within the AR system. These levels are unattainable with the current inertial MEMS technology. Importantly, the method presented is independent of any specific hardware.

However, this ideal accuracy noted is not required for all applications. Assuming similar results to those presented in the validation of the methods for the two dimensional system will be achieved in the three dimensional system, then these methods would mark a very significant improvement in the state of the art. In particular, they are almost twice as good as a leading commercial MEMS based IMU, the Inertia Cube 3, which costs in the order of US\$1000.

7.5 Summary

A robust method to determine pitch or roll orientation for highly dynamic head motion was developed, based on an inverted pendulum model of head motion, and accelerometer measurements. A unique approach is required, and was developed, to solve the unstable coupled set of differential model equations. The key advantage of this accelerometer model-based method is that the orientation remains registered to the gravitational vector, providing a drift free solution that outperforms existing, state of the art, gyroscope based methods. This proof of concept uses low-cost accelerometer sensors to show significant potential to improve head tracking in dynamic AR environments, such as outdoors.

Chapter 8

Future Work

The model-based methods for tracking orientation presented offer significant, stable and accurate improvements over the state of the art. However, there are still several avenues of potential improvement that have arisen in the latter course of this work. These directions and possibilities are outlined in this chapter.

8.1 Further Validation Methods

The extended method of Equations (6.9) – (6.34), presented in Chapter 6, was validated experimentally using the inverted pendulum apparatus. However, due to slack within the pivot bearing mechanism, and the relatively large noise induced by the motion of the cart along the track, Accelerometer 2 of Figure 6.1 was actually placed upon the pendulum at the centre of rotation. The values for the measured A_h and A_v , required to determine the relative acceleration were then derived using the measured θ_{en} from the encoder. Modifications to the apparatus would rectify these issues and allow the second accelerometer to be placed more realistically upon the cart, and the extended method more successfully implemented.

8.1.1 Using the Method in a Nested Approach

A further extension and validation of the extended method in two dimensions would illustrate the application within a nested approach. This implementation would determine the orientation of the second pendulum in a double pendulum system, as shown schematically in Figure 8.1. The determination of the orientation of the

first pendulum section would be required to find A_h and A_v for the second system. Thus, the extended method is radially extensible to more complex systems. Such an array of accelerometers could be positioned in a wearable computing system, for example, on the hips, shoulders, and head, to provide orientation for total human body motion.

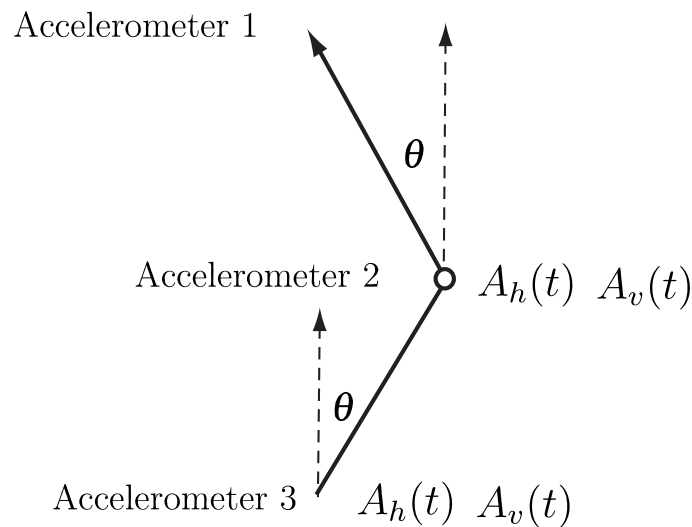


Figure 8.1: The nested system for two pendulum sections

This extended physical approach could be easily experimentally verified using an extended inverted pendulum apparatus, with optical encoders providing the true orientation for the system for comparison.

8.1.2 Controlling the Inverted Pendulum

To validate the approach presented in the extended method, the solution for orientation of the pendulum could be implemented within a control system to stabilise the inverted pendulum in real time. The successful implementation of such an approach would provide undisputable validation of the accuracy and real time application of the orientation result from the method. As such it presents a difficult, but well known, benchmark problem for the results developed here.

8.1.3 Head Motion Validation

The validation approaches applied here do not specifically validate the method for actual head motion. Given that improving dynamic head tracking is the ultimate, and intended application of this work, it is important to validate the method specifically for this case. Such validation requires a highly accurate and independent measure of head orientation. An infra-red optical tracking system, as introduced in Section 1.4, should provide a good measure of truth for such validation. However, it is expected that better performance will be achieved from the method for this case when implemented in three dimensions. This expectation exists because unmodelled out of plane disturbances will have a detrimental effect on the performance of the method in any given two dimensional plane and it would be very difficult to implement and capture head motion data without inducing such effects.

8.2 Extensions of the Methods and Algorithms

8.2.1 Extension to Three Dimensional Motion

The methods developed and provisionally validated within this thesis are based on proving the concept that using accelerometers combined with a model can provide accurate orientation that is immune to drift. Now that this concept has been initially validated, the method and approach can be extended to three dimensions, providing a robust solution for tracking pitch and roll head orientations within highly dynamic AR applications that motivated this work.

8.2.2 Integrating a Gyroscope into the Methods

The approach presented in this thesis utilises only accelerometers, combined with a model of the motion. However, this work approaches the limits of the accuracy attainable with only accelerometers due to noise and model error. Accelerometers have the advantage that they sense the gravitational acceleration. This gravitational acceleration provides reference for accelerations from resulting orientations. However, rate gyroscopes sense rotational rate, which, upon integration, yields ori-

entation. This orientation result is unreferenced and suffers from considerable drift, but is generally quite smooth.

Introducing a gyroscope to the method offers significant synergies. The accelerometer model-based method will provide stability to the drift prone gyroscope over the medium and long term. Conversely, the gyroscope can provide stability to the accelerometer method over the short term providing additional robustness to this method with respect to noise and un-modelled disturbances. This combination has more potential for an improved result than other approaches that simply correct the drift of the gyroscope sporadically.

The inclusion of the gyroscope within the method could also result in a significant computational saving. As the gyroscope directly measures $\dot{\theta}$, the radial equation used to optimise the initial conditions by fitting to the measured A_R becomes linear in θ . Thus, the surface describing the optimal θ_0 and $\dot{\theta}_0$ only has one solution, making a solution much simpler and faster.

Thus, combining a gyroscope into the new methods developed in this thesis effectively provides dynamic drift correction applied at every measurement time point. This combination could potentially provide a significant improvement in the solution for θ , by as much as 10 times. This new result would be much closer to the ideal performance suggested to achieve 1mm registration error within an AR system that is provided in Table 2.1. It would also even more significantly outperform current multi-sensor platforms like the Inertia Cube 3 due to the major advantages captured by the methods developed in this thesis.

8.2.3 Investigate and Implement Prediction

Prediction, discussed in Section 1.5.1, is an approach to reduce dynamic registration error caused by latency within and AR system. The application of more accurate head motion models, such as the inverted pendulum model presented and solved within this thesis, offer potential to improve the performance of the prediction. Improved prediction performance, would result in an increased feasible prediction interval, as well as a more accurate estimate. Thus, to some extent negating the effect the latency has on the registered image within an AR application.

Appendix A

Full Solution to the Generalised Approach

In this appendix the solution to Equation (5.17) of the generalised method is constructed in terms of the initial conditions θ_0 and $\dot{\theta}_0$ independently from the solution in of the piecewise method of Equations (4.18) – (4.25) which are in terms of C_1 and C_2 . Solving the linear Equation (5.17) gives the analytical expression:

$$\theta_{sol,i} = (\bar{A}_{1,i}\theta_0 + \bar{A}_{2,i}\dot{\theta}_0 + \bar{A}_{3,i})\mathbf{e}^{m_i(t-t_{i-1})} + (\bar{B}_{1,i}\theta_0 + \bar{B}_{2,i}\dot{\theta}_0 + \bar{B}_{3,i})\mathbf{e}^{-m_i(t-t_{i-1})} - \frac{(b_{1,i} + u_{1,i} + u_{2,i}t)}{b_{2,i}} \quad (\text{A.1})$$

which has a differential of:

$$\dot{\theta}_{sol,i} = m_i(\bar{A}_{1,i}\theta_0 + \bar{A}_{2,i}\dot{\theta}_0 + \bar{A}_{3,i})\mathbf{e}^{m_i(t-t_{i-1})} - m_i(\bar{B}_{1,i}\theta_0 + \bar{B}_{2,i}\dot{\theta}_0 + \bar{B}_{3,i})\mathbf{e}^{-m_i(t-t_{i-1})} - \frac{u_{2,i}}{b_{2,i}} \quad (\text{A.2})$$

where for both Equations (A.1) and (A.2) the following variables are redefined:

$$\begin{aligned}
t_i &= i\delta t \\
m_i &= \frac{(b_{2,i}g)^{1/2}}{R^{1/2}} \\
\bar{A}_{1,i} &= \frac{(b_{2,i}g)^{1/2}q_{1,i} + dq_{1,i}R^{1/2}}{2(b_{2,i}g)^{1/2}} \\
\bar{A}_{2,i} &= \frac{(b_{2,i}g)^{1/2}q_{2,i} + dq_{2,i}R^{1/2}}{2(b_{2,i}g)^{1/2}} \\
\bar{A}_{3,i} &= \frac{(b_{2,i}g)^{1/2}(b_{1,i} + u_{1,i} + u_{2,i}t_{i-1}) + u_{2,i}R^{1/2} + b_{2,i}^{3/2}g^{1/2}q_{3,i} + dq_{3,i}R^{1/2}b_{2,i}}{2b_{2,i}^{3/2}g^{1/2}} \\
\bar{B}_{1,i} &= \frac{(b_{2,i}g)^{1/2}q_{1,i} - dq_{1,i}R^{1/2}}{2(b_{2,i}g)^{1/2}} \\
\bar{B}_{2,i} &= \frac{(b_{2,i}g)^{1/2}q_{2,i} - dq_{2,i}R^{1/2}}{2(b_{2,i}g)^{1/2}} \\
\bar{B}_{3,i} &= \frac{(b_{2,i}g)^{1/2}(b_{1,i} + u_{1,i} + u_{2,i}t_{i-1}) - u_{2,i}R^{1/2} + b_{2,i}^{3/2}g^{1/2}q_{3,i} - dq_{3,i}R^{1/2}b_{2,i}}{2b_{2,i}^{3/2}g^{1/2}}
\end{aligned}$$

where the $q_{1,i}$, $q_{2,i}$, $q_{3,i}$ and $dq_{1,i}$, $dq_{2,i}$, $dq_{3,i}$ terms define the initial conditions at t_{i-1} for the i th section in terms of the initial conditions at t_0 , θ_0 and $\dot{\theta}_0$. Continuity is maintained as before, with these constants representing the coefficients of θ_0 and $\dot{\theta}_0$ within the solution, evaluated at the end of the previous section. This definition is shown in Equation (A.3).

$$\begin{aligned}
\theta_{sol,i}(t_{i-1}) &= \theta_{sol,i-1}(t_{i-1}) = q_{1,i}\theta_0 + q_{2,i}\dot{\theta}_0 + q_{3,i} \\
\dot{\theta}_{sol,i}(t_{i-1}) &= \dot{\theta}_{sol,i-1}(t_{i-1}) = dq_{1,i}\theta_0 + dq_{2,i}\dot{\theta}_0 + dq_{3,i} \quad i = 2, \dots, k \quad (A.3)
\end{aligned}$$

However, at t_0 the initial conditions are already defined. Thus, for the case where $i = 1$, $q_{1,i}$, $q_{2,i}$, $q_{3,i}$ and $dq_{1,i}$, $dq_{2,i}$, $dq_{3,i}$ are defined such that:

$$\begin{aligned}
\theta_{sol,1}(0) &= \theta_0 \\
\dot{\theta}_{sol,1}(0) &= \dot{\theta}_0 \quad (A.4)
\end{aligned}$$

giving:

$$\begin{aligned}
q_{1,i} &= 1 & dq_{1,i} &= 0 \\
q_{2,i} &= 0 & dq_{2,i} &= 1 \\
q_{3,i} &= 0 & dq_{3,i} &= 0
\end{aligned}
\qquad i = 1 \qquad (\text{A.5})$$

Beyond the first section, $q_{1,i}$, $q_{2,i}$, $q_{3,i}$ and $dq_{1,i}$, $dq_{2,i}$, $dq_{3,i}$ are defined by recursive expressions where:

$$\begin{aligned}
q_{1,i} &= \bar{A}_{1,i-1} \mathbf{e}^{m_{i-1}(t_{i-1}-t_{i-2})} + \bar{B}_{1,i-1} \mathbf{e}^{-m_{i-1}(t_{i-1}-t_{i-2})} \\
q_{2,i} &= \bar{A}_{2,i-1} \mathbf{e}^{m_{i-1}(t_{i-1}-t_{i-2})} + \bar{B}_{2,i-1} \mathbf{e}^{-m_{i-1}(t_{i-1}-t_{i-2})} \\
q_{3,i} &= \bar{A}_{3,i-1} \mathbf{e}^{m_{i-1}(t_{i-1}-t_{i-2})} + \bar{B}_{3,i-1} \mathbf{e}^{-m_{i-1}(t_{i-1}-t_{i-2})} - \frac{(b_{1,i-1} + u_{1,i-1} + u_{2,i-1}t_{i-1})}{b_{2,i-1}} \\
dq_{1,i} &= m_{i-1} \bar{A}_{1,i-1} \mathbf{e}^{m_{i-1}(t_{i-1}-t_{i-2})} - m_{i-1} \bar{B}_{1,i-1} \mathbf{e}^{-m_{i-1}(t_{i-1}-t_{i-2})} \\
dq_{2,i} &= m_{i-1} \bar{A}_{2,i-1} \mathbf{e}^{m_{i-1}(t_{i-1}-t_{i-2})} - m_{i-1} \bar{B}_{2,i-1} \mathbf{e}^{-m_{i-1}(t_{i-1}-t_{i-2})} \\
dq_{3,i} &= m_{i-1} \bar{A}_{3,i-1} \mathbf{e}^{m_{i-1}(t_{i-1}-t_{i-2})} - m_{i-1} \bar{B}_{3,i-1} \mathbf{e}^{-m_{i-1}(t_{i-1}-t_{i-2})} - \frac{u_{2,i-1}}{b_{2,i-1}}
\end{aligned}
\qquad i = 2, \dots, k \qquad (\text{A.6})$$

The solution given in Equation (A.1) can be used to solve the set of ODEs in Equation (5.17) describing the motion over the whole solution period, ΔT . This solution can be represented in more compact form as follows:

$$\theta_{sol}(t) = \sum_{i=1}^k \theta_{sol,i}(t) (H(t - t_i) - H(t - t_{i-1})) \qquad (\text{A.7})$$

where H is the Heaviside function defined in Equation (5.9) and $\theta_{sol,i}$ is given in Equation (A.1).

References

- Advanced Realtime Tracking GmbH (2008). Home page. <http://ar-tracking.eu/Home.10+B6Jkw9.0.html>.
- Aliaga, D. G. (1997). Virtual objects in the real world. *Commun. ACM* 40(3), 49–54.
- Analogue Devices Inc (2007). Home page. <http://www.analog.com/en/>.
- Appel, M. and N. Navab (2002). Registration of technical drawings and calibrated images for industrial augmented reality. *Mach. Vis. Appl* 13(3), 111–118.
- Ascension Technology Corporation (2007). Home page. <http://www.ascension-tech.com/>.
- Auer, T., S. Brantner, and A. Pinz (1999). The integration of optical and magnetic tracking for multi-user augmented reality. In M. Gervaut, D. Schmalstieg, and A. Hildebrand (Eds.), *Virtual Environments '99. Proceedings of the Eurographics Workshop in Vienna, Austria*, pp. 43–52.
- Azuma, R. (1997). A survey of augmented reality. *Presence* 6(4), 355–385.
- Azuma, R. et al. (1999, December). Tracking in unprepared environments for augmented reality systems. *Computers and Graphics* 23(6), 787–793.
- Azuma, R. and G. Bishop (1994). Improving static and dynamic registration in an optical see-through HMD. In *SIGGRAPH*, pp. 197–204. ACM.
- Azuma, R. and G. Bishop (1995). A frequency-domain analysis of head-motion prediction. In *SIGGRAPH*, pp. 401–408.
- Azuma, R. T. (1995). *Predictive tracking for augmented reality*. Ph. D. thesis, University of North Carolina at Chapel Hill.

- Bajura, M., H. Fuchs, and R. Ohbuchi (1992). Merging virtual objects with the real world: seeing ultrasound imagery within the patient. *SIGGRAPH Comput. Graph.* 26(2), 203–210.
- Bajura, M. and U. Neumann (1995). Dynamic registration correction in video-Based augmented reality systems. *IEEE Computer Graphics and Applications* 15(5), 52–61.
- Behzadan, A. H. and V. R. Kamat (2005). Visualization of construction graphics in outdoor augmented reality. In *WSC '05: Proceedings of the 37th conference on Winter simulation*, pp. 1914–1920. Winter Simulation Conference.
- Chai, L., K. Nguyen, B. Hoff, and T. Vincent (1999). An adaptive estimator for registration in augmented reality. In *Proceedings of IEEE International Workshop on Augmented Reality*, pp. 23–32.
- Cheok, A. D., K. H. Goh, W. Liu, F. Farbiz, S. W. Fong, S. L. Teo, Y. Li, and X. Yang (2004). Human pacman: a mobile, wide-area entertainment system based on physical, social, and ubiquitous computing. *Personal Ubiquitous Comput.* 8(2), 71–81.
- Dao, R. (2002). Thermal accelerometers temperature compensation. MEMSIC Application Note AN-00MX-002.
- Fakhr-eddine Ababsa, Jean Yves Didier, M. M. D. R. (2003, December 3-5). Head motion prediction in augmented reality systems using monte carlo particle filters. In *ICAT*, Tokyo, JAPAN.
- Feiner, S., B. Macintyre, and D. Seligmann (1993). Knowledge-based augmented reality. *Commun. ACM* 36(7), 53–62.
- Fjeld, M., P. Juchli, and B. Voegtli (2003). Chemistry education: A tangible interaction approach. In *Proceedings of IFIP INTERACT'03: Human-Computer Interaction*, 2: Tangible bits, pp. 287.
- Foxlin, E. (1996). Inertial head-tracker sensor fusion by a complimentary separate-bias kalman filter. In *VRAIS '96: Proceedings of the 1996 Virtual Reality Annual International Symposium (VRAIS 96)*, Washington, DC, USA, pp. 185. IEEE Computer Society.

- Foxlin, E., M. Harrington, and Y. Altshuler (1998). Miniature 6-DOF inertial system for tracking HMDs. In *Proceedings of the SPIE*, Volume 3362, Orlando, FL, pp. 214–228.
- Foxlin, E., M. Harrington, and G. Pfeifer (1998). Constellation: a wide-range wireless motion-tracking system for augmented reality and virtual set applications. In *SIGGRAPH '98: Proceedings of the 25th annual conference on Computer graphics and interactive techniques*, New York, NY, USA, pp. 371–378. ACM.
- Foxlin, E. and L. Naimark (2003). VIS-tracker: A wearable vision-inertial self-tracker. In *VR*, pp. 199–206. IEEE Computer Society.
- Friedmann, M., T. Starner, and A. Pentland (1992). Synchronization in virtual realities. *Presence* 1(1), 139–144.
- Gillies, G. T., D. W. Christy, J. M. Stenger, and W. C. Broaddus (2003, January). Equilibrium and non-equilibrium dynamics of the cranio-mandibular complex and cervical spine. *Journal of Medical Engineering & Technology* 27(1), 32–40.
- Golding, A. R. and N. Lesh (1999). Indoor navigation using a diverse set of cheap, wearable sensors. In *ISWC '99: Proceedings of the 3rd IEEE International Symposium on Wearable Computers*, Washington, DC, USA, pp. 29. IEEE Computer Society.
- Grossman, G. E., R. J. Leigh, L. A. Abel, D. J. Lanska, and S. E. Thurston (1988). Frequency and velocity of rotational head perturbations during locomotion. *Experimental Brain Research* 70(3), 470–476.
- Hirasaki, E., S. T. Moore, T. Raphan, and B. Cohen (1999). Effects of walking velocity on vertical head and body movements during locomotion. *Experimental Brain Research* 127(2), 117–130.
- Holloway, R. L. (1995). *Registration errors in augmented reality systems*. Ph. D. thesis, University of North Carolina at Chapel Hill.
- Holloway, R. L. (1997). Registration error analysis for augmented reality. *Presence: Teleoperators and Virtual Environments* 6(4), 413–432.
- Ichida, K. and T. Kiyono (1977). Curve fitting by a one-pass method with a piecewise cubic polynomial. *ACM Transactions on Mathematical Software* 3(2), 164–174.
- Inetersense Inc (2007). Home page. <http://www.isense.com/>.

- Janin, A.L.; Mizell, D. C. T. (1993). Calibration of head-mounted displays for augmented reality applications. *Virtual Reality Annual International Symposium, 1993., 1993 IEEE*, 246–255.
- Kato, H.; Billinghurst, M. (1999). Marker tracking and hmd calibration for a video-based augmented reality conferencing system. *Augmented Reality, 1999. (IWAR '99) Proceedings. 2nd IEEE and ACM International Workshop on*, 85–94.
- Keir, M. S., C. E. Hann, J. G. Chase, and X. Q. Chen (2007a). Accelerometer-based orientation sensing for head tracking in AR & robotics. In *Proceedings of The 2nd International Conference on Sensing Technology (ICST 2007)*, Palmerston North, New Zealand.
- Keir, M. S., C. E. Hann, J. G. Chase, and X. Q. Chen (2007b). A new approach to accelerometer-based head tracking for augmented reality & other applications. In *Proceedings of the IEEE International Conference on Automation Science and Engineering (CASE 2007)*, Scottsdale, AZ, USA, pp. 603–608.
- Kijima, R.; Ojika, T. (2002). Reflex hmd to compensate lag and correction of derivative deformation. *Virtual Reality, 2002. Proceedings. IEEE*, 172–179.
- Kourogi, M.; Kurata, T. (2003, 7-10 Oct.). Personal positioning based on walking locomotion analysis with self-contained sensors and a wearable camera. *Mixed and Augmented Reality, 2003. Proceedings. The Second IEEE and ACM International Symposium on*, 103–112.
- Kraft, E. (2003, July). A quaternion-based unscented kalman filter for orientation tracking. In *Proceedings of the 6th Int. Conf. on Information Fusion*, Cairns, Australia.
- Laerhoven, K. V. and O. Cakmakci (2000). What shall we teach our pants? In *ISWC*, pp. 77–83.
- Lang, P., M. Ribo, and A. Pinz (2002). A new combination of vision-based and inertial tracking for fully mobile, wearable and real-time operation. In *26th Workshop of the Austrian Association for Pattern Recognition (GM/AAPR)*, Volume 160, Graz, Austria, pp. 141148.
- List, U. H. (1984). Nonlinear prediction of head movements for helmet-mounted displays. Technical report, AFHRL-TP-83-45 AD-A136590, Williams AFB, AZ: Operations Training Division.

- Luinge, H., P. Veltink, and C. Baten (1999). Estimation of orientation with gyroscopes and accelerometers. In *BMES/EMBS Conference, 1999. Proceedings of the First Joint*, Volume 2, pp. 844.
- Mark, W. R., L. McMillan, and G. Bishop (1997). Post-rendering 3d warping. In *Symposium on Interactive 3D Graphics*, pp. 7–16, 180.
- MEMSIC Inc. (2008). Home page. <http://www.memsic.com/memsic/>.
- Micro Strain (2007). Home page. <http://www.microstrain.com/>.
- Milgram, P. and F. Kishino (1994). Augmented reality: A class of displays on the reality-virtuality continuum. In *SPIE, Telem manipulator and Telepresence Technologies*, Volume 2351-34, pp. 4248.
- Nintendo (2007). Wii. <http://www.nintendo.com/wii>. Visited on 30/12/2007.
- Piekarski, W. and B. Thomas (2002, January). ARQuake: the outdoor augmented reality gaming system. *Communications of the ACM* 45(1), 36–38.
- Polhemus (2008). Home page. <http://www.polhemus.com>.
- Randell, C.; Muller, H. (2000). Context awareness by analysing accelerometer data. *Wearable Computers, 2000. The Fourth International Symposium on*, 175–176.
- Reading, V. M. (1972, March). Visual resolution as measured by dynamic and static tests. *European Journal of Physiology* 333(1), 17–26.
- Ribo, M., P. Lang, H. Ganster, M. Brandner, C. Stock, and A. Pinz (2002). Hybrid tracking for outdoor augmented reality applications. *IEEE Computer Graphics and Applications* 22(6), 54–63.
- Rizos, C., T. S. Yan, and D. A. Kinllyside (2004, December). Development of sydnet permanent real-time gps network. In *The 2004 International Symposium on GNSS/GPS*, Sydney, Australia.
- Roberts, G. W., A. Evans, A. Dodson, B. Denby, S. Cooper, and R. Hollands (2002, April). The use of augmented reality, gps, and ins for subsurface data visualization. In *FIG XXII International Congress*, Washington, D.C.
- Satoh, K., M. Anabuki, H. Yamamoto, and H. Tamura (2001). A hybrid registration method for outdoor augmented reality. In *ISAR*, pp. 67–76. IEEE Computer Society.

- Schml, F., R. Kunz, and W. Stoll (2000, April). Dynamic visual acuity during linear acceleration along the inter-aural axis. *European Archives of Oto-Rhino-Laryngology* 257(4), 193–198.
- Shaw, C. and J. Liang (1992). An experiment to characterize head motion in VR and RR using MR. In *Proceedings of the 1992 Western Computer Graphics Symposium*, pp. 99–101.
- Soler, L., S. Nicolau, J. Schmid, J. Koehl, C. and Marescaux, X. Penneç, and N. Ayache (2004, Nov). Virtual reality and augmented reality in digestive surgery. *Mixed and Augmented Reality, 2004. ISMAR 2004. Third IEEE and ACM International Symposium on*, 278–279.
- State, A., G. Hirota, D. T. Chen, W. F. Garrett, and M. A. Livingston (1996). Superior augmented reality registration by integrating landmark tracking and magnetic tracking. *Computer Graphics 30*(Annual Conference Series), 429–438.
- Strickland, J. (2007). How virtual reality gear works <http://electronics.howstuffworks.com/VR-gear6.htm>. visited on 20/12/ 2007.
- Ullmer, B. and H. Ishii (2000). Emerging frameworks for tangible user interfaces. *IBM Syst. J.* 39(3-4), 915–931.
- Weinberg, H. (2002). Temperature compensation techniques for low g iMEMS accelerometers. Analogue Devices Application Note AN-598.
- Weinberg, H. (2004). Phase and frequency response of iMEMS accelerometers and gyros. Analogue Devices Application Note AN-688.
- Welch, G. and G. Bishop (1997). SCAAT: Incremental tracking with incomplete information. *Computer Graphics 31*(Annual Conference Series), 333–344.
- Welch, G. and E. Foxlin (2002). Motion tracking: No silver bullet, but a respectable arsenal. *IEEE Computer Graphics and Applications* 22(6), 24–38.
- Welch, R. B. (1978). *Perceptual Modification: Adapting to Altered Sensory Environments*. New York: Academic Press.
- Xsens Technology (2007). Home page. <http://www.xsens.com/>.
- You, S. and U. Neumann (2001). Fusion of vision and gyro tracking for robust augmented reality registration. In *VR*, pp. 71–78.

- You, S., U. Neumann, and R. Azuma (1999a). Hybrid inertial and vision tracking for augmented reality registration. In *VR*, pp. 260.
- You, S., U. Neumann, and R. Azuma (1999b, November/December). Orientation tracking for outdoor augmented reality registration. *IEEE Computer Graphics and Applications* 19(6), 36–42.